

ANL-7750

RETURN TO ANL (IDAFD) LIBRARY.

7750

ANL-7750

Argonne National Laboratory

CHEMICAL ENGINEERING DIVISION RESEARCH HIGHLIGHTS

January—December 1970

The facilities of Argonne National Laboratory are owned by the United States Government. Under the terms of a contract (W-31-109-Eng-38) between the U. S. Atomic Energy Commission, Argonne Universities Association and The University of Chicago, the University employs the staff and operates the Laboratory in accordance with policies and programs formulated, approved and reviewed by the Association.

MEMBERS OF ARGONNE UNIVERSITIES ASSOCIATION

The University of Arizona	Kansas State University	The Ohio State University
Carnegie-Mellon University	The University of Kansas	Ohio University
Case Western Reserve University	Loyola University	The Pennsylvania State University
The University of Chicago	Marquette University	Purdue University
University of Cincinnati	Michigan State University	Saint Louis University
Illinois Institute of Technology	The University of Michigan	Southern Illinois University
University of Illinois	University of Minnesota	The University of Texas at Austin
Indiana University	University of Missouri	Washington University
Iowa State University	Northwestern University	Wayne State University
The University of Iowa	University of Notre Dame	The University of Wisconsin

NOTICE

This report was prepared as an account of work sponsored by the United States Government. Neither the United States nor the United States Atomic Energy Commission, nor any of their employees, nor any of their contractors, subcontractors, or their employees, makes any warranty, express or implied, or assumes any legal liability or responsibility for the accuracy, completeness or usefulness of any information, apparatus, product or process disclosed, or represents that its use would not infringe privately-owned rights.

Printed in the United States of America
Available from
National Technical Information Service
U.S. Department of Commerce
5285 Port Royal Road
Springfield, Virginia 22151
Price: Printed Copy \$3.00; Microfiche \$0.95

ARGONNE NATIONAL LABORATORY
9700 South Cass Avenue
Argonne, Illinois 60439

CHEMICAL ENGINEERING DIVISION
RESEARCH HIGHLIGHTS

January-December 1970

R. C. Vogel, Division Director
L. Burris, Associate Division Director
A. D. Tevebaugh, Associate Division Director
D. S. Webster, Associate Division Director
E. R. Proud, Assistant Division Director
J. Royal

TABLE OF CONTENTS

	<u>Page</u>
ABSTRACT	7
I. FUEL-CYCLE TECHNOLOGY	7
A. Liquid Metal Decladding of Reactor Fuels	7
1. Plant Concept for LMFBR Fuel Decladding	8
2. Cladding Dissolution in Liquid Zinc	9
3. Control of Fission Product Iodine in a Pyrochemical Head-End Process	11
B. Continuous Conversion of U/Pu Nitrates to Oxides	14
1. Laboratory Investigations	15
2. Engineering Program	17
C. In-Line Analysis in Fuel Fabrication	18
1. Determination of Pu/U Ratio	19
2. Determination of O/M Ratio	20
3. Conclusions	21
D. Adaptation of Centrifugal Contactors in LMFBR Fuel Processing	21
II. SODIUM TECHNOLOGY	25
A. Sodium Chemistry	25
1. Characterization of Oxygen- and Hydrogen-Bearing Species in Sodium	26
2. Characterization of Carbon- and Nitrogen-Bearing Species in Sodium	29
3. Solubility of Xenon in Liquid Sodium	32
B. Analytical Standards Program	35
1. Analytical Standards Laboratory	35
2. Analytical Development	37
C. Engineering Development	39
1. Monitoring of Sodium Purity	39
2. Failed Element Detection and Location (FEDAL) Systems and Radioactive Repair Engineering	47
3. Nature and Control of Sodium Aerosol	51

TABLE OF CONTENTS

	<u>Page</u>
III. MATERIALS CHEMISTRY AND THERMODYNAMICS	53
A. High-Temperature Thermodynamic Studies.	53
1. Volatilization Studies of Uranium-Plutonium Oxides by Mass Spectrometry.	53
2. Phase and Reaction Studies of U-O-Na and U-Pu- O-Na Systems	54
3. Mass-Spectrometric Study of Sodium-Fuel Interaction. .	55
4. Influence of Oxygen Contamination on Carbon and Uranium Activities in UC.	56
B. Reactor Safety and Physical Property Studies.	57
1. Enthalpies and Heat Capacities by Drop Calorimetry. . .	58
2. Vapor Pressure over UO_2 at High Temperatures	59
3. Matrix Isolation Spectroscopy of UO_2	61
4. Speed of Sound in Molten Sodium and UO_2	62
5. Theoretical Calculations of Measured Physical Property Data to High Temperatures	63
6. Thermal Diffusivity of Reactor Materials	63
7. Reactor Materials--Fuel Phase Studies at High Temperatures	64
C. Calorimetry.	65
1. Thermochemistry of Plutonium Compounds: Enthalpy of Formation of Plutonium Sesquicarbide	66
2. Thermochemistry of Hydrogen Fluoride	66
3. Enthalpies of Formation of Disodium and Monosodium Acetylides	68
4. Thermochemistry of Na_3UO_4 and Na_2O	69
5. Enthalpy of Formation of Molybdenum Disulfide.	69
6. Enthalpy of Formation of Xenon Hexafluoride.	69
7. Quantum Chemical Investigations of Selected Nonmetal Monofluorides	70
IV. ANALYTICAL AND REACTOR CHEMISTRY	72
A. Chemistry of Irradiated Fast Reactor Fuels and Materials. .	72
1. Distribution of Noble Fission-Product Gas in Mixed- Oxide Fuels.	72
2. Electron Microprobe Analysis of Irradiated Mixed- Oxide Fuels.	74

TABLE OF CONTENTS

	<u>Page</u>
B. Fast-Reactor Cross-Section Measurements	77
1. Spectrum-Averaged Measurements	77
2. Low-Mass Fast-Neutron Fission Yields	81
3. Dosimetry Characterization of a Fast-Neutron Irradiation Environment.	82
C. Fission Yields as a Function of Neutron Energy	82
V. CHEMISTRY OF LIQUID METALS AND MOLTEN SALTS . . .	86
A. Liquid Metal Studies	86
1. Thermodynamics	86
2. Transport Properties	98
B. Molten Salt Studies	104
1. Thermodynamics	104
2. Structure Investigations by Spectroscopic Methods . . .	113
C. Energy Conversion	117
1. High-Specific-Energy Lithium/Selenium Batteries for Implantation	117
2. High-Specific-Power Lithium/Selenium Cells for Hybrid Vehicle Propulsion	124
3. High-Specific-Energy Lithium/Sulfur Cells for Electric Vehicles	131
VI. NUCLEAR SAFEGUARDS STUDY	140
VII. FLUIDIZED-BED COMBUSTION OF FOSSIL FUELS.	141
A. Coal-Combustion Experiments with Pulverized Limestone	142
B. Coal-Combustion Experiments with Coarse Limestone. . .	142
C. Natural Gas Combustion Experiments--NO Levels and SO ₂ Sorption and Desorption from CaSO ₄	144
D. Reduction of Nitrogen Oxide Emission in Coal- Combustion Experiments	144
E. Mathematical Modeling Studies	145
VIII. ADDENDUM	146

TABLE OF CONTENTS

1. Introduction	1
2. Materials and Methods	2
3. Results	3
4. Discussion	4
5. Conclusion	5
6. Acknowledgments	6
7. References	7
8. Appendix	8
9. Index	9
10. Glossary	10
11. Bibliography	11
12. Figures	12
13. Tables	13
14. Summary	14
15. Abstract	15
16. Introduction	16
17. Materials and Methods	17
18. Results	18
19. Discussion	19
20. Conclusion	20
21. Acknowledgments	21
22. References	22
23. Appendix	23
24. Index	24
25. Glossary	25
26. Bibliography	26
27. Figures	27
28. Tables	28
29. Summary	29
30. Abstract	30
31. Introduction	31
32. Materials and Methods	32
33. Results	33
34. Discussion	34
35. Conclusion	35
36. Acknowledgments	36
37. References	37
38. Appendix	38
39. Index	39
40. Glossary	40
41. Bibliography	41
42. Figures	42
43. Tables	43
44. Summary	44
45. Abstract	45
46. Introduction	46
47. Materials and Methods	47
48. Results	48
49. Discussion	49
50. Conclusion	50
51. Acknowledgments	51
52. References	52
53. Appendix	53
54. Index	54
55. Glossary	55
56. Bibliography	56
57. Figures	57
58. Tables	58
59. Summary	59
60. Abstract	60
61. Introduction	61
62. Materials and Methods	62
63. Results	63
64. Discussion	64
65. Conclusion	65
66. Acknowledgments	66
67. References	67
68. Appendix	68
69. Index	69
70. Glossary	70
71. Bibliography	71
72. Figures	72
73. Tables	73
74. Summary	74
75. Abstract	75
76. Introduction	76
77. Materials and Methods	77
78. Results	78
79. Discussion	79
80. Conclusion	80
81. Acknowledgments	81
82. References	82
83. Appendix	83
84. Index	84
85. Glossary	85
86. Bibliography	86
87. Figures	87
88. Tables	88
89. Summary	89
90. Abstract	90
91. Introduction	91
92. Materials and Methods	92
93. Results	93
94. Discussion	94
95. Conclusion	95
96. Acknowledgments	96
97. References	97
98. Appendix	98
99. Index	99
100. Glossary	100
101. Bibliography	101
102. Figures	102
103. Tables	103
104. Summary	104
105. Abstract	105
106. Introduction	106
107. Materials and Methods	107
108. Results	108
109. Discussion	109
110. Conclusion	110
111. Acknowledgments	111
112. References	112
113. Appendix	113
114. Index	114
115. Glossary	115
116. Bibliography	116
117. Figures	117
118. Tables	118
119. Summary	119
120. Abstract	120
121. Introduction	121
122. Materials and Methods	122
123. Results	123
124. Discussion	124
125. Conclusion	125
126. Acknowledgments	126
127. References	127
128. Appendix	128
129. Index	129
130. Glossary	130
131. Bibliography	131
132. Figures	132
133. Tables	133
134. Summary	134
135. Abstract	135
136. Introduction	136
137. Materials and Methods	137
138. Results	138
139. Discussion	139
140. Conclusion	140
141. Acknowledgments	141
142. References	142
143. Appendix	143
144. Index	144
145. Glossary	145
146. Bibliography	146
147. Figures	147
148. Tables	148
149. Summary	149
150. Abstract	150
151. Introduction	151
152. Materials and Methods	152
153. Results	153
154. Discussion	154
155. Conclusion	155
156. Acknowledgments	156
157. References	157
158. Appendix	158
159. Index	159
160. Glossary	160
161. Bibliography	161
162. Figures	162
163. Tables	163
164. Summary	164
165. Abstract	165
166. Introduction	166
167. Materials and Methods	167
168. Results	168
169. Discussion	169
170. Conclusion	170
171. Acknowledgments	171
172. References	172
173. Appendix	173
174. Index	174
175. Glossary	175
176. Bibliography	176
177. Figures	177
178. Tables	178
179. Summary	179
180. Abstract	180
181. Introduction	181
182. Materials and Methods	182
183. Results	183
184. Discussion	184
185. Conclusion	185
186. Acknowledgments	186
187. References	187
188. Appendix	188
189. Index	189
190. Glossary	190
191. Bibliography	191
192. Figures	192
193. Tables	193
194. Summary	194
195. Abstract	195
196. Introduction	196
197. Materials and Methods	197
198. Results	198
199. Discussion	199
200. Conclusion	200
201. Acknowledgments	201
202. References	202
203. Appendix	203
204. Index	204
205. Glossary	205
206. Bibliography	206
207. Figures	207
208. Tables	208
209. Summary	209
210. Abstract	210
211. Introduction	211
212. Materials and Methods	212
213. Results	213
214. Discussion	214
215. Conclusion	215
216. Acknowledgments	216
217. References	217
218. Appendix	218
219. Index	219
220. Glossary	220
221. Bibliography	221
222. Figures	222
223. Tables	223
224. Summary	224
225. Abstract	225
226. Introduction	226
227. Materials and Methods	227
228. Results	228
229. Discussion	229
230. Conclusion	230
231. Acknowledgments	231
232. References	232
233. Appendix	233
234. Index	234
235. Glossary	235
236. Bibliography	236
237. Figures	237
238. Tables	238
239. Summary	239
240. Abstract	240
241. Introduction	241
242. Materials and Methods	242
243. Results	243
244. Discussion	244
245. Conclusion	245
246. Acknowledgments	246
247. References	247
248. Appendix	248
249. Index	249
250. Glossary	250
251. Bibliography	251
252. Figures	252
253. Tables	253
254. Summary	254
255. Abstract	255
256. Introduction	256
257. Materials and Methods	257
258. Results	258
259. Discussion	259
260. Conclusion	260
261. Acknowledgments	261
262. References	262
263. Appendix	263
264. Index	264
265. Glossary	265
266. Bibliography	266
267. Figures	267
268. Tables	268
269. Summary	269
270. Abstract	270
271. Introduction	271
272. Materials and Methods	272
273. Results	273
274. Discussion	274
275. Conclusion	275
276. Acknowledgments	276
277. References	277
278. Appendix	278
279. Index	279
280. Glossary	280
281. Bibliography	281
282. Figures	282
283. Tables	283
284. Summary	284
285. Abstract	285
286. Introduction	286
287. Materials and Methods	287
288. Results	288
289. Discussion	289
290. Conclusion	290
291. Acknowledgments	291
292. References	292
293. Appendix	293
294. Index	294
295. Glossary	295
296. Bibliography	296
297. Figures	297
298. Tables	298
299. Summary	299
300. Abstract	300
301. Introduction	301
302. Materials and Methods	302
303. Results	303
304. Discussion	304
305. Conclusion	305
306. Acknowledgments	306
307. References	307
308. Appendix	308
309. Index	309
310. Glossary	310
311. Bibliography	311
312. Figures	312
313. Tables	313
314. Summary	314
315. Abstract	315
316. Introduction	316
317. Materials and Methods	317
318. Results	318
319. Discussion	319
320. Conclusion	320
321. Acknowledgments	321
322. References	322
323. Appendix	323
324. Index	324
325. Glossary	325
326. Bibliography	326
327. Figures	327
328. Tables	328
329. Summary	329
330. Abstract	330
331. Introduction	331
332. Materials and Methods	332
333. Results	333
334. Discussion	334
335. Conclusion	335
336. Acknowledgments	336
337. References	337
338. Appendix	338
339. Index	339
340. Glossary	340
341. Bibliography	341
342. Figures	342
343. Tables	343
344. Summary	344
345. Abstract	345
346. Introduction	346
347. Materials and Methods	347
348. Results	348
349. Discussion	349
350. Conclusion	350
351. Acknowledgments	351
352. References	352
353. Appendix	353
354. Index	354
355. Glossary	355
356. Bibliography	356
357. Figures	357
358. Tables	358
359. Summary	359
360. Abstract	360
361. Introduction	361
362. Materials and Methods	362
363. Results	363
364. Discussion	364
365. Conclusion	365
366. Acknowledgments	366
367. References	367
368. Appendix	368
369. Index	369
370. Glossary	370
371. Bibliography	371
372. Figures	372
373. Tables	373
374. Summary	374
375. Abstract	375
376. Introduction	376
377. Materials and Methods	377
378. Results	378
379. Discussion	379
380. Conclusion	380
381. Acknowledgments	381
382. References	382
383. Appendix	383
384. Index	384
385. Glossary	385
386. Bibliography	386
387. Figures	387
388. Tables	388
389. Summary	389
390. Abstract	390
391. Introduction	391
392. Materials and Methods	392
393. Results	393
394. Discussion	394
395. Conclusion	395
396. Acknowledgments	396
397. References	397
398. Appendix	398
399. Index	399
400. Glossary	400
401. Bibliography	401
402. Figures	402
403. Tables	403
404. Summary	404
405. Abstract	405
406. Introduction	406
407. Materials and Methods	407
408. Results	408
409. Discussion	409
410. Conclusion	410
411. Acknowledgments	411
412. References	412
413. Appendix	413
414. Index	414
415. Glossary	415
416. Bibliography	416
417. Figures	417
418. Tables	418
419. Summary	419
420. Abstract	420
421. Introduction	421
422. Materials and Methods	422
423. Results	423
424. Discussion	424
425. Conclusion	425
426. Acknowledgments	426
427. References	427
428. Appendix	428
429. Index	429
430. Glossary	430
431. Bibliography	431
432. Figures	432
433. Tables	433
434. Summary	434
435. Abstract	435
436. Introduction	436
437. Materials and Methods	437
438. Results	438
439. Discussion	439
440. Conclusion	440
441. Acknowledgments	441
442. References	442
443. Appendix	443
444. Index	444
445. Glossary	445
446. Bibliography	446
447. Figures	447
448. Tables	448
449. Summary	449
450. Abstract	450
451. Introduction	451
452. Materials and Methods	452
453. Results	453
454. Discussion	454
455. Conclusion	455
456. Acknowledgments	456
457. References	457
458. Appendix	458
459. Index	459
460. Glossary	460
461. Bibliography	461
462. Figures	462
463. Tables	463
464. Summary	464
465. Abstract	465
466. Introduction	466
467. Materials and Methods	467
468. Results	468
469. Discussion	469
470. Conclusion	470
471. Acknowledgments	471
472. References	472
473. Appendix	473
474. Index	474
475. Glossary	475
476. Bibliography	476
477. Figures	477
478. Tables	478
479. Summary	479
480. Abstract	480
481. Introduction	481
482. Materials and Methods	482
483. Results	483
484. Discussion	484
485. Conclusion	485
486. Acknowledgments	486
487. References	487
488. Appendix	488
489. Index	489
490. Glossary	490
491. Bibliography	491
492. Figures	492
493. Tables	493
494. Summary	494
495. Abstract	495
496. Introduction	496
497. Materials and Methods	497
498. Results	498
499. Discussion	499
500. Conclusion	500
501. Acknowledgments	501
502. References	502
503. Appendix	503
504. Index	504
505. Glossary	505
506. Bibliography	506
507. Figures	507
508. Tables	508
509. Summary	509
510. Abstract	510
511. Introduction	511
512. Materials and Methods	512
513. Results	513
514. Discussion	514
515. Conclusion	515
516. Acknowledgments	516
517. References	517
518. Appendix	518
519. Index	519
520. Glossary	520
521. Bibliography	521
522. Figures	522
523. Tables	523
524. Summary	524
525. Abstract	525
526. Introduction	526
527. Materials and Methods	527
528. Results	528
529. Discussion	529
530. Conclusion	530
531. Acknowledgments	531
532. References	532
533. Appendix	533
534. Index	534
535. Glossary	535
536. Bibliography	536
537. Figures	537
538. Tables	538
539. Summary	539
540. Abstract	540
541. Introduction	541
542. Materials and Methods	542
543. Results	543
544. Discussion	544
545. Conclusion	545
546. Acknowledgments	546
547. References	547
548. Appendix	548
549. Index	549
550. Glossary	550
551. Bibliography	551
552. Figures	552
553. Tables	553
554. Summary	554
555. Abstract	555
556. Introduction	556
557. Materials and Methods	557
558. Results	558

ABSTRACT

During 1970, the Chemical Engineering Division has continued its investigations in the areas of fuel-cycle technology, sodium technology, materials properties, analytical and reactor chemistry, liquid-metal and molten-salt studies, energy conversion, and fluidized-bed combustion of fossil fuels. For reprocessing LMFBR irradiated fuel, a head-end process for decladding the fuel in liquid metal, a process for converting recovered plutonium and uranium nitrate solutions to oxides, and a centrifugal contactor suitable for high plutonium content are being developed. Analytical procedures adaptable to in-line use in the fabrication of LMFBR fuel are also being studied. In the sodium technology program, major emphasis is being placed on the measurement of sodium quality by chemical analyses and on-line monitors. An effort is also being made to develop failed-fuel-element detectors. Materials and chemistry studies are concerned with various aspects of the behavior of materials in fast reactors. Fuel-cladding interactions and material-transport phenomena in mixed-oxide fuel are being studied. Thermodynamic studies of the U-C-O and U-Pu-O systems are being carried out, and a considerable effort is being made to obtain information on the sodium-fuel reaction. High-temperature physical-property data needed for fast-reactor safety analysis are being obtained. Calorimetric procedures are being used to obtain thermochemical data on materials of interest in reactor technology. Determinations of fast-reactor cross sections and fission yields are continuing. Development efforts also continue on secondary electrical batteries for vehicle propulsion and for powering an artificial heart as well as on fluidized combustion of fossil fuels as a means of reducing pollutants. A new program on nuclear safeguards has been started.

I. FUEL-CYCLE TECHNOLOGY

A. Liquid Metal Decladding of Reactor Fuels

The reference fuel recovery process for liquid metal-cooled fast breeder reactors (LMFBRs) of the future is a modified shear-leach process followed by solvent extraction. The most difficult and costly aspect of LMFBR fuel reprocessing will probably be the head-end operations, which include fuel subassembly handling, cladding removal, iodine and sodium removal, and introduction of the fuel into an acid dissolver. These

operations would be accomplished in a shear-leach head-end process by shearing the fuel into short lengths, oxidizing the UO_2 to U_3O_8 to pulverize the fuel, and selectively leaching the exposed fuel from the stainless steel cladding with nitric acid. The shear-leach procedure is practiced with fuels from the present thermal reactors, but decladding of LMFBR oxide fuels by shear-leaching would encounter problems related to the higher burnups, higher burnup rates, shorter cooling times, residual sodium, and high plutonium content of LMFBR fuel.

Liquid-metal decladding processes under development at Argonne provide an attractive head-end for LMFBR fuel. In liquid-metal decladding, the cladding is removed by immersing the fuel subassembly (probably after the bottom is cropped) in molten zinc at 800°C . The zinc corrodes away the cladding and the subassembly supporting members but does not react with the fuel oxides. After the zinc-steel phase is largely removed from the vessel containing the fuel oxides, the fuel oxides are reduced to metal with Mg-Zn-Ca, producing a uranium precipitate and a Mg-Zn-Pu solution. The plutonium-bearing solution is removed from the vessel for further processing. Iron is added to the uranium to form liquid U-5 wt % Fe alloy, which is cast as ingots for storage. This procedure avoids mechanical disassembly of the fuel and shearing and has the following advantages: (1) efficient and early removal of iodine and other volatile fission products, (2) relative ease of dissipation of fission-product decay heat, (3) safe handling of residual sodium, and (4) production of solid wastes (except that waste xenon and krypton remain gaseous and are collected and stored in a gas mixture containing about 50% xenon plus krypton).

The principal disadvantages of the liquid-metal head-end process (which are not considered to be serious) are the lack of industrial experience in the use of refractory metals as materials of construction, the large quantity of zinc required, and the large amount of solvent metal cations introduced into the acid solution (during dissolution) and ultimately into the wastes. The latter two disadvantages could be lessened by vacuum evaporation of zinc from the zinc-steel (before disposal as waste) and of Mg-Zn solvent from the Mg-Zn-Pu (before acid dissolution). The recovered zinc and Zn-Mg could be recycled.

1. Plant Concept for LMFBR Fuel Decladding

In the previous report (ANL-7650, p. 1), a plant concept for decladding 5 tons/day of fuel was discussed. That concept did not include the reduction step which now appears necessary to assure adequate iodine removal and to simplify materials handling.

A preliminary conceptual design for the decladding-reduction head-end process has been prepared for a 4.8 metric ton/day plant. The unit is represented in elevation view in Fig. I-1. The principal process

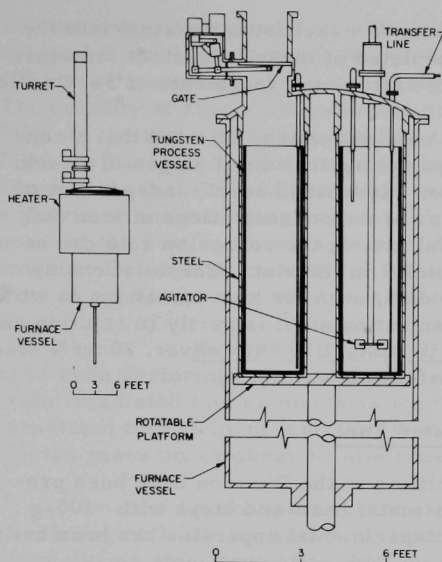


Fig. I-1. Head-End Processing Unit--Elevation View. ANL Neg. No. 308-2376.

unit is a $5\frac{1}{2}$ -ft-dia furnace chamber containing a rotatable platform. On the platform are three 2-ft-dia by 8-ft-deep tungsten process vessels, one located at each of three process stations. Decladding is performed at the first position, reduction of uranium and plutonium at the second position, and uranium dissolution at the third. The three process steps normally proceed simultaneously, one step in each vessel.

Before the platform and three process vessels are rotated, the platform is lowered to allow the tungsten vessels to clear the transfer lines and agitator during rotation. The vessels are rotated once every 2 hr; 36 subassemblies are processed each day, equivalent to about 4.8 metric tons of fuel per day.

Fuel is charged from a transfer turret fastened to the top of the process unit into the tungsten vessel at the decladding station. Three fuel subassemblies at a time are introduced through gates between the turret and process unit. All other process streams (e.g., zinc for decladding) are pressurized into or out of the tungsten vessels through transfer lines. Agitation is provided at the reduction station, but not at the other process stations.

The cover gas in the furnace chamber and process vessels during decladding is composed of xenon, argon, and krypton. No specific composition is maintained, but rather the mixture represents gases released into the process unit during decladding and purging operations. It is expected that the gas will contain about 45% Xe and 5% Kr. After gas is used to make pressure transfers of solutions between vessels, the gas is compressed to 100 psi and temporarily stored for reuse. Periodically, accumulated gases are removed from temporary storage and are further compressed for permanent storage in gas cylinders.

2. Cladding Dissolution in Liquid Zinc

a. Dissolution Mechanism

Evidence was presented previously (ANL-7650, p. 3) that attack of stainless steel by zinc begins by penetration of liquid zinc into

stainless steel and preferential leaching of nickel from the steel into the zinc. As the surface of the steel is depleted of nickel, the steel structure changes sufficiently so that it fractures into small fragments of Fe-Cr alloy.

Additional data were obtained which indicated that a constant reaction-zone thickness develops during the initial stages of attack, and that this is followed by a corrosion rate that is nearly independent of the presence or absence of agitation or of the concentrations of iron and chromium in solution. After the initial attack, the corrosion rate can be predicted from the concentration of nickel in the zinc. The relationship obtained was observed to apply to all data, even for zinc containing 26 wt % stainless steel, although at this concentration steel is partly in solution and partly in suspension and the mixture is paste-like. (However, 20 wt % steel in zinc is sufficiently fluid to be transferable as liquid.)

b. Decladding of Irradiated Fuel

The Senior Cave facilities of the Division have been prepared for use in demonstrating liquid-metal head-end steps with ~100-g quantities of highly irradiated fuel. Experimental apparatus has been built and is being tested.

For the first runs with irradiated fuel, stainless steel cladding will be dissolved from an irradiated $\text{UO}_2\text{-PuO}_2$ fuel element contained in a tantalum basket, and the declad fuel will be examined in the basket. The fuel will then be reduced and all process streams, including the cover gas, will be analyzed. The experiments are expected to demonstrate plutonium recovery and fission-product behavior and to reveal the physical condition of declad fuel following decladding.

c. Engineering-Scale Experiments

In one concept of liquid-metal decladding of LMFBR fuel, three fuel subassemblies are contained in a basket during decladding in liquid zinc. After decladding, the basket (which then contains $\text{UO}_2\text{-PuO}_2$) is lifted out of the melt. Before the decladding concept utilizing a basket was replaced with the decladding-reduction concept described in the introduction of this section, three experiments were done with a basket comprising a Mo-30% W frame and base plate and a $5\frac{3}{4}$ -in.-dia cylindrical tantalum wall with approximately one hundred $1/16$ -in. holes in the lower $3\frac{1}{2}$ in.

The basket was charged with a stainless steel tube (4-in. OD, $1/8$ -in. wall, and 5-in. height) and UO_2 pellets or crushed pellets of a selected particle size distribution. The basket and contents were immersed in zinc at 800°C . After the steel tube had corroded, the basket

was removed, the cylindrical wall was slid upward, and the contents were scraped from the base of the basket into a tray. In each experiment, about 10% of the iron originally in the charge was found with the recovered UO_2 . The quantity of zinc-stainless steel heel roughly equalled the quantity of UO_2 . In the two runs employing UO_2 fines, about 10% of the fines were lost from the basket. Application of the basket concept to fuel containing an appreciable fraction of fines might require an improved basket design and a provision for removing any oxide fines from the zinc melt prior to disposal of the zinc melt as waste. Improved separation of steel from the fuel oxide would require greater circulation of zinc through the basket wall. This might be accomplished by sloshing the basket in the liquid.

Release of Fission-Product Gases. Several experiments have been performed simulating the rapid release of fission-product gases from irradiated fuel elements as may occur during decladding in zinc. An irradiated fuel element (fuel pin) is expected to contain about 25 cm^3 of fission gases under about 50-atm pressure.

In the most recent experiment, two simulated fuel elements consisting of 0.010-in. wall by 1/4-in.-OD tubes containing about 4 in. of close-fitting steel rods at the bottom and 25 cm^3 of argon at 50-atm pressure were made into a bundle with 15 wire-wrapped 1/4-in.-dia steel rods. This bundle was placed in a 2-in.-OD steel tube simulating a shroud and immersed 3 in. into zinc at 795°C . After about 1.9 min, the two tubes ruptured and vented rapidly. Inspection of the tubes after the run revealed that the bottoms were missing, that the steel rods (simulating fuel) had remained in the tubes, and that zinc had splashed around the tubes and rods inside the shroud to a height of only 20 in. There was no evidence that zinc had splashed outside the shroud.

The experimental results indicate that zinc will be splashed by a rapid release of fission-product gases during zinc decladding but that this will present no serious problems.

3. Control of Fission Product Iodine in a Pyrochemical Head-End Process

Reprocessing of 30-day-cooled fast reactor fuel by a Purex process requires decontamination factors for iodine¹ of 10^7 - 10^8 in the head-end step to avoid accumulation of iodine in the organic streams. A pyrochemical head-end process comprising decladding and reduction steps is being investigated. Both of these steps are completed with the fuel immersed in liquid metals. The volatile iodine that is released when stainless steel cladding dissolves in the molten zinc used for decladding reacts with

¹"Aqueous Processing of LMFBR Fuels," USAEC Report ORNL-4436, p. 171 (1970).

the zinc. The degree of interaction of iodine with zinc has been determined experimentally, and the results are presented in this report.

The assumptions used to define the scope of the experiments were (1) iodine exists in the fuel element mainly as elemental iodine and to only a small extent as CsI and FeI_2 ; (2) when the lower end of a fuel element is immersed in zinc in a decladding vessel, the cladding ruptures and elemental iodine mixed with xenon and krypton flows from the fuel element plenum through the annulus and is released through the aperture made by the rupture; and (3) the gas mixture from the plenum is released into the zinc pool as a sequence of bubbles.

Experiments were performed simulating the release of fission gases from fuel elements. To generate an iodine-argon gas stream, argon carrier gas was passed through a reservoir containing iodine labelled with ^{131}I and held at a constant temperature. The argon-iodine mixture was bubbled through a pool of liquid zinc, which was covered by a 2-cm deep layer of LiCl-KCl eutectic. Any iodine in the effluent gas from the zinc-salt pool was removed by scrubbing the gas stream with 0.1M $\text{Na}_2\text{S}_2\text{O}_3$ - 1M NaOH solution. The depth of the zinc pool, the gas flow rate, the iodine concentration in the carrier gas, and the temperature of the zinc were varied in different experiments.

Although iodine at first reacts with zinc, no iodine is found in the zinc at the end of the runs. The amount of iodine that reacts with the zinc is determined by dissolving all of the LiCl-KCl in water at the conclusion of an experiment and by counting the contained ^{131}I in that solution and in the scrubber solution. The results are given in Table I-1. From the ratio of the counting rate of an aliquot of the salt solution to the counting rate of an aliquot of the scrubber solution, the decontamination factor can be calculated. The counting rate in the scrubber solution never exceeded background. Thus, iodine had been completely absorbed, even at a zinc pool depth of only 3 cm and gas flow rates of 500 ml/min. The latter gas flow rate corresponded to 70 bubbles per second. The flow rate of gas through the zinc pool had no apparent effect on the reaction.

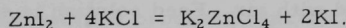
To prove that the absence of iodine in the scrubber solution resulted from iodine capture in the zinc-salt rather than reaction of iodine with equipment components or a malfunction of the aqueous scrubber, an experiment was conducted with zinc absent. At the end of this experiment, one half of the iodine was detected in the aqueous scrubber and the other half was in the cover salt. This indicates that a large amount of iodine in the effluent gas from the zinc-salt pool would be absorbed in the scrubber solution.

TABLE 1-1. Iodine Absorption in Zinc

Expt.	Depth ^a of Zinc Pool (cm)	Temp of Zinc (°C)	Concen. of Iodine in Ar (at. %)	Ar-I ₂ Flow Rate (ml/min)	Amount of Iodine Transported (mg)	Final Cover Salt Activity [counts/(min) (aliquot)]	Final Scrubber Activity [counts/(min) (aliquot)]
1	17	500	0.1	65	22	3 × 10 ⁴	Background ^b
2	10	800	0.1	65	35		Background ^b
			0.1	150	38		Background ^b
			0.2	150	76	1 × 10 ⁵	Background ^b
3	3	800	0.2	150	205		Background ^b
				300	205		Background ^b
				500	205	5 × 10 ⁵	Background ^b
4	3	500	0.2	150	205		Background ^b
				300	205		Background ^b
				500	205	3 × 10 ⁵	Background ^b
5	3	500	3 × 10 ⁻³	300	17	7 × 10 ⁵	Background ^b
6	10	800	0.2	150	630	1.2 × 10 ⁶	Background ^b
7	Salt Only	800 ^c	0.1	150	25	7.0 × 10 ³	7.3 × 10 ³

^aCover salt depth was 2 cm in all runs.^bError in background was +8 counts/min.^cTemperature of salt phase.

Further study indicated that the reaction of iodine with the Zn-LiCl-KCl medium probably occurs in two steps. The first step is formation of ZnI₂ from zinc and iodine. However, iodine would not be retained in the zinc-salt melt as ZnI₂ since this compound has a vapor pressure of 760 Torr at 625°C. At 800°C (the normal temperature of the bath), ZnI₂ would be expected to evaporate from the melt. A Raman spectroscopic analysis² was made of a salt sample prepared by bubbling iodine through molten zinc-salt until the mole fraction of iodine in the salt was 0.05. The only observed peak in the Raman spectrum of the salt at 450°C was attributed to ZnCl₄²⁻. This finding suggests that the second step is a reaction between ZnI₂ and LiCl-KCl:



Owing to this reaction, iodine is completely retained in the cover salt. In a plant operation, the cover salt would be discarded as dry active waste.

Two other possible chemical states of iodine, CsI and FeI₂, have not been investigated experimentally. Based on free energies of formation, CsI would not be expected to react further in the decladding or reduction steps but to collect in the cover salt. Ferrous iodide would be reduced by metallic zinc to ZnI₂ and iron.

²The Raman spectroscopic studies were made by V. A. Maroni of this Division.

The data presented here suggest strongly that adequate control of iodine in pyrochemical head-end steps is feasible under process conditions.

B. Continuous Conversion of U/Pu Nitrates to Oxides

A necessary and presently expensive step in the nuclear fuel cycle for LMFBR fuels is the conversion of uranium nitrate and plutonium nitrate solutions (produced in nuclear fuel reprocessing plants) to an oxide form. This conversion must provide the fuel fabricator with powdered fuel oxides suitable for the fabrication of fuel shapes (pellets) on a safe, reliable, economic basis. The presence of plutonium in LMFBR fuel necessitates alpha containment, and the intrinsic radiation from plutonium isotopes necessitates that operating personnel be protected from neutrons and gamma rays. This, in turn, requires that fuel be fabricated remotely or semiremotely.

Currently, oxide fuel for nuclear fuel elements is prepared by multi-step processes, which include precipitation, filtration, and calcination steps. This process is slow, unduly sensitive to process conditions, and not well suited to automation and remote operation. The unprecedentedly high plutonium throughput rates projected for LMFBR fuel recycle will require equipment of large capacity. The problems of nuclear criticality and self-radiation from plutonium are an incentive to develop continuous processes and equipment so that a high capacity can be achieved with relatively low holdup of plutonium.

A continuous process is under investigation at Argonne that offers potential economic advantages and uniform product. This process is continuous fluidized-bed denitration of uranium-plutonium nitrate solutions to a $\text{UO}_3\text{-PuO}_2$ powder form, followed by fluidized-bed reduction with hydrogen to $\text{UO}_2\text{-PuO}_2$. This process lends itself to remote operation and is based on extensive fluidized-bed calcination technology³ developed in this Division for the processing of uranyl nitrate in a feed materials plant and aluminum nitrate in a waste calcination facility.

In fluidized-bed denitration, a heated bed of oxide particles (typical of the denitration product) is fluidized with air. Feed solution is sprayed into the bed through an atomizing nozzle. The liquid droplets either strike the particles and thermally decompose (depositing a fresh oxide layer) or decompose in the gas phase (forming small solid particles). The usual denitration temperatures are 275 to 400°C. By means of an overflow arrangement (which may be supplemented with product withdrawal at the bottom of the column), the bed inventory in the denitrator is kept constant.

³A. A. Jonke, E. J. Petkus, J. W. Loeding, and S. Lawroski, Nucl. Sci. Eng. **2**, 303 (1957).

The off-gas contains NO_2 , NO , O_2 , and water, the composition varying with the temperature of denitration. The reaction is endothermic; the heat required for denitrating uranyl nitrate hexahydrate (UNH) alone at 230°C would be about 260,000 Btu/(lb-mol uranium). Decomposition of the solutions to be used here, which typically are more dilute than UNH and contain excess nitric acid, will require an even greater heat input.

An integrated program for laboratory studies and experimental work on a pilot engineering scale is in progress.

1. Laboratory Investigations

Initial work in the laboratory program was directed toward characterization (composition and structure) of denitration products and the study of the sinterability of fuel oxide prepared by denitration. In laboratory-scale experiments to characterize denitration products, solutions containing uranyl nitrate alone, plutonium nitrate alone, and U-20% Pu nitrate (1.5M total metal ions) were denitrated by feeding a solution dropwise to a hot surface maintained at 300 to 600°C . Approximately 6 g of oxide was prepared in each experiment. Selected oxide products were examined by X-ray diffraction, with an electron microprobe, and by autoradiography with the following results.

The major phase in the UO_3 -20 wt % PuO_2 material made at 450°C was identified as gamma- UO_3 ; PuO_2 possibly constituted a minor phase. Material prepared at lower temperatures ($\sim 400^\circ\text{C}$) contained gamma- UO_3 and $\text{UO}_3 \cdot \text{H}_2\text{O}$. Electron-microprobe and autoradiographic examinations of mixed-oxide powder prepared at 450°C indicated that plutonium distribution in the uranium oxide matrix was good. Two types of electron-microprobe examination were made--scanning (8 by $10\text{-}\mu\text{m}$ and 80 by $100\text{-}\mu\text{m}$ areas) and single-spot ($0.5\text{-}\mu\text{m}$ -dia beam). It is noteworthy that, in a check of 30 individual spots, not a single spot was found to be completely free of plutonium, although the concentrations of plutonium varied considerably.

Plutonium nitrate solutions denitrated at 450 and 300°C produced only PuO_2 with the product prepared at 450°C showing greater crystallinity. X-ray diffraction patterns of PuO_2 prepared by dropwise denitration at 300°C from (1) a 65% Pu(VI)-35% Pu(IV) nitrate solution, and (2) a Pu(IV) nitrate solution were compared. The latter was more crystalline, but there was no other obvious difference in the diffraction patterns.

In exploratory laboratory tests performed to determine the sinterability of fuel oxide prepared by denitration, several UO_2 -17 wt % PuO_2 pellets were prepared by drop denitration of uranyl nitrate-plutonium nitrate solution, reduction of the UO_3 - PuO_2 powder to UO_2 - PuO_2 , pressing

into $\sim 1/4$ -in.-dia pellets, and sintering the pellets. The $\text{UO}_3\text{-PuO}_2$ powder was prepared by the dropwise addition of a nitrate solution (about 1.65M total U + Pu) into a quartz tube at 300°C . After transfer to a stainless steel crucible, the $\text{UO}_3\text{-PuO}_2$ was reduced to $\text{UO}_2\text{-PuO}_2$ with hydrogen at 550°C . A pressure of 87,000 psi was used in forming the pellets, which were then sintered for 90 min at 1650°C in an argon atmosphere. The pellets, which have a density up to about 89% of theoretical, are being examined for homogeneity, structure, and impurity content.

In other laboratory work, a procedure for dissolving $\text{UO}_3\text{-PuO}_2$ material produced by denitration was developed and tested in a series of scouting laboratory studies. A dissolution step is needed for the pilot-plant program to permit recycling of denitration products and thereby minimize plutonium inventory requirements. Dissolution data are also of interest for scrap recovery process development.

Dissolution tests were made with $\text{UO}_3\text{-20 wt \% PuO}_2$ and with PuO_2 alone that had been prepared by drop denitration at 300, 450, and 600°C . Nitric acid molarities were 5 to 16, dissolution temperatures were 95 to 120°C , and final actinide concentrations in the solutions were 0.35 and 1.5M .

The data indicated that (1) oxide prepared at the lowest temperature, 300°C , was easiest to dissolve, (2) the oxide dissolution rate was unaffected by the dissolution temperature, (3) the dissolution rate was unaffected by the final actinide concentration when dissolution was with 16N nitric acid, and (4) the fraction of plutonium dissolved was greater with 16N acid than with 5N ; also, the rate of plutonium dissolution was significantly higher for $\text{UO}_3\text{-20 wt \% PuO}_2$ material than for PuO_2 alone-- $\sim 99\%$ dissolution was achieved in 5 hr as compared with 30-50% dissolution for PuO_2 in a similar period.

Plutonium ion stability in nitric acid solutions (simulated feed solutions) was also studied in the laboratory. The change in valence distribution, as a result of standing, of plutonium (VI) and (IV) ions in nitrate solutions 1.35M in plutonium was measured spectrophotometrically. The amounts of Pu(VI) and Pu(IV) were calculated from the optical spectra. These data are shown in Fig. 1-2 along with data reported by Crawley⁴ for 0.82M Pu in 5.3M HNO_3 solution and earlier ANL data for a solution 1.2M U- 0.3M Pu in $2\text{-}4\text{M}$ HNO_3 .

For the initial 50-day period, the concentration of Pu(VI) is a linear function of time, indicating a zero-order reaction with respect to Pu(VI). After 50 days, the rate at which the concentration of Pu(VI) ions decreases apparently increases. The rate of valence change in the

⁴D. T. Crawley, "Pressure Buildup of Plutonium Nitrate Solutions in Sealed Shipping Containers," ARH-1093 (July 15, 1969).

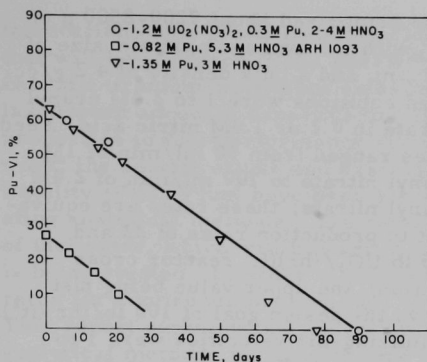


Fig. I-2. Reduction of Pu(VI) in HNO_3 .
ANL Neg No. 308-2331.

stainless steel cylindrical fluidized-bed denitrator 4 in. in diameter, which is considered critically safe for feeds containing up to 20% plutonium. A parallel effort will be the development of a slab-shaped column that offers nuclear criticality advantages when scaled up for high-plutonium systems.

The denitration pilot plant was constructed in an existing 3- by 4-module glovebox. The major unit is a 4-in.-dia fluidized-bed denitrator with integral filters. The fluidized-bed denitrator consists of three separately flanged parts--the cone-shaped gas-distributor section at the bottom of the denitrator, the denitration section, and the filter chamber. A spray nozzle and temperature or pressure sensors can be positioned at 3-, 6-, or 9-in. levels. The denitration section is heated by twelve 2000-W Watlow resistance heaters, copper-spray-bonded to the exterior wall. The filter chamber, mounted directly above the bed, is fabricated of 4-in.-dia, schedule 40, Type 304 stainless steel pipe 47 in. long, and contains two 18-in.-long sintered stainless steel filters.

Auxiliaries include a nitrate solution make-up system, a pre-heater for the fluidizing gas, an off-gas condenser and condensate receiver, a demister, and high-efficiency (AEC-type) filters for further off-gas cleanup. All process vessels are of stainless steel. Instrumentation consists of appropriate temperature and pressure sensors with local or panelboard readouts, controllers, recorders, and a data logger. Figure I-3 is a simplified drawing of the pilot plant for the denitration experiments.

The operability of the pilot plant was checked out in a series of six denitration runs at 300°C with uranyl nitrate. A wide range of operating conditions was used to determine any particle-size effects (i.e., growth or diminution trends in bed particle size). The initial bed in each

range 0.3 to 1.35M plutonium is independent of the initial plutonium concentration. Examination of a solution 1.35M plutonium in 3M HNO_3 revealed no spectra for trivalent or pentavalent plutonium.

2. Engineering Program

A fluidized-bed pilot plant has been constructed to study denitration of mixtures of uranium nitrate and plutonium nitrate solutions. Because of the broad experience with cylindrical columns in earlier denitration work, initial investigations are being done with a

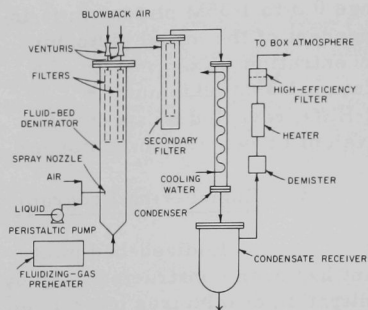


Fig. I-3. Equipment Components of 4-in.-dia Denitration Pilot Plant.

case comprised about 7200-8500 g of UO_3 with an average particle size of $162 \mu\text{m}$, and a bulk density of 4.2 g/cc . Feed solutions were 1 to 2.4M uranyl nitrate in 0.2 or 1.0M nitric acid. Feed rates ranged from 50 ml/min of 1M uranyl nitrate to 100 ml/min of 2.4M uranyl nitrate; these rates are equivalent to production rates of 22 and $105 \text{ lb } \text{UO}_3 / (\text{hr})(\text{ft}^2 \text{ reactor cross section})$, the upper value being just above the design goal of $100 \text{ lb}/(\text{hr})(\text{ft}^2)$. Fluidizing-air velocities were 1 to 1.5 ft/sec . Volume ratios of nozzle air to liquid in the feed ranged from 330 to 640. Runs were continued for as long

as 14 hr. Mechanical operability--that is, ease of startup and shutdown, ability to maintain uniform feed rate and fluidized-bed level, and sufficient heat input capacity for the design goal of $100 \text{ lb } \text{UO}_3 / (\text{hr})(\text{ft}^2)$ --was good in five of the six runs.

Results are considered preliminary and conclusions tentative because runs were of relatively short duration and since results for uranium-plutonium systems may differ from those for uranium alone. The design goal of $100 \text{ lb } \text{UO}_3 / (\text{hr})(\text{ft}^2)$ was reached when 2.0M uranyl nitrate was fed at about 100 ml/min. The effects on particle size were as follows:

(1) Slight particle growth occurred in the bed.

(2) Both fine (-200 mesh) and coarse material ($+8$ mesh) formed; fines constituted about 5% of the product, whereas the coarse fraction represented about 5-10% of the product.

(3) Similar particle-size distributions were found for product sampled at the overflow point and at the bottom withdrawal point. This indicates that good mixing was occurring in the bed.

The current program has given an insight into the characteristics of our denitration pilot-plant operation and has shown that the equipment and instrumentation are functioning properly. Work with uranium-plutonium is planned. Critically safe auxiliary items (e.g., a dissolver to permit recycle of $\text{UO}_3\text{-PuO}_2$ and a feed storage vessel) are being designed.

C. In-Line Analysis in Fuel Fabrication

The application of in-line nondestructive methods for analyzing critical properties of fuel during fabrication is expected to lower fuel

fabrication costs of the large number of fuel elements and subassemblies that will be produced in the LMFBR program. Rigorous specifications for ceramic uranium-plutonium oxide fuel have been set, but these may be relaxed when adequate experimental data relating the effects of various fuel properties to fuel performance are accumulated and evaluated. In this work, the specifications and associated precisions for Fast Flux Test Facility (FFTF) fuel have been selected as the starting criteria in evaluating analytical methods. The determination of Pu/U ratio and O/M ratio of fuel oxide, which will be part of any anticipated fabrication procedure, is being studied. In order to accommodate large-scale fuel production rates (or continuous processing), analyses must be performed rapidly. This report summarizes ANL work on the development of rapid, in-line analytical methods for determining these two ratios.

1. Determination of Pu/U Ratio

The most probable concentration of plutonium in oxidic FBR fuels is in the range from 15 to 25%. Analytical methods recommended in FFTF documents are for determining plutonium and uranium in aqueous solutions. Controlled-potential coulometry is the recommended method; an alternative procedure is X-ray fluorescence spectrometry utilizing an internal standard of yttrium in solution.

For the direct measurement of Pu/U ratios in oxide powder or pellet, the potentiality of X-ray fluorescence spectrometry can be inferred from the application of this method to the determination of various elements in certain industries such as copper ore processing and cement production. To apply the method to (U,Pu)O₂ fuel, problems of matrix effects (i.e., absorption and enhancement) must be evaluated.

The relationship of the atomic numbers between the pairs, thorium-uranium and uranium-plutonium, results in similarity of fluorescence and absorption characteristics and allows the use of thorium-uranium oxide as a stand-in for uranium-plutonium oxide, avoiding the hazards of handling plutonium. Secondary fluorescence or enhancement is likewise similar for the two pairs--in thorium-uranium oxides, the UL α emitted X-rays excite ThL α emission; in uranium-plutonium oxides, PuL α emitted X-rays excite UL α emission.

Mixtures of ThO₂ and UO₂ were prepared having UO₂ concentrations of 10, 20, 30, and 40 wt %. The relative intensities of ThL α and UL α fluorescence spectra were measured with a Norelco X-ray fluorescence spectrometer. The expected matrix effects of enhancement of ThL α and of absorption loss for UL α were observed. Further study will be required to define quantitatively the effects of crystallite size, particle density, and packing density. If calculation of these matrix effects is possible, the number of standard calibration samples required would be reduced drastically.

In work to increase the speed of analysis with the X-ray fluorescence spectrometer, 20-mil collimators were substituted for the 5-mil collimators originally used. Increased count rates were obtained along with adequate resolution of the thorium and uranium peaks. The count rate achieved for uranium (2×10^3 cps) under these conditions suggests that analysis of one pellet per minute is feasible. This analysis rate can accommodate a production rate of 900,000 pellets per day if the batch size is equivalent to 500,000 pellets. Further study is needed to determine if the analysis rate, batch size, and quality assurance criteria are compatible with the expected plant capacity.

2. Determination of O/M Ratio

The initial O/M ratio of (U,Pu) O_2 fuel material may have a major effect on changes in the fuel during irradiation and fuel performance. Present specifications for FFTF pellets are for an initial O/M ratio of 1.97 ± 0.02 . The recommended method of analysis for O/M ratio is based on the weight change upon heating a sample in a gas with controlled oxidation-reduction potential. This method is slow and destructive. A method based on measuring physical properties such as the lattice parameter would be rapid, nondestructive, and possibly adaptable for in-line use.

The U-Pu-O ternary system has been studied extensively by X-ray diffraction at Harwell, Karlsruhe, and various USAEC sites. When the O/M ratio is carefully controlled at 2.00, Vegard's relationship between UO_2 and PuO_2 has been demonstrated, i.e., a linear change of lattice cell size with a change of plutonium content was observed. A Vegard relationship between UO_2 and $PuO_{1.5}$ has not been fully established. The single-phase region (fcc) at room temperature extends at least up to a Pu/Pu + U ratio of 0.15 and perhaps up to a Pu/Pu + U ratio of 0.35.

Data have been located in the literature that relate the lattice parameter to the O/M ratio for ternary material for which adequate analysis for Pu and O can be presumed. At constant Pu/Pu + U, a linear variation of lattice parameter with O/M is shown; coefficients are about 0.5 pm (0.005 Å) per 0.02 O/M (the unit for the FFTF specification of precision is 0.02 O/M). Treating all of the literature data as one relationship with the constraint of the Vegard relationship for stoichiometric oxide produces the following relationship of lattice parameter (a_0), plutonium content (Pu) and O/M ratio (O/M):

$$a_0 = 6.1127 - 0.534 (\text{Pu}) - 0.321 (\text{O/M}) + 0.229 (\text{Pu}) (\text{O/M}).$$

For a 1% change of the O/M ratio, the change in lattice parameter is 0.55 pm (0.0055 Å), which is easily measured because it is about ten times the usual precision of lattice parameter measurements.

3. Conclusions

Evidence of the feasibility of rapid, nondestructive analytical methods for determining the Pu/U ratio of (U,Pu)O₂ FBR fuels has been obtained from the results of preliminary experiments and from literature information. Further experiments should demonstrate that adequate precision ($\pm 0.5\%$) can be achieved, should delineate the influences of particle size and density, and should define the potential of these methods for on-line application.

Determination of O/M by lattice parameter measurement with X-ray diffraction techniques has been supported by literature information. The method is currently in use by scientists defining phase diagrams and properties of the U-Pu-O ternary system. It has potential as an off-line analytical method applied to FBR fuel fabrication.

D. Adaptation of Centrifugal Contactors in LMFBR Fuel Processing

Large centrifugal contactors are presently being used at the Savannah River Plant (SRP) to recover uranium and plutonium from production-reactor fuels using a Purex process. (The Purex process employs multiple solvent extraction cycles to separate uranium and plutonium from each other and from fission products. The solvent is tributyl phosphate in a kerosene-type diluent, and the aqueous phases contain nitric acid.) Centrifugal contactors have demonstrated unique advantages over other contactors such as pulse columns and mixer settlers: high capacity relative to holdup volume, reduced radiation damage to solvent, rapid achievement of equilibrium operating conditions, and quick flushout of equipment at the end of a processing campaign.

Purex-type solvent extraction processes are now under development for processing of Liquid-Metal Fast-Breeder Reactor (LMFBR) fuels. The high plutonium content of these fuels and the reduced cooling time allowed before processing require modifications of the process and the operating equipment.

A program has been undertaken to extend the centrifugal contactor design of the SRP units to a configuration suitable for safe and efficient handling of plutonium in the plutonium isolation cycles during Purex solvent-extraction processing of LMFBR fuels. The principal advantage sought is an increase in nuclear safety by limiting the diameter of the unit to a critically favorable dimension, while maintaining a relatively high throughput. A high throughput can be achieved by using high rotor speeds as well as a long settling zone in the rotor to achieve increased residence times.

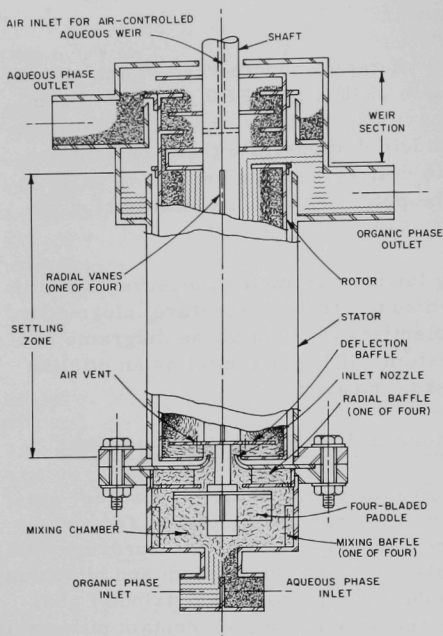


Fig. I-4. Experimental Centrifugal Contactor.
ANL Neg. No. 308-2377.

A centrifugal contactor has been designed for testing and is currently being fabricated. The main components are shown in Fig. I-4. The rotor has a 4-in. ID and is 15 in. in length and is supported by a shaft entering the top of the contactor. The ID of the stator is $4\frac{3}{4}$ in., which is critically safe for plutonium concentrations as high as 200 g/liter (assuming full water reflection and without credit for neutron absorption by any ^{240}Pu present). It is not expected that a plutonium concentration approaching 200 g/liter will occur in Purex flowsheets for which this type of contactor may be employed.

In the unit shown, an aqueous and an organic phase enter the mixing chamber located below the rotor. The phases are mixed by a paddle attached to the end of the rotor shaft. Radial baffles located just above the mixing chamber direct the mixed phases

into an orifice in the bottom of the spinning rotor, where they are quickly accelerated to rotor speed by four internal vertical vanes. The phases are separated by centrifugal force as they move upward through the rotor, with the heavy phase moving to the outside and a layer of emulsion floating between the clear heavy and light phases. A weir is provided for each phase, and the position of any unseparated emulsion is adjusted by air control to locate it between the light-phase weir and the opening to the heavy-phase weir. This feature (which was developed at Savannah River) permits operation over a broader range of phase density ratios and flow rates than could be achieved with a fixed weir. The separated phases are discharged through ports near the top of the rotor.

The rotor is supported only at the top in order to avoid problems that might be caused if bearings were operated in corrosive solutions. Accordingly, the length of the rotor and its operating speed are limited by the critical speed of the shaft and rotor assembly. At the critical speed, any vibration resulting from rotor imbalance is strongly reinforced and can lead to excessive deflection of the rotor, high stresses, and possible failure of the equipment. The present spindle assembly for the rotor can

accommodate a $1\frac{1}{4}$ -in. dia shaft. Calculations of critical speeds indicated that the rotor assembly would have a first critical speed of about 5400 rpm if the length of the rotor bowl was limited to 15 in. Since the generally recommended safe operating speed is about 70% of the critical speed, operating speeds of about 3600 rpm should be permissible with the proposed rotor.

The weir section occupies the upper 3 in. of the rotor length; the remaining 12 in. is available for use as a settling zone. The length-to-diameter ratio of three for the settling zone and the operating speed of 3600 rpm will extend the study of operating characteristics beyond the range of the SRP units, which have a settling-zone length of about 13 in., a rotor diameter of 10 in., and an operating speed of 1750 rpm.

A facility has been built in which experimental centrifugal contactors will be tested using various organic and aqueous streams. The facility is equipped with supply tanks for the aqueous and organic streams, pumps, constant-head tanks, and flowmeters. The spindle that supports the rotor will be driven through a belt by a dc motor to permit operation over a range of rotor speeds. The entire facility is enclosed in a ventilated hood to confine any organic or acid vapors released.

The testing program to be carried out with the above contactor is designed to establish separating capacities with an aqueous phase consisting of a nitric acid solution and an organic phase consisting of tributyl phosphate in refined kerosene or n-dodecane diluent. Performance data from these tests will be compared with performance data from tests of the Savannah River units. Additional tests will be made with inactive uranium feed solutions to evaluate the mass-transfer efficiency of the contactor.

The contactor design provides for the removal of the lower mixing section to permit replacement of the mixing paddle. One of the variables to be tested is the effect of different types of mixing paddles. In addition, it will be possible to replace the bottom section with a special housing that will permit an independently driven paddle to be introduced into the mixing chamber. This arrangement allows investigation of the effects of operating the rotor and the mixing paddle at different speeds.

The design of the ANL contactor also permits it to be converted into an annular mixing unit. In the latter design, the mixing paddle and mixing chamber are removed. The aqueous and organic streams enter through inlet lines in the upper part of the stator (i.e., through the contactor casing) and are mixed by skin friction as they flow downward through the annular space between the spinning rotor and the stator. At the bottom of the stator, four radial baffles convert some of the kinetic energy of the spinning fluid into pressure. The mixed phases flow into the rotor and are separated as is described above.

The principal advantages sought in the annular design are simpler fabrication, lighter weight (which may have a significant effect on critical speed for a rotor that has a relatively high length-to-diameter ratio), and potential hydrodynamic support of the spinning rotor by the fluid in the annular space.

Preliminary tests of the annular mixer design have been made with plastic units having 4-in. OD by 15-in. long rotors and $4\frac{1}{2}$ -in. and 5-in. ID stators. Throughput rates with water alone were as high as 11 gpm, depending on the size of the orifice in the rotor, the rotor speed, and the internal construction of the rotor (i.e., one of the rotors has a smaller flow area for the aqueous phase and therefore yields a lower throughput when other operating conditions are the same). Measurements of mixing power input made while the unit was mounted on a dynamometer test stand showed that the power input was high, indicating a high mixing intensity. Future studies of phase separation and mass transfer will allow contactor performance to be evaluated.

II. SODIUM TECHNOLOGY

The Division's effort in sodium technology is conveniently divided into three sections: Sodium Chemistry, Analytical Standards Program, and Engineering Development.

The sodium chemistry work was the initial activity for the Chemical Engineering Division in sodium technology, and for some time it constituted the major effort. Within the past year, however, there has been an increased Laboratory (and Divisional) involvement in the timely design and successful operation of the Fast Flux Test Facility (FFTF) and sodium-cooled fast breeder demonstration reactors; this involvement has led to increased emphasis on analytical development, particularly the establishment of national analytical standards, and on engineering development, including the development of monitors for impurities in sodium, methods for detecting and locating fuel failures in operating reactors, and methods of safe and effective maintenance of (contaminated) reactor systems. Such emphases have necessitated a reduction in the effort applied to the more basic chemical studies.

The current effort in sodium chemistry involves a study of oxygen- and hydrogen-bearing species in sodium, measurement of the heat of solution of oxygen in sodium, characterization of carbon- and nitrogen-bearing species in sodium, and determination of the solubility of xenon in sodium.

Analytical work includes the activities of the Analytical Standards Laboratory, notably, the development and establishment in the national sodium community of standard analytical procedures, and the development of a method for determining oxygen, carbon, and nitrogen in sodium by proton activation.

Engineering studies include development of monitors for the measurement of the activities in sodium of dissolved oxygen, carbon, and hydrogen and of a detector for the leakage of small amounts of water into sodium; investigation of methods for detecting and locating failed fuel; studies of the problems of radioactivity in reactor systems and their relation to maintenance procedures; and a study of the nature and control of sodium aerosols in reactor cover gas.

A. Sodium Chemistry

The program on the chemistry of liquid sodium is directed toward the development of a sound scientific foundation for understanding the behavior of sodium's common nonmetallic contaminants--carbon, nitrogen, oxygen, and hydrogen--so that analytical methods can be developed for these contaminants and potential corrosion problems in sodium systems can be predicted from existing corrosion data. Recent effort in the program

has been devoted to (1) elucidating the phase relations in the Na-Na₂O-NaOH-NaH system, (2) determining the heat of solution of oxygen in sodium, (3) determining the stability in sodium of disodium acetylide--a compound believed to be important in carbon transport, and (4) studying the interactions of nitrogen and calcium in sodium and thereby assessing the role of calcium in enhancing nitridation of steels in sodium systems. Included in the program is a research effort which does not fall in the above categories, but which provides information useful in fuel element detection and location (FEDAL) schemes, namely, determination of the solubility of xenon in liquid sodium.

1. Characterization of Oxygen- and Hydrogen-Bearing Species in Sodium

a. The Sodium-Rich Corner of the Sodium-Oxygen-Hydrogen Ternary System

This investigation seeks to understand the behavior of oxygen- and hydrogen-bearing species in liquid sodium. The results will directly assist in the development and evaluation of analytical methods for the qualitative and quantitative monitoring of oxygen and hydrogen impurities in sodium. In addition, information will be obtained that will provide a strong foundation for future investigations of cold trapping, caustic stress corrosion, mass transport, and other related topics. The initial effort is being directed toward the elucidation of the phase relations in the Na-Na₂O-NaOH-NaH system.

The problems associated with the reaction of sodium with O₂ and H₂ have been extensively studied in various laboratories. For the most part, the emphasis in these studies has been on safety considerations and on developing a broad understanding of the chemical and mechanical interaction of the reaction products with other LMFBR components. Details of the actual chemical reactions and the nature and distribution of the resultant species have received only limited attention. Nevertheless, several reviews¹⁻³ have recently been made of the available information on the phase relations that exist between Na, Na₂O, NaOH, and NaH. In each case, the conclusion was reached that essentially no unequivocal information is available on the Na-Na₂O-NaOH-NaH ternary system and that the respective binaries, i.e., the systems Na-Na₂O, Na₂O-NaOH, NaOH-NaH, and NaH-Na, have been determined only fragmentarily. Although the available information is sparse, it has served us as a basis for the construction of two very tentative but self-consistent versions of the Na-Na₂O-NaOH-NaH diagram. The assumption was made that either Na₂O-NaOH or NaOH-NaH is a quasi-binary section and, thus, that the Na-Na₂O-NaOH-NaH section of the larger

¹B. A. Shikhov, *Russ. J. Inorg. Chem. (English Transl.)* 12, 545 (1967).

²S. A. Jansson, in *Corrosion by Liquid Metals*, pp. 523-560, J. E. Draley and J. R. Weeks, eds., Plenum Press, New York (1970).

³J. L. Henry, U.S. Bureau of Mines, Albany, Oregon, unpublished work.

Na-O-H ternary can be treated independently. Also, the hydrogen partial pressure was considered to be sufficiently large so that NaH melts congruently. Both diagrams show a region of liquid immiscibility in accord with Shikhov.¹

Our experimental program is addressed to (a) determining which of the two diagrams is more reliable, (b) refining the selected diagram and (c) studying the interactions between hydrogen- and oxygen-bearing species in sodium at LMFBR temperatures. Emphasis will be placed initially on the Na-NaOH system because of its special pertinence to analytical methods development.

To determine which of the two diagrams is more reliable, heat-treated mixtures of Na, Na₂O, NaOH, and NaH will be examined at room temperature by X-ray powder diffraction techniques. A selection between the diagrams may be possible on the basis of the phases present and/or absent. Preliminary experiments are under way.

To refine the selected diagram and to study the hydrogen-oxygen-sodium interactions at elevated temperatures, the method selected is that of simultaneously determining (a) the activities of oxygen and hydrogen in the various phase fields and (b) the nature and concentration of the species in the vapor in thermodynamic equilibrium with the liquid and solid ternary phases. A correlation of these parameters with known additions of Na₂O, NaOH, and NaH to liquid sodium should provide insight into the nature of the interactions and delineate the phases and phase-region boundaries of the ternary system.

An apparatus for this purpose has been designed. The main component is a large (~1000 cm³) nickel Knudsen cell that is heated by a standard wire-wound furnace. Vapor from the cell effuses through several orifices (effectively converting the vapor into a molecular beam) and into a precision quadrupole mass spectrometer. A critical analysis of the mass data should provide identity information that is directly related to the particular solid and liquid phases present in the Knudsen cell. Also inserted into the Knudsen cell are oxygen- and hydrogen-activity probes. The outputs of the two probes will be monitored for the discontinuities that are produced by transgressions of the various phase-region boundaries.

b. The Heat of Solution of Oxygen in Liquid Sodium

Application of galvanic-cell methods for monitoring oxygen activity in liquid sodium was first proposed by G. W. Horsley in 1959. A systematic effort to use a solid electrolyte in the measurement of some of the thermodynamic properties of the sodium-oxygen system was started by Alcock and Stavropoulos⁴ in 1963, and has been continued by scientists at Brookhaven National Laboratory since 1967.

⁴G. P. Stavropoulos, Ph.D. thesis, University of London (1967).

In an effort to further our understanding of solutions of oxygen in sodium, work was started on the measurement of the heat of solution of oxygen in liquid sodium. This work involves measuring, as a function of temperature, the open-circuit reversible electromotive force of the cell $\text{Sn-SnO}_2/\text{ThO}_2\text{-Y}_2\text{O}_3/\text{O}$ (dil. sol'n in Na) in which the reference electrode is Sn-SnO_2 and the working electrode consists of a dilute solution of oxygen (1-100 ppm) in sodium, maintained at constant composition. For solutions as dilute as those studied, solute-solute interactions are insignificant and the solute-solvent affinity is strong; hence the heat of solution may be expected to be independent of oxygen concentration. Moreover, with the

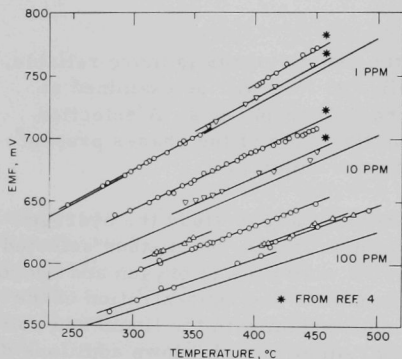


Fig. II-1. Experimental and Calculated Emf-versus-Temperature Data for the Cell: $\text{Sn-SnO}_2/\text{ThO}_2\text{-Y}_2\text{O}_3/\text{O}$ (dil. sol'n in Na). ANL Neg. No. 308-2378.

reasonable assumptions that Henry's law is applicable and that the heat of solution is nearly independent of temperature, thermodynamic considerations indicate that the cell emf should vary linearly with temperature. This linear relationship may be seen in Fig. II-1, where the data collected at ANL and elsewhere⁴ are presented. Also shown are curves for oxygen levels of 1, 10, and 100 ppm calculated with the aid of existing solubility information;⁵ these curves are given so that the oxygen concentrations at which the emf measurements were made may be estimated.

The experimental data for each curve were fit, by the method of least squares, to an equation of

$$(500\text{-}1000^\circ\text{K})\Delta G_f^\circ(\text{SnO}_2) = -(140.0 \pm 0.3) + (0.0511 \pm 0.0003) T \quad (1)$$

$$(500\text{-}1000^\circ\text{K})\Delta G_f^\circ(2\text{Na}_2\text{O}) = (200.9 \pm 3.0) + (0.068 \pm 0.002) T \quad (2)$$

the partial molar heat of solution of oxygen in sodium was determined to be 13.2 ± 0.1 kcal/mol. This value may be compared with values obtained in other studies: 13.1 ± 0.8 kcal/mol (average of four values) by Stavropoulos,⁴ 12.0 ± 0.2 kcal/mol (average of five values) by Minushkin,⁶ 11.2 kcal/mol from Eichelberger's solubility equation,⁷ and 12.8 ± 0.3 kcal/mol from an

⁵V. J. Rutkauskas, LA-3879 (1968).

⁶B. Minushkin, BNL-50207, p. 85 (1969).

⁷R. L. Eichelberger, AI-AEC-12685 (1968).

assessment⁸ of the solubility data of Rutkauskas⁵ and of Noden and Bagley.⁹ The agreement with the value derived from the latter solubility results leads to the suggestion that even at oxygen levels much larger than those studied here (the solubility of oxygen in sodium, e.g., is ~3000 ppm at 550°C) solute-solute interactions are negligible and dilute solution behavior is exhibited by sodium-oxygen solutions.

2. Characterization of Carbon- and Nitrogen-Bearing Species in Sodium

a. Carbon Chemistry

Carburization and decarburization of steels are corrosion phenomena known to occur in sodium systems. Disodium acetylide, Na_2C_2 , has been postulated¹⁰ to be the species responsible for carbon transport in liquid sodium-steel systems. To aid in evaluating this postulate, information on the thermal stability of Na_2C_2 in sodium was needed. Experiments which were made to collect the required data are described later.

The decomposition of pure Na_2C_2 (no sodium added) gives rise to gaseous sodium and solid carbon; according to the phase rule, the system is thus monovariant, and the extent of decomposition (as measured by the pressure of sodium in the system) is a function of temperature. However, the system becomes invariant in the presence of liquid sodium, and it can be in equilibrium only at one discrete temperature. Liquid sodium may become part of the system in two ways: by purposeful addition (as was done in this study) or by decomposition of "pure" Na_2C_2 until the pressure of sodium in the system equals the vapor pressure of pure sodium and sodium condenses. The invariant temperature is the same in either case.

Experiments to determine the invariant temperature have been of two kinds: X-ray and chemical. The X-ray experiments, described in the preceding report (ANL-7650, pp. 15-16), showed that (a) pure Na_2C_2 undergoes a tetragonal-to-cubic phase change when heated to 275°C, and (b) the cubic structure persists to at least 500°C. Thus, an invariant temperature above 500°C was indicated.

The chemical experiments involved heating copper or graphite-lined copper capsules containing 2 g of sodium and 0.1 to 0.2 g of Na_2C_2 to temperatures in the range 550-700°C, then cooling them and analyzing

⁸T. F. Kassner, D. L. Smith, "Calculations on the Kinetics of Oxygen Solution in Tantalum and Niobium in a Liquid-Sodium Environment," ANL-7335 (September 1967). The uncertainty limits for the heat of solution (± 0.3 kcal/mol) were not reported by Kassner and Smith; they were determined as part of the present study.

⁹J. D. Noden, K. A. Bagley, UKAEA report TN-80 (1958).

¹⁰C. Luner, H. M. Feder, F. A. Cafasso, in Proceedings of the International Conference on Sodium Technology and Large Fast Reactor Design, Argonne, Nov. 7-9, 1968, ANL-7520, Part I, p. 455 (1969).

the contents for acetylide. To avoid contamination from air, the capsules were loaded and welded shut in a helium-filled glovebox and heated in helium-filled furnaces; they were then returned to the glovebox, cut open, and placed in a vacuum system for chemical analysis. The results showed that Na_2C_2 is undecomposed in sodium that has been heated to 550°C for two weeks. At 600°C , 25% of the Na_2C_2 is decomposed after one week. At higher temperatures, the decomposition is faster: after two weeks at 650°C or one day at 700°C , essentially no acetylide is left. It appears, therefore, that the invariant temperature for the Na_2C_2 -Na system lies in the range 550 - 600°C .

b. Nitrogen Chemistry

The study of the chemistry of nitrogen in liquid sodium has two principal objectives. The first is to provide information on the existence, identification, and chemical behavior of nitrogenous species in sodium so that analytical methods can be developed for these species. The second is to elucidate the roles that these species play in transporting, through sodium, the nitrogen that nitrides reactor components.

To begin the program, a study of the interaction of nitrogen and calcium in sodium was undertaken. This approach was taken after a literature search showed that (a) nitridation of stainless steel in the presence of molten sodium is a genuine phenomenon and (b) the function of calcium as a nitrogen carrier in sodium is a common conjecture. An analogous carrier role could also be postulated for magnesium, since both alkaline earths are present in reactor sodium, and the known chemistries of their nitrides are similar. Ultimately, the program will also include studies to elucidate the roles of other selected nitrogenous species such as amide, nitrite, cyanide, cyanamide, and cyanate.

The experimental procedure for the nitrogen-calcium studies was, briefly, as follows. A solution of 1 at. % calcium in sodium, contained in a Type 304 stainless steel reaction vessel, was agitated under a constant pressure of 720 Torr of nitrogen gas. Gas absorption was followed gasometrically to determine the stoichiometry of the reaction. After the absorption curve was sufficiently defined (about one week), a filtered sample of the liquid sodium phase was withdrawn for determination of its calcium and Kjeldahl-nitrogen content. Several Type 304 stainless steel tabs that had been included in the original sample loading and that had been submerged under the sodium throughout the experiment were analyzed for nitrogen, and other constituents as desired.

The system for measuring nitrogen absorption consisted of a cylindrical reaction vessel and furnace well contained in a rocking furnace which, in turn, was connected to a constant-pressure gasometric manifold by means of flexible stainless steel tubing. The furnace assembly rocked

through a vertical position so that sodium in the cylindrical reaction vessel flowed a short distance up and down the vessel walls and tabs in the sodium always remained submerged. In each experiment, a new reaction vessel was used, so that there was no question of nitride carry-over from one experiment to another.

The following experiments have been conducted: (1) two experiments with 0.01 mol calcium in 0.99 mol sodium at 590°C; (2) one "dry" experiment (no sodium or calcium) at 590°C; (3) one blank experiment with 1.00 mol sodium (no calcium added); and (4) one experiment with 0.01 mol calcium in 0.99 mol sodium at 390°C. The results of the gasometric experiments are shown in Fig. II-2, where nitrogen uptake is plotted as a function of time. The two experiments with calcium-sodium at 590°C agreed within experimental error and are shown by one averaged curve. The results of the gasometric experiments are shown in Fig. II-2, where nitrogen uptake is plotted as a function of time. The two experiments with calcium-sodium at 590°C agreed within experimental error and are shown by one averaged curve.

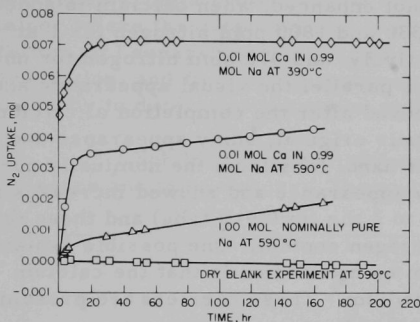


Fig. II-2. Nitrogen Absorption Curves at 390 and 590°C and 720 Torr. ANL Neg. No. 308-2379.

The "dry" experiment was designed to measure the nitrogen uptake resulting from nitridation, in the absence of sodium and calcium, of Type 304 stainless steel (the material of construction for the reaction

vessel and furnace well). The finding that no nitrogen was absorbed indicates that the steel, the only possible nitrogen absorber, was not nitrided. However, in experiments which were carried out in the presence of sodium or sodium-calcium solutions, significant nitrogen absorption was observed. For these experiments, the initial rise in the curves is interpreted as reflecting the reaction between nitrogen and dissolved reactive constituents (of which calcium is the major one) in the sodium, and the linear portions, in the 590°C experiments, as reflecting the absorption of nitrogen by the steel. The horizontal portion of the curve for the experiment with sodium-calcium at 390°C is a feature also exhibited by the curve for the "dry" experiment. Since the dry experiment at the higher temperature of 590°C showed that no nitridation of steel occurred, it is reasonable to expect that at the lower temperature of 390°C, the horizontal portion of the curve also reflects a period of no nitridation of steel.

The interpretation, offered above, of an initially rapid interaction between calcium in solution in sodium and nitrogen is analogous to that suggested by Addison and Davies¹¹ for lithium-sodium solutions and

¹¹C. C. Addison, B. M. Davies, *J. Chem. Soc. (A)*, 1827 (1969).

nitrogen at 400°C. In this connection, it is also noteworthy that the calcium does not remain in solution in sodium. Analysis of filtered samples of the solutions taken at the end of the experiments showed less than 10 ppm calcium. Also, a stainless steel tab that had been submerged in the solution did not reveal any significant calcium uptake. These facts are consistent with the interpretation offered above and with the hypothesis of relatively rapid formation, in sodium, of an insoluble calcium-nitrogen compound.

Analyses of submerged tabs showed that nitridation of Type 304 stainless steel is inhibited, not enhanced, when calcium is added to the sodium. Tab analyses showed 330 and 1800 ppm nitrogen for 1 at. % calcium and no added calcium, respectively, and 370 ppm nitrogen for untreated tabs. These analytical findings parallel the visual appearance and weight changes of the tabs. Tabs removed after the completion of calcium-enriched experiments emerged with their original, shiny appearance and with no change in weight. On the other hand, tabs from the nominally pure sodium runs emerged with a dull grey appearance and showed increases in weight. The weight increases were 1 to 2 mg (in 0.9-g tabs) and these agreed well with the analytical results for nitrogen content. One possible explanation for the inhibiting effect of calcium on nitridation is that the calcium removes nitrogen carriers from the sodium. These carriers are presumably impurities that have not yet been identified.

The amount of nitrogen that is ascribed to interactions with calcium and impurities in the experiments with 1 at. % calcium at 590°C is 3.37×10^{-3} mol. The difference between this amount of nitrogen and the corresponding quantity (5.6×10^{-4} mol) from the experiment with 1 mol of nominally pure sodium gives the amount of nitrogen interacting with calcium and an apparent overall Ca-N stoichiometry of $\text{Ca}_{1.78}\text{N}$.

The conclusion that emerges from these experiments is that calcium does not enhance nitridation, but, in fact, inhibits it. This finding tends to refute the conjecture cited in the literature that calcium, in sodium, functions as a nitrogen carrier in the nitridation process.

3. Solubility of Xenon in Liquid Sodium

The solubility of noble gases in liquid sodium is of considerable interest because of the use of sodium as a coolant in nuclear reactors. Helium and argon are generally used as reactor cover gases, and krypton and xenon are fission product gases which are released to sodium through fuel-pin cladding failures. The solubilities of helium,¹² argon,¹³ and krypton¹⁴ in liquid sodium have been measured previously. The study of the solubility

¹²E. Veleckis, G. Redding, "Solubility of Helium in Liquid Sodium," in ANL-7675, p. 64 (1969).

¹³E. Veleckis, R. Blomquist, R. Yonco, M. Perin, "Solubility of Argon in Liquid Sodium," in ANL-7325, p. 128 (1967).

¹⁴S. K. Dhar, "Solubility of Krypton in Liquid Sodium," in ANL-6900, p. 125 (1964).

of xenon was undertaken to provide data for evaluating schemes, currently under development at Argonne, for detecting and locating fuel-cladding failures in LMFBR systems.

The method used for the xenon solubility measurements is due to Grimes et al.¹⁵ This method incorporates several important features for determining very low solubilities of gases in liquids at elevated temperatures. Our adaptation of the method involves (a) saturating liquid sodium with natural xenon at a preselected temperature and pressure, (b) transferring a known portion of the saturated sodium to another container where the dissolved gas is stripped from sodium by sparging with helium, (c) separating the stripping gas from the gas mixture by selective absorption, and finally, (d) analyzing the remaining gas by gas chromatography to determine the xenon originally dissolved in sodium.

Solubility determinations were carried out as a function of both pressure and temperature. The pressure-dependence experiments were

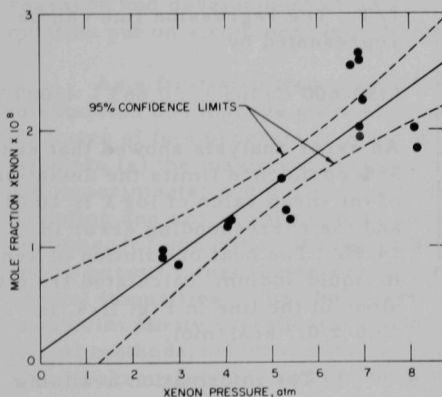


Fig. II-3. Pressure Dependence of the Solubility of Xenon in Sodium at 500°C. ANL Neg. No. 308-2380.

carried out at approximately 500°C and at xenon pressures ranging from 2 to 8 atm. The purpose of these experiments was to establish whether Henry's law is obeyed by solutions of xenon in sodium. The results are shown in Fig. II-3 where the mole fraction solubility of xenon, x_{Xe} (corrected to exactly 500°C), is plotted against the xenon pressure, P . The experimental data were fitted to a linear, two-constant equation and yielded a least-squares slope (the Henry's law constant) of $K_H = 2.8 \times 10^{-9} \text{ atm}^{-1}$. On the basis of statistical F-tests made on the value of the intercept and the linearity of the line, the displacement of the line from the origin was found to be insignificant; hence, the data

can be represented by Henry's law, $x_{Xe} = K_H P$. This can also be seen in Fig. II-3 by the position of the 95% confidence limits for the predicted mean values of x_{Xe} .¹⁶ A solubility relationship of the form $x_{Xe} = K P^n$, which includes Henry's law and Sieverts' law as special cases, was also tested. A linear least-squares analysis of $\log x_{Xe}$ vs. $\log P$ yielded a slope of $n = 0.9 \pm 0.3$, which is a further indication of the adequacy of a Henry's law representation of the solubility data.

¹⁵W. R. Grimes, N. W. Smith, G. M. Watson, J. Phys. Chem. 62, 862 (1958).

¹⁶These limits can be interpreted as follows. If repeated determinations of x_{Xe} are made at the same value of P , the probability that the average value of x_{Xe} will fall between these limits is 0.95. See, e.g., N. R. Draper and H. Smith, Applied Regression Analysis, p. 23, John Wiley & Sons (1966).

The temperature-dependence experiments were carried out between 350 and 600°C. The solubilities are expressed in terms of the Ostwald coefficient, λ , which is the volume of gas per unit volume of sodium, both the solute and solvent being at the temperature and pressure of the experiment. The Ostwald coefficient is related to the Henry's law constant by the equation

$$\lambda = (RTd_{\text{Na}}/10^9 M_{\text{Xe}})K_{\text{H}}$$

where R is the gas constant, T is the absolute temperature, d_{Na} is the density of liquid sodium,¹⁷ M_{Xe} is the atomic weight of xenon, and K_{H} is in ppb per atm. The results of these measurements are shown in Fig. II-4 as a plot of $\log \lambda$ vs. $1/T$. The regression line can be represented by

$$(350\text{--}600^\circ\text{C}) \log \lambda = 0.663 - 4500T^{-1}$$

An error analysis showed that at the 95% confidence limits the deviation of the mean value of $\log \lambda$ is ± 0.019 and the corresponding error in λ , $\pm 4.4\%$. The heat of solution of xenon in liquid sodium, calculated from the slope of the line in Fig. II-4, is $20.6 \pm 0.7 \text{ kcal/mol.}^{18}$

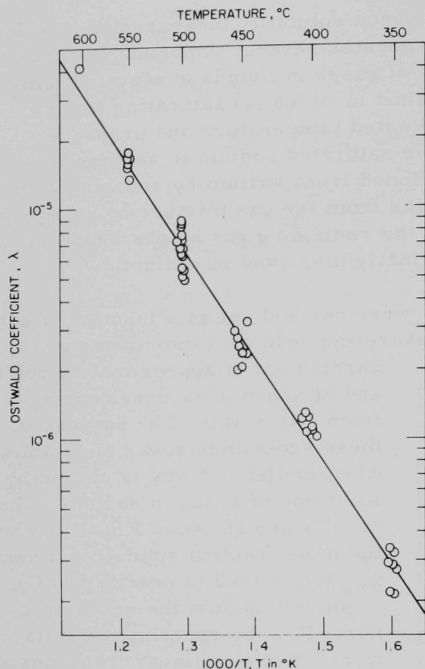


Fig. II-4. Temperature Dependence of the Solubility of Xenon in Sodium.
ANL Neg. No. 308-2381.

The information available on the solubility of noble gases in liquid alkali metals has recently been reviewed.¹⁹ The only other experimental study on the solubility of xenon in liquid sodium appears to be that of Mitra.²⁰ His procedure, however, contained experimental inconsistencies and yielded xenon solubilities 10^5 higher than those reported here. Xenon solubilities of that magnitude are inconsistent with expectations and with extrapolations based on the available data for other noble gases in sodium.

¹⁷J. P. Stone et al., NRL-6241, Naval Research Laboratory (Sept. 24, 1965); G. H. Golden, J. V. Tokar, ANL-7323 (August 1967).

¹⁸The heat of solution calculated from the slope of a plot of $\log \lambda$ vs. $1/T$ corresponds to $\overline{H}_{\text{Xe}}(\text{soln}, T, P) - H_{\text{Xe}}^{\circ}(\text{g}, T, P)$, where the standard state is defined to be that of 1 mole of ideal gas at temperature T in a volume equal to the molar volume of sodium, V_{Na} .

¹⁹E. L. Reed, J. J. Droher, LMEC-69-36, Liquid Metals Engineering Center (January 1970).

²⁰C. Mitra, Eng. Sc. Dissertation, Columbia University (1959).

A theoretical model that satisfactorily accounts for the measured solubilities of noble gases in liquid sodium has been developed at ANL (see Section V.A.1.c, this report). As shown in Fig. V-3, xenon solubilities predicted by this model are in good agreement with the measured solubilities.

B. Analytical Standards Program

Significant advances have been made in recent years in the development of analytical methods for impurities in sodium. Many of the impurities of interest to sodium coolant technologists are now being determined by more than one method. For example, the oxygen content of sodium is being determined in various laboratories by amalgamation, distillation, refractory-wire, electrochemical, activation, and uranium-gettering techniques. However, little effort has been made to standardize the methods in current use, and the result has been that impurity-sensitive (and often discrepant) experimental data from different laboratories have proven to be difficult to intercompare and interpret. If sodium technology is to advance rapidly, the research and development efforts of all major sodium technology contractors must be put on a common, intercomparable, and reliable basis.

As a first step toward achieving this goal, ANL has been requested to establish and manage an Analytical Standards Program. The long-term objective of this program is a set of specifications (RDT Standards) which stipulate (a) the maximum permissible impurity levels in operating reactor and experimental sodium systems (including cover gases); (b) standard sampling and analytical methods for determining impurity levels in such systems; (c) impurities that must be controlled to assure system integrity and to permit intercomparison of experimental data; and (d) methods to control impurities. The short-term objectives of the program are (1) a set of interim purity specifications and (2) a set of interim sampling and analytical methods, selected from existing technology, that are uniformly applied throughout the sodium technology community.

The short-term objectives are being met through the establishment of an Analytical Standards Laboratory, whose function is the management of, as well as participation in, the interlaboratory aspects of the standards program. Work related to meeting the long-range objectives has been directed toward development of analytical methods for which a need exists.

1. Analytical Standards Laboratory

The initial effort of the Analytical Standards Laboratory was an assessment of the steps necessary to meet the short-term goals of the program. The following conclusions were reached:

- 1) Sampling and analytical needs of the sodium technology community must be periodically assessed.

- 2) Sampling and analytical methods must be selected from existing technology to satisfy, as well as possible, the immediate analytical needs of the sodium technology community. Acceptable methods, their use, limitations, and range of applicability must be specified and updated whenever appropriate.
- 3) Areas of sampling and analysis, where additional development work is required, must be defined, and work in different laboratories in these areas must be coordinated. Continuous surveillance of new developments must be maintained so that interim methods may be updated or replaced as appropriate.
- 4) Uniform application of acceptable methods must be demonstrated by sample interchange programs.
- 5) Acceptable impurity limits for sodium and cover-gas systems must be defined and updated as warranted by new developments. Impurity-control methods also must be specified and periodically updated.

Successful implementation of the standards program requires the close cooperation of all laboratories participating in the sodium technology effort. Accordingly, ANL organized two advisory working groups to assist in implementing this program--a Reactor Standards Working Group and a National Standards Working Group. The two groups differed only in the scope of their interests. After the Reactor Standards Working Group had attained its objective of satisfying the immediate sampling and analytical needs of the reactor community, it was merged with the National Standards Working Group. This group is presently concerned with satisfying the sampling and analytical needs of the national R & D programs, and eventually will be concerned with establishing the specifications for the monitoring and control of impurities in sodium and cover-gas systems on a national scale.

With the assistance of these groups, ANL has (1) published a manual of procedures to be used for the analysis of sodium and cover-gas systems, (2) established interlaboratory exchange programs and schedules for the testing of sampling and analytical methods, (3) developed mechanisms for preparing and distributing test samples, and (4) drafted a set of purity specifications for sodium systems.

Besides the management activities in which ANL's Analytical Standards Laboratory is involved, laboratory work is also being done as part of the program. Analytical capability has been established for participating in the sample interchange programs, and laboratory work has begun on satisfying specific FFTF needs. The latter work involves (1) determining whether or not displacement of samplers a distance of ~100 ft from the point of interest (as may be done in FFTF) can lead to errors in analysis of sodium for oxygen and/or carbon and (2) designing and testing a prototype overflow sampler for FFTF.

2. Analytical Development

As noted above, the program requires research activities so that it may meet its ultimate objective. None of the methods presently specified for use are true standard methods. For most of the impurities found in sodium, reliable, accurate standard methods must still be developed. Consequently, ANL has undertaken their development within its own research program and plans to utilize other laboratories in the national program in this endeavor.

ANL's recent developmental effort has been directed toward the investigation of the following methods: (1) high-temperature gas chromatography as a means of separating radioactive species in reactor cover gas prior to radioactivity assays, (2) emission spectrographic analysis of a sodium aerosol, generated ultrasonically and excited by an induction-coupled plasma, as a means of determining trace metals in sodium, and (3) proton activation as a basis for a reference method for determining total oxygen, carbon, and nitrogen in sodium. The first two investigations are in preliminary stages of evaluation; the third is described below.

Reference Method for Total Oxygen, Carbon, and Nitrogen in Sodium. Reference methods are needed for the determination of oxygen, carbon, and nitrogen in sodium to establish the accuracy of other analytical methods. The reference methods must be specific, accurate ($\pm 10\%$), capable of determining concentrations of 0.1 ppm in sodium, and must provide samples free from contamination and segregation.

Activation with charged particles has become an important tool for the specific and accurate assay of oxygen, carbon, and nitrogen in the sub-parts-per-million range.²¹ Low-energy protons are of particular interest for our application because they do not appreciably activate sodium; thus, the need for separation chemistry is eliminated and the possibility of errors from contamination and segregation is reduced. Emphasis was, therefore, placed on the development of the proton-activation method.

The concept of determining oxygen, carbon, and nitrogen in sodium by proton activation is based on the following reactions: $^{18}\text{O}(\text{p},\text{n})^{18}\text{F}$, $^{13}\text{C}(\text{p},\text{n})^{13}\text{N}$ and $^{14}\text{N}(\text{p},\alpha)^{11}\text{C}$. Preliminary investigations of the feasibility of this method were performed by bombarding nickel-foil-covered NaF pellets spiked with known amounts of Al_2O_3 , C, and AlN. The results of these preliminary experiments gave the following projected sensitivities (in ppb): O, 50 ± 25 ; C, 20 ± 10 ; and N, 2 ± 1 . Precision was determined only for the $^{18}\text{O}(\text{p},\text{n})^{18}\text{F}$ reaction. The specific $^{18}\text{O}(\text{p},\text{n})^{18}\text{F}$ production was constant to within 2%.

²¹Proceedings of the 2nd Conference on Practical Aspects of Activation Analysis with Charged Particles, Liege, Belgium (EUR-3896 d-f-e), H. G. Ebert, ed. (1968).

Two potential interfering reactions were observed. They were $^{16}\text{O}(p,\alpha)^{13}\text{N}$ and $^{11}\text{B}(p,n)^{11}\text{C}$. As noted above, the carbon determination is based on the assay of ^{13}N and the nitrogen determination on the assay of ^{11}C . An experimental evaluation of the problems showed that the interference from ^{16}O will be serious only when the oxygen level is at least tenfold greater than the carbon level and that a correction for interference of ^{11}B can be made if the boron concentration does not exceed that of the nitrogen.

Deuterons and neutrons, if present in the proton beam, would also lead to interferences via the $^{23}\text{Na}(d,p)^{24}\text{Na}$ and $^{23}\text{Na}(n,\gamma)^{24}\text{Na}$ reactions. (Deuterons as D^+ are accelerated with the H_2^+ of the proton beam; neutrons arise from reactions of the beam with the beam tube and the collimators.) Deuterons were eliminated from the beam by employing a stripper foil (to change H_2^+ to H^+) and a magnet (to separate H^+ from D^+). Neutron production was minimized by focusing the proton beam through the center of the tube.

Having shown that adequate sensitivity could be achieved and that interferences from induced activities could be either circumvented or adequately controlled, a sampling/irradiation cell was designed. The cell permits irradiation of molten and well-stirred sodium and, thereby, circumvents the two major problems of proton activation, viz., surface activation rather than volume activation (due to the short range of the protons) and vaporization of sodium (caused by the heat generated in stopping the energetic proton beam). The cell consists basically of a nickel flow-through sampler. It is equipped with (1) noncontaminating valves that can be closed to isolate $\sim 20\text{ cm}^3$ of sodium and (2) a 6-mil nickel window that is coated on its inside surface with a thin (0.28 mg/cm^2) vapor-deposited layer of cobalt. (This coating, which is not activated by protons, was applied to prevent activities generated in the nickel from recoiling into the sodium.)

The experimental procedure involves the following steps: (1) bypass sampling of a sodium system by means of the sampling/irradiation cell, (2) proton activation of the molten and well-stirred sodium in the same cell, (3) transfer of the sodium to a counting cell, and (4) assay of the induced activities.

Initial experiments with molten sodium were directed toward testing of the cell and evaluating the problems involved in the determination of oxygen in sodium. Accordingly, two samples obtained from a sodium loop were bombarded with protons. Findings from these experiments indicated that (1) determination of oxygen in sodium by proton activation of molten, well-stirred sodium is feasible, (2) the cell functioned satisfactorily, (3) a detection limit of 1 ppm oxygen is possible with this cell design, and (4) the induced activities other than ^{18}F were ^{24}Na , ^{56}Mn and several copper isotopes.

The copper activities are believed to have been induced in the nickel window and to have recoiled into sodium via a breach in the thin cobalt layer that had been vapor-deposited on the window. The ^{56}Mn is believed to have been induced in the cobalt layer via the reaction $^{59}\text{Co}(n,\alpha)^{56}\text{Mn}$.

The production of the manganese and copper activities can be eliminated by the use of a window made from ^{58}Ni . A cell has been designed that incorporates such a window and also holds smaller samples. The smaller sample size (10 g rather than 70 g) should allow the detection limit to be lowered to 0.1 ppm of oxygen.

The work performed to date indicates that the proton-activation method for determining very low levels of oxygen, as required by the reference method, shows great promise. However, further development of this analytical method has been deferred because of budgetary limitations.

C. Engineering Development

1. Monitoring of Sodium Purity

a. National Meter Program

Argonne National Laboratory (ANL) has been given the responsibility of administering a National Meter Program involving the major sodium technology contractors in the United States. This program for development and application of sodium-purity monitoring stations is designed to (1) characterize the performance capabilities of present meters, (2) standardize the design and operational procedures and establish commercial availability for these characterized meters, (3) determine the requirements for meters on a continuing basis, as LMFBRs are advanced to a commercial status, and (4) upgrade performance or develop new meters, as required, to meet long-range performance goals.

Sodium technology contractors will participate in a coordinated test plan to determine the capabilities of existing impurity meters that have been developed for continuous monitoring of LMFBR sodium. Completion of this plan will result in the needed characterization of the meters in the shortest possible time by taking advantage of existing facilities. Impurity monitors in this program include oxygen, hydrogen, and carbon meters, and steam-generator leak detectors.

At present, the foremost goal of the program is to meet the needs of the Fast Flux Test Facility (FFTF) for commercially available oxygen and carbon meters by July 1, 1971. An additional goal is to have commercial hydrogen meters available by that date, or shortly thereafter, although this has not been listed as an FFTF requirement.

In addition to the meters themselves, prototype meter modules are being designed for FFTF; the modules include the individual meters and equipment for controlling sodium temperature and flow. A module is also being developed for equilibrating metal specimens with sodium to obtain measurements of the chemical activities of impurities for calibration of the meters. Both the meter modules and the calibration modules will have general utility in LMFBF systems. Commercial suppliers will be sought for these modules, as well as for the meters themselves.

b. Direct Measurement of the Activities of Impurities in Sodium

The objective of this work is the development of methods for calibrating impurity meters for carbon, oxygen, hydrogen, and, possibly, nitrogen, by independent chemical determinations of the impurity activities. Application of such methods in on-line meter-calibration devices is sought. The type of method under development generally involves equilibration of thin wires of a suitable metal in sodium. The equilibrium concentration of the impurity being determined is a measure of its chemical activity in the sodium. These methods are being developed in a cooperative program between the Chemical Engineering and Materials Science Divisions.

Laboratory development of a method for determining oxygen activity in sodium with vanadium wires is essentially complete. Measurements of the distribution coefficients for oxygen in the V-O-Na system for temperatures between 500 and 750°C, in 50-degree intervals, have been reported. Chemical activities of oxygen in sodium of up to 0.1 ppm at 500°C and up to 16 ppm at 750°C can be determined from measurements of the equilibrium concentration of oxygen in vanadium. The method will be used for calibration of electrochemical oxygen meters and for measurements of oxygen activities in operating sodium systems, including reactor systems.

Vanadium is also being considered as a detector metal for measuring hydrogen activity in sodium, and some distribution coefficient data have been obtained. Vanadium, iron, and iron alloys are being considered for carbon detectors. The wire-equilibration method may also be applied to nitrogen activity measurements; however, a suitable detector metal has not yet been found.

A significant effort is also being mounted to establish reliable, routine analytical procedures for the determination of the oxygen, carbon, nitrogen, and hydrogen in the equilibrated metal specimens.

The use of these methods for periodic on-line calibration of the various impurity meters requires that suitable equipment for specimen equilibration be designed and incorporated into a modularized package with the necessary devices for controlling sodium temperature and flow.

The module must be designed for rapid access to the specimens after equilibration. For radioactive sodium systems, this can be most easily accomplished by providing for complete drainage of the radioactive sodium.

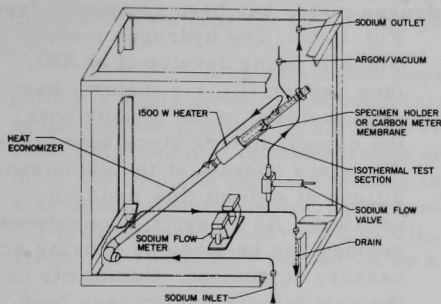


Fig. II-5. Module for Wire Equilibration and Carbon Meter. ANL Neg. No. 308-2382.

The conceptual design of the module is shown in Fig. II-5. Since the module heats sodium to temperatures up to 750°C , it will also be used as the carbon meter module (see Section II.C.1.d, below) by replacing the wire holder with the carbon-meter membrane system.

c. Oxygen Meter

The goal of this work is the development and prooftesting of an on-line oxygen-meter module for monitoring oxygen activity in the primary and secondary sodium systems of LMFBRs. Electrochemical oxygen meters will be evaluated and improved, where necessary, to provide (1) reliable and reproducible measurement of the oxygen activity in sodium and (2) continuous operation of the meter at temperatures up to $\sim 900^{\circ}\text{F}$ ($\sim 480^{\circ}\text{C}$). Testing and development of the meter-module components will be carried out at the Illinois site of ANL. Characterization of the meter will be through the national program, which will involve major LMFBR sodium technology contractors. Prooftesting of the module will be done on the Radioactive Sodium Chemistry Loop (RSCL), which is being installed at EBR-II on the primary sodium system. Operating experience gained at EBR-II and in the meter-characterization program will be useful in qualifying oxygen-meter modules for the Fast Flux Test Facility (FFTF) and for general LMFBR use.

A program being set up between ANL, Brookhaven National Laboratory (BNL), WADCO Corp., and the Zirconium Company of America (Zircoa) is expected to result in the commercial availability of oxygen meters by July 1971. The meter under development will have a gas reference electrode and an improved thoria-7.5 wt % yttria solid electrolyte produced by an isostatic pressing process. The improved electrolyte tubes should be commercially available by early 1971, which will allow a few months for characterization studies to be conducted by ANL and Westinghouse Advanced Reactor Division (WARD) before the meter-commercialization target date of July 1971. The electrolyte tubes will be of the size (1/4-in. dia) that is currently used in the Westinghouse version of the oxygen meter.

An oxygen meter is being installed on an existing sampling line at EBR-II for a rapid evaluation of the effects of direct beta and gamma radiation on the operation of the oxygen meter. The results of this test are

required to uncover possible detrimental effects of the radiation on cell output, stability, and life. The test is scheduled to begin in January 1971.

A preliminary layout of a prototype module for FFTF containing two oxygen meters and one hydrogen meter has been completed (see

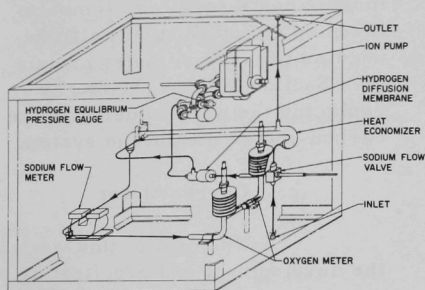


Fig. II-6. Oxygen-Hydrogen Meter Module.
ANL Neg. No. 308-2383.

Fig. II-6). The hydrogen meter, which is being developed at ANL (see Section II.C.1.e, below), has been included in the module with the oxygen meters since both types of meters operate at the same conditions of sodium flow and temperature. As a result, a considerable savings can be made by sharing accessory equipment. Comments on the preliminary design have been received from EBR-II and WADCO (FFTF) and these are being considered in the detailed design.

Designs of the heat exchanger and hydrogen-meter housing are complete. Oxygen meters for the modules have been ordered from Westinghouse. Preliminary layouts of the electrical and instrumentation packages for the modules have been made and reviewed.

A prototype module will be pretested at ANL-Illinois prior to prooftesting at EBR-II. A detailed schedule and job-assignment chart has been developed for installation of the module at EBR-II on the Radioactive Sodium Chemistry Loop (RSCL), Cell B.

Work is under way to characterize oxygen-meter performance at temperatures from 700 to 900°F (370 to 480°C). An apparatus which will be attached to the Test and Evaluation Apparatus (TEA) will provide for (1) calibration and testing of ten meters installed in series, (2) tests of the oxygen-hydrogen meter module, and (3) tests of the on-line calibration module (required in conjunction with items 1 and 2).

A conceptual plan for this apparatus has been developed. A design layout to determine space requirements and the preliminary design of a regenerative heat exchanger, heater, and cooler have been started.

d. Carbon Meter

This work involves the development and prooftesting of an on-line carbon-meter module for monitoring carbon activity in the primary and secondary sodium systems of LMFBRs. The meter housing and equipment for control of sodium temperature and flow are of the same design as those of the on-line calibration module (see Section II.C.1.b). Carbon-diffusion meters of the best available design will be evaluated for the meter

component of the module. Testing and development of the module components will be done at the Illinois site of ANL. The module will be proof-tested on the Radioactive Sodium Chemistry Loop (RSCL) of EBR-II. Operating experience at EBR-II will be used to provide recommendations for carbon-monitoring stations for FFTF and general LMFBR use.

A carbon meter developed by the United Nuclear Corporation (UNC) is being given prime consideration as the on-line meter component of the carbon-monitoring station. This meter is based on measuring the rate of diffusion of carbon through an iron membrane at 1200 to 1400°F (650-760°C). The carbon reaching the reverse side of the membrane reacts with a flowing, moist, hydrogen-argon gas mixture to form CO. The CO is catalytically converted to CH₄, and the CH₄ concentration in the gas stream is continually measured by a flame-ionization detector.

An understanding of the basic relationship of the carbon-meter response to carbon from various sources is a necessary part of the meter development. The UNC carbon-diffusion probe was immersed in sodium and its response to the addition of various materials and carbon species was tested. All-copper equipment (except for the probe) was used because copper is inert to carbon.

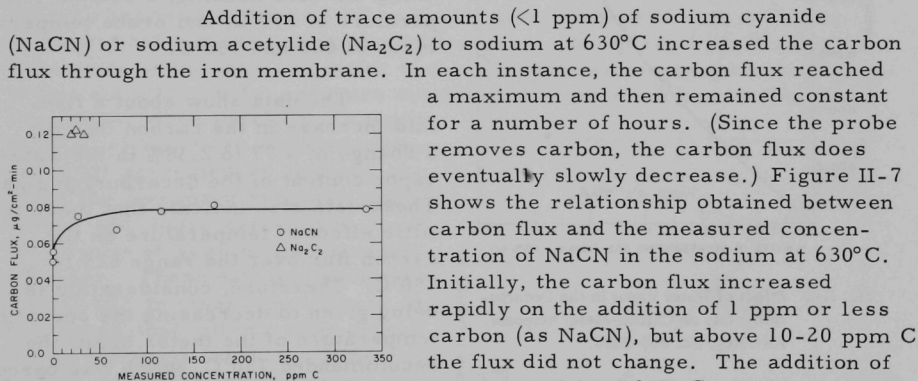


Fig. II-7. Carbon-Meter Response to NaCN and Na₂C₂ in Stirred Sodium at 630°C. ANL Neg. No. 308-2384.

Initially, the carbon flux increased rapidly on the addition of 1 ppm or less carbon (as NaCN), but above 10-20 ppm C the flux did not change. The addition of trace quantities of Na₂C₂ also increased the carbon flux, the initial increase being about twice that for cyanide. At the temperature of the experiment, acetylide decomposes rather slowly (see Section II.A.2.a) so that the variation of carbon flux as a function of acetylide concentration could not be readily measured. The further addition of sodium acetylide led to the formation of particulate carbon without noticeable increase in the analyzed acetylide content of the sodium (see Fig. II-7).

The response of the carbon meter was also tested by inserting a rod (5 in. by 1/4-in. OD) of low-carbon steel (1020) into the

sodium at 630°C. A few minutes after the rod was inserted, the carbon flux increased. After the rod was removed, the carbon flux reached a maximum and remained constant for 12 hr. When a Type 304 stainless steel rod was inserted, the flux decreased. The UNC meter housing, in which the probe is located and the sodium is heated, is itself made of stainless steel and can act as a getter to remove carbon from the sodium. Consequently, an inert liner for the meter housing is considered a possible improvement.

The effect of the water vapor content of the decarburizing gas on the carbon flux through the iron membrane was investigated. For these experiments 10% H₂-90% Ar, instead of the usual 5% H₂-95% Ar, was used as the decarburizing gas to ensure that the mixture, when combined with varying amounts of water, would prevent the oxidation of the iron membrane at the temperature employed. Figure II-8 shows the results obtained for experiments performed on a small pumped-sodium apparatus (Test and Evaluation Apparatus, TEA) using the UNC housing, a sodium temperature of 370°C, and probe temperatures of 625 and 750°C.

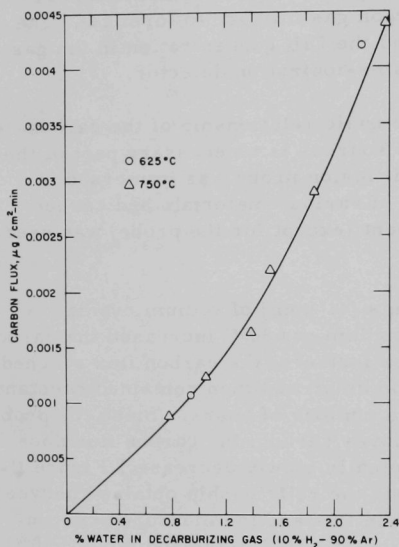


Fig. II-8. Effect of Water Vapor in the Decarburizing Gas on Carbon-Meter Response. ANL Neg. No. 308-2385.

The data show about a five-fold increase in the carbon flux for a change of 0.77 to 2.38% in the water vapor content of the decarburizing gas. These data also indicate that there is little effect of temperature on the carbon flux over the range 625 to 750°C. Therefore, consideration is being given to decreasing the operating temperature of the meter below the recommended 750°C, which was based

on static pot tests performed by the meter's developer, UNC; the decrease may be to a temperature as low as 650°C.

e. Hydrogen Meter

The goals of this program are the design, development, and proof-testing of an on-line hydrogen meter for measuring the hydrogen activity in primary and secondary LMFBR sodium systems. A diffusion-type meter being developed at ANL is being evaluated for the on-line hydrogen meter component of the oxygen-hydrogen meter module to be installed at EBR-II, as discussed in II.C.1.c. Operating experience at EBR-II will be used to provide recommendations for hydrogen monitoring for FFTF and general LMFBR use.

The hydrogen-activity meter being developed is an equilibrium diffusion-type monitor with a direct pressure readout of the activity of hydrogen in sodium. This direct readout is possible because the partial

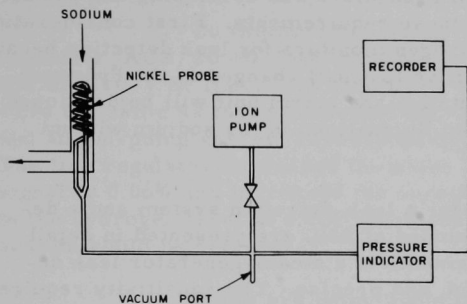


Fig. II-9. Hydrogen-Activity Meter.
ANL Neg. No. 308-2422.

pressure of hydrogen in equilibrium with sodium is related by Sievert's law²² to the hydrogen concentration in the sodium. The principal components of the meter (see Fig. II-9) are a high-surface-area nickel membrane that is immersed in the sodium, a pressure-measuring device such as a hot cathode-triode ion gauge, and an ion-pump vacuum system for periodic pumpdown. The nickel membrane operates at temperatures of 370 to 500°C.

A prototype of the ANL hydrogen-activity meter has been fabricated and is being evaluated in a newly constructed gas-flow test apparatus. The equilibrium hydrogen pressures of standard hydrogen-argon gas mixtures, equivalent to hydrogen concentrations in sodium of 0.5 to 4 ppm, were measured with a Varian Millitorr (hot cathode-triode) ionization gauge. Samples of the flowing gas were taken at the inlet and outlet of the chamber containing the nickel membrane; simultaneously, pressure measurements were made with the ionization gauge. When the Millitorr gauge is calibrated for use with hydrogen, excellent agreement is obtained between the measured hydrogen pressures, and those determined from the results of gas-chromatographic analyses. These data are shown in Fig. II-10. In other experiments, it was found that, after a step change in the hydrogen level, the time required to reach equilibrium was about 10 to 20 min.

These results indicate that the equilibrium diffusion-type meter with a calibrated Millitorr gauge has the desired characteristics for a hydrogen-activity meter.

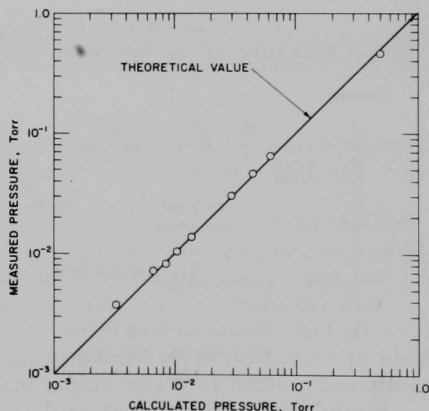


Fig. II-10. Hydrogen Activity Meter Calibration.
ANL Neg. No. 308-2421.

²² The concentration of hydrogen in sodium is given by $S = Kp^{1/2}$, where K = Sievert's constant and P = hydrogen pressure.

f. Detection of Leaks in Steam Generators

This work involves evaluating the requirements for a leak-detection system for LMFBF steam generators and developing and proof-testing a detection system to meet these requirements. First consideration is being given to diffusion-type hydrogen monitors for leak detection because they appear to be durable and sensitive to small changes in the hydrogen level of sodium. A signal-interpretation and alarm unit will be developed that accommodates normal hydrogen fluctuations in the sodium without giving false alarms.

The requirements for a leak-detection system and a description of the detector being developed at ANL are presented in detail elsewhere.²³ The principal requirements of a steam-generator leak detector are that it be sensitive, rapid, and precise. The sensitivity required to detect leaks that would lead to rapid perforation of adjacent tubes in a large generator (10^6 lb sodium/hr) is the capability of detecting a change of ~4% in the hydrogen level at a concentration of 0.1 ppm hydrogen dissolved in sodium.

The in-sodium hydrogen monitor being developed for leak detection is based on the diffusion rate of hydrogen through a nickel membrane operated under a dynamic vacuum. A vacuum (10^{-6} to 10^{-8} Torr) is drawn at a steady rate by an ion pump; thus, a hydrogen-activity gradient develops from the sodium side to the vacuum side of the membrane and results in the diffusion of hydrogen through the membrane.

The rate of hydrogen diffusion through the membrane, a direct measure of the hydrogen concentration in the sodium, will be determined by monitoring the current to the ion pump. This leak detector is shown schematically in Fig. II-11.

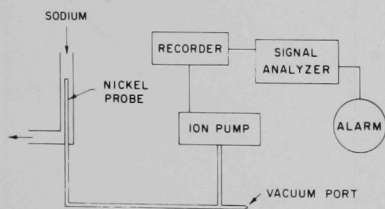


Fig. II-11. On-Line Ion-Pump Hydrogen Detector. ANL Neg. No. 308-2420.

A prototype of the leak detector has been installed on a pumped sodium system (Sodium Analytical Loop, SAL). Tests of this unit have indicated that the detector readout signal is quite stable when the ion-pump power supply is operated off a noise-free 110-V ac line. Further tests have shown, however, that the stability of the detector

readout signal is strongly affected when other appliances are being operated off the same 110-V line. Typical ion-pump current readings, taken at

²³"Sodium Technology Quarterly Report, January, February, March 1970," ANL/ST-2, Argonne National Laboratory (July 1970).

1-sec intervals, showed that the noise level was about 2.3% of the recorded signal of $17 \mu\text{A}$, a current reading equivalent to ~ 0.1 ppm hydrogen in sodium.

To improve the signal-to-noise ratio, a Sorensen ac line regulator (ACR, $\pm 0.1\%$) was installed between the ion-pump power supply and the 110-V ac line. The conditions under which the regulator was tested were the same as those described above--an irregular 110-V line voltage and an ion-pump current corresponding to ~ 0.1 ppm hydrogen in sodium. The line regulator decreased the noise level from 2.3% of the recorded signal to 0.06% and increased the sensitivity to an extent that a 4% change in the hydrogen level at a concentration of 0.1 ppm hydrogen dissolved in sodium could be detected.

Plans are being made to supply an ANL hydrogen-meter leak detector for the Sodium Component Test Installation at the Liquid Metals Engineering Center for use in their test of the Atomics International steam generator, which is scheduled for spring or summer of 1971.

Work is also under way to develop a leak-detection system for the secondary sodium system at EBR-II.

2. Failed Element Detection and Location (FEDAL) Systems and Radioactive Repair Engineering

a. FEDAL Systems

Requirements for Detection Systems. Fuel failures in non-vented fast-reactor oxide fuel elements in sodium-cooled reactors may be characterized as follows:

Type 1. Cracks or pinholes in the cladding, which allow fission gases to escape either intermittently or continuously.

Type 2. Failures in which sodium coolant enters the fuel element through a cladding defect. The sodium can subsequently be expelled or, if the defect is large enough, the sodium may continuously wash the oxide, carrying with it fission products that have leached from the fuel.

Type 3. Failures that allow particles of fuel oxide to escape to the coolant. This type of failure would not be likely to occur spontaneously but would probably result from a failure that started with sodium-oxide contact and would progress because of a combination of chemical attack and flow erosion of the oxide.

Type 4. Fuel meltdown, which would occur when coolant flow was diminished and power output maintained.

The present mode of operation of sodium-cooled reactors is to shut down and correct Type 1 failures. A charged-wire detector (called the Fission Gas Monitor at EBR-II), which is based on the detection of gamma-emitting daughters of ^{88}Kr , ^{89}Kr , and ^{138}Xe , has been the major instrument used to detect Type 1 failures. There has been no routinely used location system, although "tagging" by incorporating mixtures of stable isotopes of xenon inside the fuel-element jacket is being used for experimental fuels in EBR-II.

Commercial LMFBRs may continue to operate with Type 1 failures; in fact, some reactor concepts include the use of vented fuel, from which fission gases escape continuously. Unscheduled shutdown of commercial plants would result from more serious types of fuel failures: propagation of failure from pin to pin, blocking of coolant flow channels, and washout of oxide fuel from the cladding. For less serious failures, adequate information is not available on how much dispersion of radioactive fission products is tolerable in operating fast-reactor systems.

One of the urgent needs in the overall LMFBR program is to test oxide fuels to failure and beyond, i.e., beyond the appearance of a pinhole or crack that allows escape of gas. For these tests, which might be conducted either in EBR-II or FFTF, a detection system is needed to monitor the failure while it is progressing. Data from a FEDAL system with diagnostic capability is necessary to evaluate failure experiences and to build up fuel-reliability information under conditions where fuel elements are run beyond failure. A fuel-failure detection system is needed that will distinguish between cladding defects that release gas only and serious failures in which leaching of the fuel by sodium occurs. A delayed-neutron monitor should detect extensive washout of oxide particles from the cladding. However, this device, which is designed to protect the reactor and is presently in use at EBR-II, provides little capability for determining the extent of leaching of the fuel by sodium because of its low signal-to-noise characteristics prior to extensive washout of particles.

In-Sodium Monitors for Fuel-Failure Detection. The in-line application of gamma spectrometry for analysis of fission-product isotopes in primary sodium is hampered by the interference from sodium-activation products, mainly sodium-24. Therefore, the major problem to be solved is the development of separations methods that are adaptable to in-line monitoring equipment.

Three approaches to sodium-radioisotope separations have been considered: (1) Elements more volatile than sodium, including cesium and rubidium, could be separated from sodium by an in-line, multistage vacuum distillation column that greatly increases the ratio of cesium and rubidium to sodium-24 in the vaporized product. (2) Fission and corrosion products could be extracted into a second liquid phase, e.g., lithium, that is

circulated and counted; this second phase accumulates the nonvolatiles when the volatiles, including sodium, are distilled from it. (3) Iodine in sodium could be determined from the rate of generation of its xenon daughter, a gas which is sparged out of the sodium and counted. Current effort is being directed primarily toward developing the iodine-monitoring concept into an in-line monitoring device.

The steps involved in monitoring iodine in the sodium would be the following: (1) sampling of the reactor sodium in a flow-through sampling and sparging cell; (2) sparging the sample with helium (containing a small amount of inactive xenon as a carrier) in a gas recirculation loop to strip the sodium of most of the xenon that was present at the time of sampling; (3) trapping and discarding the xenon stripped in step 2; (4) allowing iodine in the sample to decay for a predetermined time to allow buildup of xenon daughters; (5) re stripping the sodium of xenon gas with recirculating helium containing added inactive xenon; and (6) trapping and assaying the xenon produced from iodine decay. Assuming that the transfer of xenon from the sodium to the xenon trap is essentially complete, the concentration of iodine in the sodium phase is calculable from the measured xenon activity, decay constants of the isotopes in the mass chain selected, and the times involved in the various steps.

Of the xenon activities considered for assay in reactor application of the iodine-monitor concept, the 15.6-min ^{135m}Xe isotope is of primary interest. Its precursor, ^{135}I (6.7 hr), has a long enough half-life so that its escape fraction to the coolant through a cladding leak should be significantly greater than that of delayed neutron precursors, but its half-life is not so long that buildup of activity in the coolant would interfere with the detection of subsequent fuel failures. In addition, the half-lives of the ^{135}I precursors, 1.9-sec Sb and 29-sec Te, are short enough so that they will not complicate the ^{135m}Xe assay.

Location Systems. A number of concepts for locating failed fuel have been devised. Xenon tagging, which is presently being used for experimental fuels in EBR-II, will probably not be applicable in future reactors operating with vented and/or defective fuel. Several other concepts, which were evaluated for use by the FFTF Project, involve the disengagement of fission-gas bubbles from sodium. These concepts have proven to be difficult to implement because of the complexities arising from the presence of a line extending from the top of each fuel assembly to the processing equipment.

For noncontinuous operation of a location system, a small gas trap could be built into each fuel assembly. In its simplest form, this trap would be a small, closed dome placed over the outlet of each fuel assembly, but attached to it. The gas trap would be designed to be inefficient at normal sodium velocities and would function only at very low

sodium velocities, such as those existing at reactor shutdown. Two factors contribute to a gas release during reactor shutdown: (1) the pressure outside the pin is reduced when the sodium velocity is reduced, and, as a result, gas is released either from a fuel defect or from the vent while pressure balance is being achieved; and (2) experience with oxide fuel indicates that a burst of gas is also released from the oxide matrix as the fuel cools.

If cladding leaks (either small, continuous gas leaks or large, serious leaks) are present at the end of the reactor operating cycle, the fuel-assembly gas trap should contain quantities of isotopes such as ^{88}Kr (2.77 hr), $^{85\text{m}}\text{Kr}$ (4.36 hr) and ^{135}Xe (9.3 hr). The gas trapped in each dome would be sampled with a "sipping" tool attached to the already existing refueling mechanism, and only one line would be used to route the gas samples, in turn, from the sipping tool to a shielded-detector site. Other ways of utilizing the sipping technique are under consideration.

b. Maintenance and Repair

The primary system of an LMFBR becomes radioactive with radioisotopes from activation of structural materials and sodium and from fuel sources, and the spread of this radioactivity throughout the primary system is expected to cause serious maintenance problems. Plans for the research and development work required to evaluate these maintenance problems have been formulated; the program will emphasize the use of EBR-II. The plans include work in the following categories: monitoring and surveillance, activity-level prediction, decontamination and maintenance procedures, and activity-level control methods.

There are two trends in design and proposed mode of operation of future LMFBRs that will lead to primary system contamination levels greater than those presently existing in EBR-II. (1) The temperature levels will be higher, which will increase transport rates of activated corrosion products. (2) Reactors will continue to operate with fuel elements that have lost hermetic seals; thus, some fission products normally contained within the cladding could distribute throughout the primary system. The higher levels of radiation are expected to cause increased difficulties in maintenance, and the severity of these maintenance problems is related to the specific radiation levels in existence in the area of maintenance work.

The radiation levels that will be encountered in future reactors cannot, at present, be predicted with any degree of certainty because the transport and deposition processes are very complex and complete theories for prediction do not exist. This information can be gained only by reactor experience, in which the radiation levels are monitored as temperatures are increased and the reactor is operated with some failed fuel in the core. Valuable insight into some of the problems can be gained by studying the spread of radioactivity in EBR-II. To use EBR-II for this

purpose, certain plant changes would have to be made and experiments carried out. These activities are as follows: (1) develop and implement standard methods of analysis for examination of contaminated surfaces taken from the reactor (these surfaces may be those of tabs inserted for this purpose or of components taken from the primary sodium system or from the analytical cold trap); (2) gain access to the shell side of the intermediate heat exchanger for deposition measurements; (3) develop and execute a plan for the use of tabs as a tool for measuring system contamination during periods of operation with failed fuel; (4) conduct experiments using reactor sodium to investigate the transport of activated corrosion products; (5) remove and analyze circulating particulates or measure their effects indirectly; (6) investigate methods for moving fixed activity in the reactor; and (7) use the cold trap or the analytical cold trap to investigate methods for removal of activity from sodium.

3. Nature and Control of Sodium Aerosol

The presence of sodium aerosol in high-temperature reactor cover gas can interfere with the movement of control-rod drive units, shafts, and other mechanical parts of the reactor, clog the gap between moving parts, and transport fission products and other impurities from the sodium phase to the cover-gas phase.

At temperatures above $\sim 300^{\circ}\text{C}$, most of the sodium transported in a cover gas will leave the sodium pool as sodium vapor. If the interface temperature exceeds the cover gas temperature by more than 50°C , most of the sodium vapor will be condensed to aerosol within a few millimeters of the interface. Convective recirculation of cooled aerosol from the cover gas back to the hot sodium surface will promote continued transport of sodium vapor from the pool surface to the aerosol particles. At the higher sodium-pool temperatures, it is expected that processes of agglomeration and gravitational settling will control the concentration and size of the aerosol. The present program, which involves both calculational and experimental studies, has the objectives of determining aerosol properties, investigating the mechanism of aerosol formation, and developing methods for aerosol control.

a. Calculational Studies

The sodium aerosol characteristics in the cover gas over the sodium pool will be controlled principally by the following process mechanisms: (1) heat transport, (2) mass transport, (3) nucleation, (4) agglomeration, and (5) gravitational settling. The development of models based on combining these process mechanisms will help to define the scaling laws of the overall process. Such models are needed to determine the value of small-scale laboratory experiments and the need for full-scale tests.

Heat-transport calculations have indicated²⁴ that most of the condensation to aerosol will occur close to the sodium surface.

Sodium vapor that has evaporated from the surface of the sodium pool will be cooled by natural convection in the cover gas. Most of the sodium vapor will condense on existing aerosol particles and cause them to grow. As these particles are removed either by gravitational settling or cover-gas circulation, new particles will be created by nucleation processes. Three processes are possible: nucleation on foreign particles, nucleation on ions, and spontaneous nucleation. Since no experimental data were found for nucleation processes of metal vapors, a calculational study was undertaken to examine these three processes as applied to sodium aerosols and a comparison was made with experimental data for water vapor. This theoretical treatment is reported elsewhere.²⁵

b. Experimental Studies

Initial experimental studies were directed toward measurements of sodium-aerosol concentrations in argon cover gas over a sodium pool at various temperatures (the apparatus is described in a progress report).²⁴ Because of experimental difficulties with loss of aerosol in the sample lines, the values obtained are considered to be only lower limits. The measured aerosol concentrations were compared with sodium-vapor concentrations, calculated from the properties of saturated sodium vapor for the same temperatures. These data are given in Table II-1. Both the calculated vapor concentration and the measured aerosol concentration are based on the volume of cover gas at 1 atm and 25°C. In spite of the experimental difficulties, the results indicate that the sodium aerosol concentration can exceed the concentration resulting from the vapor pressure by a factor greater than 9. An extremely high aerosol concentration, 35 g/m³, was measured above the sodium at 500°C.

TABLE II-1. Sodium Aerosol Concentration in Argon Cover Gas

Run	Sodium Temp. (°C)	Measured Aerosol Conc. (g/m ³)	Calculated Vapor Conc. (g/m ³)
NAF 1	200	0.00022	0.000168
NAF 2	300	0.0048	0.0174
NAF 3	403	4.6	0.490
NAF 4	500	35	5.06
NAF 5	600	plugged line	33.4

Preliminary measurements of the particle-size distribution of sodium aerosol in argon over sodium at 400°C have been made with a Casalla jet impactor. The results indicated that the mass mean diameter was ~4 μm, i.e., 50 wt % of the sodium aerosol was present as particles having diameters less than 4 μm.

²⁴"Sodium Technology Quarterly Report, January, February, March, 1970," ANL/ST-2, pp. 3-12 to 3-16 (July 1970).

²⁵"Sodium Technology Quarterly Report, July, August, September 1970," ANL/ST-4 (December 1970).

III. MATERIALS CHEMISTRY AND THERMODYNAMICS

A. High-Temperature Thermodynamic Studies

The objective of this program is to obtain phase-diagram, thermodynamic, and chemical data that can be used to interpret and evaluate performance of fast-breeder-reactor fuels. This information will aid in understanding and in selecting methods for control of sodium-fuel interactions, fission-product distribution in the fuel, cladding attack by corrosive fission products, plutonium segregation, and fuel swelling. In addition, these data will help to identify phases formed in fuel under operating conditions and to choose additives for controlling the chemical potentials of fuel anions and those fission products which are deleterious to prolonged fuel-pin lifetimes.

The high-temperature investigations of U-Pu-O, U-Pu-O-Na, and U-C-O fuel-fission product-sodium systems include mass-spectrometric vapor pressure measurements, phase-diagram studies, and activity measurements by transpiration experiments.

1. Volatilization Studies of Uranium-Plutonium Oxides by Mass Spectrometry

The mass-spectrometric investigation of single-phase $(U_{0.8}Pu_{0.2})O_{2-x}$ material has been completed, and a paper entitled "A Mass Spectrometric Investigation of the Volatilization Behavior of $(U_{0.8}Pu_{0.2})O_{2-x}$ "¹ has been published. A summary of this study follows:

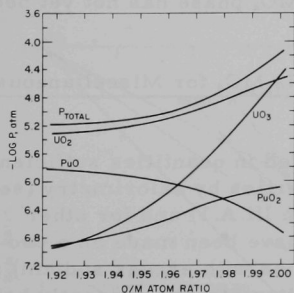


Fig. III-1

Partial Pressures of the Vapor Species over $(U_{0.8}Pu_{0.2})O_{2-x}$ at 2241°K.

The variation of the ion intensities of UO^+ , UO_2^+ , UO_3^+ , PuO^+ , and PuO_2^+ (the only species detected) as a function of temperature was determined using an ionizing electron energy of 15 eV for UO_3^+ and PuO_2^+ and 11 eV for PuO^+ , UO^+ , and UO_2^+ . The partial enthalpies of sublimation in the vapor species, determined by the second-law method, are 123.43 ± 1.69 , 139.41 ± 1.81 , 146.25 ± 1.67 , and 158.47 ± 1.98 cal/mol for the vapor species PuO , PuO_2 , UO_2 , and UO_3 , respectively. Since UO^+ appears to result primarily from fragmentation of other vapor species, data for it have been omitted. The partial pressures derived from the experimental data at 2241°K are shown in Fig. III-1 as a function of the O/M ratio for the solid phase.

¹J. E. Battles, W. A. Shinn, P. E. Blackburn, R. K. Edwards, Plutonium 1970: Proceedings of the Fourth International Conference on Plutonium and Other Actinides, Nuclear Metallurgy, Vol. 17, part II, pp. 733-742, The Metallurgical Society of AIME.

2. Phase and Reaction Studies of U-O-Na and U-Pu-O-Na Systems

Interaction of sodium coolant with reactor fuel could cause fuel swelling and cladding rupture in the event of a breach in the cladding. The severity of the problem may determine how long failed fuel elements can be left in the reactor core and whether or not failed fuel elements can be stored in the reactor sodium coolant.

Some of the objectives of this study and the progress that has been achieved thus far in meeting them are given below.

a. Na-O-M Phase in Equilibrium with Sodium and Mixed Oxide

Pepper et al.² stated that Na_3UO_4 is the Na-U-O phase that exists in equilibrium with sodium and UO_2 in the temperature range 600 to 1000°C. According to their X-ray data, it has a face-centered cubic structure with $a_0 = 4.79\text{-}4.80 \text{ \AA}$. Before working with mixed oxides, we confirmed this by detecting a fcc phase ($a_0 = 4.78\text{-}4.79 \text{ \AA}$) in equilibrium with sodium and UO_2 in products of reactions at 750 and 800°C. Phase relations were also determined for other U-O-Na compounds (see Section III.A.3 of this report).

Experiments were conducted with mixed oxides with a Pu/(U + Pu) ratio of 0.198. A face-centered cubic phase, $a_0 = 4.78 \text{ \AA}$, was found to have formed in the presence of sodium and the MO_{2-x} phase in reactions at 800, 905, and 950°C. The similarity of these X-ray data to those for Na_3UO_4 indicates that the phase is Na_3MO_4 , where M stands for uranium and plutonium. The Pu/(U + Pu) ratio of the Na_3MO_4 phase has not yet been established.

b. The Preparation of Na_3UO_4 and Na_3MO_4 for Miscellaneous Purposes

Preparations of Na_3UO_4 are needed in quantities sufficient for the establishment of its thermodynamic properties by calorimetry (see Section III.C) and mass spectrometry (see Section III.A.1) and for other purposes. Single-phase preparations of Na_3UO_4 have been made on a two-gram scale by reacting Na_2O and UO_2 (sometimes with excess sodium) at 800°C in nickel capsules that are welded shut. Attempts are currently being made to duplicate the process on a 70-gram scale. When the latter are successful, attempts will be made to produce Na_3PuO_4 and $\text{Na}_3(\text{U,Pu})\text{O}_4$ on a similar scale.

In an attempt to establish the melting point of Na_3UO_4 , a sample of single-phase Na_3UO_4 was heated for 10 minutes at 1425°C in a

²R. T. Pepper, J. R. Stubbles, C. R. Tottle, Appl. Mater. Res. 3, 203 (1964).

nickel capsule. Metallographic examination of the product showed that, instead of melting, the Na_3UO_4 had sintered.

In addition to the research on Na_3MO_4 described above, studies are planned on the sodium-fuel reaction mechanism and on direct measurements of fuel O/M ratios in equilibrium with Na_3MO_4 and sodium. An X-ray lattice-parameter measurement of the fuel is being explored as a method to obtain the fuel O/M composition.

3. Mass-Spectrometric Study of Sodium-Fuel Interaction

The objective of this study is to obtain equilibrium thermodynamic data on the products of reaction between sodium and fuel. In particular, the studies are concerned with determination of the oxygen and sodium partial pressures (activities) in equilibrium with the reaction product, liquid sodium, and $(\text{U,Pu})\text{O}_2$. Knowledge of the sodium and oxygen partial pressures will permit us to calculate the O/M ratio below which reactions will not occur.

After initial tests to establish if oxygen and sodium could be measured with the spectrometer, we ran two series of experiments on Na_3UO_4 . In the first series, it was found that a large portion of the sample was lost by effusion from the Knudsen cell at 900-1060°C and that initially only sodium was detectable. After the sample had dissociated for some time, the sample lost both oxygen and sodium vapor. The residue at the end of this experiment was practically all UO_2 . Thus, near the end of the experiment, oxygen pressures could also be measured. However, to measure both sodium and oxygen, one must study regions of the U-O-Na system removed from the region of interest.

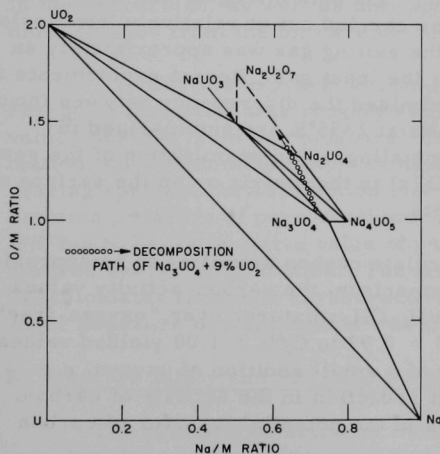


Fig. III-2. Phase Relations in the U-O-Na System.

In the second series of experiments, we again measured pressures in samples that were initially Na_3UO_4 . In addition, the sample material was periodically analyzed by X-ray diffraction to determine the condensed phases present. The data from Section III.A.2 and these X-ray data were combined to construct the phase diagram in Fig. III-2. In these measurements, the sample continuously changed composition as sodium was lost, moving material into regions richer in oxygen and uranium (along the broken line in Fig. III-2). We continued these

experiments until we reached a three-phase region (tentatively identified as $\text{NaUO}_3\text{-Na}_2\text{UO}_4\text{-Na}_2\text{U}_2\text{O}_7$) where both sodium and oxygen could be measured. With the measured sodium and oxygen pressures and the calculated equilibrium constants, one can calculate oxygen pressures by a stepwise process in each of the three-phase regions where sodium pressures were measured. Finally, the data will be used to calculate oxygen pressures in the $\text{UO}_2\text{-Na}_3\text{UO}_4\text{-Na}$ three-phase region.

After completing studies on the U-O-Na system, we plan to study the U-Pu-O-Na system.

4. Influence of Oxygen Contamination on Carbon and Uranium Activities in UC

Measurements of the influence of oxygen on carbon activity and total pressure of uranium-bearing species in the uranium-carbon system have been initiated. To avoid the formation of $\text{UO}_2(\text{s})$ when investigating the single-phase UC_xO_y region, the oxygen partial pressure must be lower than that needed for the formation of $\text{UO}_2(\text{s})$. Therefore very high CO/CO_2 ratios are required (since $2\text{CO}_2 \rightleftharpoons 2\text{CO} + \text{O}_2$). With a gettering system consisting of a combination of hot copper and a Molecular Sieve, we were able to obtain a CO-He carrier-gas mixture containing less than 0.1 ppm CO_2 . The CO/CO_2 ratios in the equilibrating gas were measured by means of gas chromatography. From these ratios, estimates of the carbon and oxygen activities can be obtained.

The uranium carbide charge used in our studies consisted of a spherical -8 +12 mesh powder with the following composition: ~4.55 wt % carbon ($\text{C}/\text{U} = 0.96$), ~150 ppm oxygen, ~350 ppm nitrogen, and <200 ppm metallic impurities. In the early runs carried out at relatively low carrier-gas flow rates, the CO/CO_2 ratio of the exiting gas was approximately an order of magnitude lower than that of the input gas. Recent experiments at high carrier-gas flow rates have minimized the discrepancy between input and output CO/CO_2 ratios. The results at 2355°K are summarized in Table III-1. It should be noted that metallographic examination of the residues did not show the presence of $\text{UO}_2(\text{s})$ in the matrix or on the surface of the particles in any of the experiments.

From these data, we calculate carbon activities to be approximately 1.5×10^{-3} at 2355°K. For comparison, the carbon-activity values based on our measurements with the $\text{H}_2\text{-CH}_4$ mixtures over "oxygen-free" UC_x compositions ranging from $\text{C}/\text{U} = 0.99$ to $\text{C}/\text{U} = 1.00$ yielded values of a_{C} of ~0.15 at 2355°K. The effect of a small addition of oxygen, e.g., 1.5-2.0 at. %, results in a significant reduction in the activity of carbon. This can have important implications in the potential transfer of carbon from fuel to cladding materials.

TABLE III-1. Tentative Values of Carbon Activity and Oxygen Partial Pressure for U-C-O System

	Run 100-1	Run 101-1	Run 101-2
Temperature, °K	2355	2355	2355
Time of run, hr	5.5	2.9	6.7
Carrier gas	CO-He	CO-He	CO-He
Flow rate, ml/min	1100	1100	1100
Partial pressure CO in carrier gas, Torr	~10	~4	~4
CO/CO ₂ , input gas	3.2×10^4	5.4×10^4	5.7×10^4
CO/CO ₂ , output gas	2.2×10^4	4.6×10^4	4.7×10^4
-log p(O ₂) (based on input)	12.52	12.98	12.94
-log p(O ₂) (based on output)	12.20	12.72	12.78
Carbon activity (based on input)	2.0×10^{-3}	1.3×10^{-3}	1.4×10^{-3}
Carbon activity (based on output)	1.4×10^{-3}	1.0×10^{-3}	1.1×10^{-3}
Composition	UC _{1.00} O _{0.04}	UC _{1.00} O _{0.02}	UC _{1.00} O _{0.02}
Nitrogen content, ppm	710	-	-
Metallographic examination	UO ₂ not detected	UO ₂ not detected	UO ₂ not detected

The total pressure of uranium-bearing species was measured at 2020, 2155, 2255, and 2355°K. The total pressure of uranium-bearing species over uranium oxycarbide composition is considerably higher (a factor of 10 or more) than the pressures obtained with "oxygen-free" material. This higher pressure may reflect in part the enhancement in uranium activity as a consequence of the significant reduction of carbon activity in the oxycarbide, as well as the vaporization of an oxygen-containing uranium species from the oxycarbide composition.

For the oxycarbide compositions given in Table III-1, the free energy of formation was roughly estimated from oxygen and carbon activity values derived from our measurements. In the absence of species information, the uranium activity was based on the total pressure of uranium-bearing species, the assumption that the vapor is uranium gas, and the sublimation pressure of pure uranium. From the expression $\Delta G_f^\circ = R'T \log N_i \Sigma a_i$, a tentative value of -40 kcal/mol at 2355°K was obtained for the free energy of formation. The free energy of formation of "oxygen-free" UC calculated from our carbon-activity measurements and Storms' adjusted vapor pressure measurements was $\Delta G_f^\circ \approx -24.8$ kcal/mol at 2355°K.

B. Reactor Safety and Physical Property Studies

The primary objective of these studies is to provide physical property data for use in evaluating the safety of various fast-breeder reactor materials. Property data obtained experimentally at temperatures above

normal operating conditions will be extrapolated to the much higher temperatures involved in accident situations. In addition, reactor material-fuel phase studies at high temperatures are under way to provide chemical information needed on fission-product distribution between molten fuel and other reactor materials for use in post-accident heat-removal calculations.

1. Enthalpies and Heat Capacities by Drop Calorimetry

Three complementary calorimetric systems for the measurement of high-temperature enthalpy increments are available for our use. Depending on the material to be studied and temperature range to be covered, one may choose (1) the resistance-heated drop calorimetric system¹ (600-1600°K), (2) the electron-beam-heated drop calorimetric system² (1300-2500°K), or (3) the induction-heated drop calorimetric system³ (2500-3600°K). During this report period, systems (1) and (3) have been used for making measurements.

a. Resistance-Heated Calorimetric System

Thermodynamic data are needed on fission-product oxides for help in evaluation of the oxidizing potential in reactor fuel pins. With this in mind, a survey of the literature was conducted on 22 fission-product elements that form various oxides. No high-temperature enthalpy data were found for ruthenium dioxide; high-temperature enthalpy measurements have since been completed by us on this compound. Other fission-product oxides, for which data are not available, will be studied later.

The experimental data for $\text{RuO}_{1.98}$ over the temperature range 298-1200°K can be represented by the expression

$$(\text{H}_T^\circ - \text{H}_{298.15}^\circ) = 18.2472T + 1.31489 \times 10^{-3}T^2 + 5.77166 \times 10^5T^{-1} - 7493.1 \text{ cal/mol} \quad (1)$$

The standard deviation for Eq. 1 is 34 cal/mol or 0.27%. The constraint that $(\text{H}_T - \text{H}_{298}) = 0$ at 298.15°K has been used in fitting the data.

The heat capacity for $\text{RuO}_{1.98}$ is obtained from the derivative of Eq. 1 and is given by

$$C_p^\circ = 18.2472 + 2.62978 \times 10^{-3}T - 5.77166 \times 10^5T^{-2} \text{ cal/(mol)(°K)} \quad (2)$$

¹D. R. Fredrickson, R. D. Barnes, M. G. Chasanov, R. L. Nuttall, R. Kleb, W. N. Hubbard, High Temp. Sci. **1**, 373 (1969).

²D. R. Fredrickson, R. Kleb, R. L. Nuttall, W. N. Hubbard, Rev. Sci. Instr. **40**, 1022 (1969).

³L. Leibowitz, M. G. Chasanov, L. W. Mishler, Trans. Met. Soc. AIME **245**, 981 (1969).

b. Induction-Heated Drop Calorimeter System

Work is continuing on the program to determine the heat capacity of UO_2 and of $(\text{U,Pu})\text{O}_2$ to high temperatures. Accurate values for heat capacity and heat of fusion will facilitate estimation of the total energy released and the temperatures attained in a reactor core during hypothetical destructive nuclear excursions. Induction heating is being used in conjunction with normal drop calorimetry procedures. The experimental procedure has been described previously.⁴

We have now completed work on UO_2 . Our enthalpy data for liquid UO_2 , for the range from 3173 to 3523°K, can be represented by the following equation obtained by the method of least squares

$$H_T^\circ - H_{298}^\circ = 32.457T - 11153.4 \quad (3)$$

The enthalpy is given in calories per mole and temperature, T , is in degrees Kelvin. The estimate of the standard error for Eq. 3 is 544 cal/mol. Moderate extrapolations using this linear relation should be satisfactory.

The heat of fusion of uranium dioxide found from our studies is 17.7 kcal/mol, and is in good agreement with the value of 18.2 kcal/mol reported by Hein and Flagella.⁵

To date, considerable effort has gone into preparation for measurements of the enthalpy of mixed-oxide fuel materials. A walk-in hood has been constructed around the induction-heated drop calorimeter system, which has been modified for operation from outside the hood. Once a sample capsule has been loaded into the furnace, the entire enthalpy determination can be performed without entering the hood. $(\text{U}_{0.8}\text{Pu}_{0.2})\text{O}_2$ pellets have been fabricated, as have suitable tungsten containers. Preparations are being made for loading and welding shut these capsules, following which enthalpy measurements will begin.

2. Vapor Pressure over UO_2 at High Temperatures

Fuel vapor pressure is an important input parameter for equation-of-state calculations in fast-reactor safety analyses. The experimental data presently available must be extrapolated over many orders of magnitude to obtain vapor-pressure values at the temperatures of interest. We are carrying out studies to provide experimental vapor pressure data over molten uranium oxide, thus providing a better basis for extrapolation. The data are being obtained by use of a transpiration apparatus described in ANL-7675, p. 90.

⁴L. Leibowitz, L. W. Mishler, D. F. Fischer, "Chemical Engineering Division Annual Report, 1969," ANL-7675, p. 89 (1970).

⁵R. A. Hein, P. N. Flagella, "Enthalpy Measurements of UO_2 and Tungsten to 3260°K," GEMP-578 (1968).

Much of the initial experimentation has involved measurements to evaluate such factors as inert carrier-gas flow rates, choice of operating techniques, hot-zone geometry, and the effect of vaporization on sample stoichiometry. These studies have utilized uranium oxide microspheres with an initial O/U ratio of 2.00. The carrier gas employed has been argon (99.999%). O/U ratios are determined by ignition of the solid to U_3O_8 ; uranium content of the condensate from the experiments is evaluated colorimetrically. The results of these initial studies are presented in Table III-2. The data in the table include the highest temperature-pressure measurements yet reported for uranium oxide.

TABLE III-2. Total Pressure of Uranium-Bearing Species over UO_2^a

Temperature (°K)	Initial O/U	Total Pressure (atm)	Condensed Phase
2615	2.00	4.45×10^{-4}	solid
2860	2.00	6.55×10^{-3}	solid
3175	2.00	7.1×10^{-2}	liquid
3390	2.00	0.18	liquid
3390	1.94	0.15	liquid

^aArgon was used as carrier gas.

It was found that there was some reduction in the O/U ratio of the transpiration sample remaining after each experiment. This was more pronounced at the higher temperatures. However, it is not yet clear whether this variation has a significant effect on the total pressure. This phenomenon will be studied later using a buffered carrier gas (probably $\text{H}_2\text{O}-\text{H}_2$ mixtures).

The data obtained for solid UO_2 (presented in Table III-2) are in excellent agreement with the literature data, e.g., those of Tetenbaum and Hunt.⁶ There are no other pressure data over the liquid available for comparison. However, one can make an extrapolation for the liquid based on the data of Tetenbaum and Hunt for the solid, recent data for the heat of fusion of UO_2 (see Section III.B.1.b of this report), and the assumption of a linear pressure vs. $1/T$ relationship. Figure III-3 shows the extrapolated liquid pressure plot, Tetenbaum and Hunt's pressures for the solid, and our experimental data. The agreement is quite good.

⁶M. Tetenbaum, P. D. Hunt, *J. Nucl. Mater.* 34, 86 (1970).

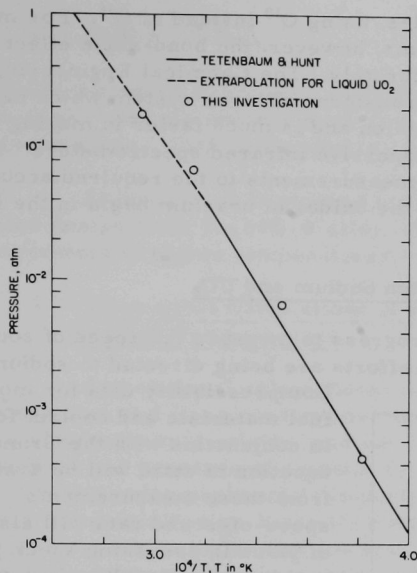


Fig. III-3

Total Pressure of Uranium-Bearing Species over Near-Stoichiometric Uranium Oxide as Function of Temperature. ANL Neg. No. 308-2419.

3. Matrix Isolation Spectroscopy of UO_2

The thermodynamic properties of the vapor species of fuel oxides are important in determining equation-of-state relationships used in projecting the results of certain fast-breeder reactor design-basis accidents. Application of statistical mechanical techniques to spectroscopic data for these species is a useful way of determining their thermodynamic properties at temperatures beyond the range of direct experimental measurements. The matrix isolation method, by trapping molecules in frozen inert gas lattices, allows low-temperature pseudo-gas-phase studies to be carried out on molecules normally present in large gas-phase concentrations only at very high temperatures. Because the population of excited rotational quantum levels is eliminated under these low-temperature conditions, interpretation of the simplified infrared and visible spectra is greatly facilitated.

During the past year, construction and testing of the experimental apparatus have been completed. A solid fuel sample of specific O/M ratio is heated in the apparatus by passing current through a small Knudsen cell. The molecular beam thus produced, together with a stream of inert gas, impinges on an infrared-transmitting window in a variable-temperature, liquid-helium cryostat. This provides the matrix for study.

One of the important parameters in determining the thermodynamic properties of gaseous UO_2 is the O-U-O bond angle. It can be determined in principle by comparison of the asymmetric stretching frequencies

of isotopically substituted molecules, using O^{18} instead of O^{16} . For molecules containing heavy central atoms, however, the bond-angle effect is small and difficult to measure accurately. The Chemical Engineering Division has available a Fourier transform infrared system which has much greater sensitivity and precision and is much faster in making measurements than are conventional dispersive infrared spectrometers. Its use will greatly facilitate performing measurements to the required accuracy when the spectroscopic studies of the oxides of uranium begin in the immediate future.

4. Speed of Sound in Molten Sodium and UO_2

Experiments are in progress to measure the speed of sound in molten reactor materials. Initial efforts are being directed to sodium.

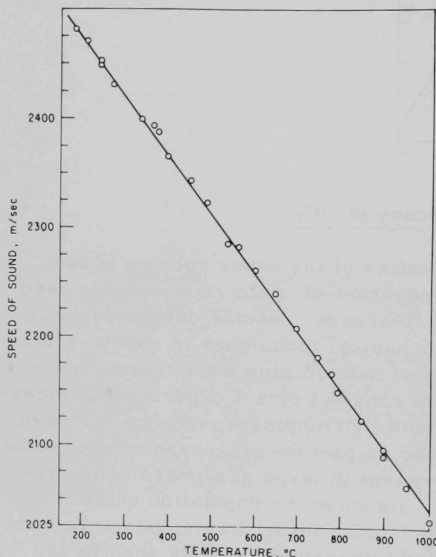


Fig. III-4. Speed of Sound in Liquid Sodium as Function of Temperature. ANL Neg. No. 308-2326.

Compressibility data for molten fuel materials and coolant for use in conjunction with the Gruneisen equation of state will be available from these measurements. These speed-of-sound data will also be of value in assessing shock propagation through molten fuel and coolant, as well as in analyzing two-phase flow of coolant.

Measurements of the speed of sound in sodium were made from 182 to 1001°C by the pulse-echo technique. The data are presented in Fig. III-4. Multiple echoes were readily detectable in these experiments, and each datum point given represents the average of two to four echoes which gave closely agreeing values. The data can be represented by the equation

$$V = 2577.3 - 0.53607t \quad (4)$$

where the velocity, V , is in meters/sec and the temperature, t , is in degrees centigrade. Moderate extrapolations to temperatures above 1000°C should be reasonably satisfactory. The estimate of the standard deviation for this equation is 3.92 meters/sec. Equation 4 may be compared with that given by Trelin et al.⁷

⁷Yu. S. Trelin, I. N. Vasil'ev, V. B. Proskurin, T. A. Tsyganova, *Teplofizika Vysokikh Temperatur* 4, 364 (1966); English translation: *High Temp.* 4, 352 (1966). Data previously reported by Trelin [Yu. S. Trelin, I. N. Vasil'ev, V. V. Roshchupkin, *Atomnaya Energiya* 9, 410 (1960); English translation: *Soviet Atomic Energy* 9, 955 (1960)] are in error by 2-2.5%.

$$V = 2585.6 - 0.542t \quad (5)$$

Values for the speed of sound in sodium at 250°C given by Pochapsky,⁸ Trelin et al.,⁷ and the present work are, respectively, 2446, 2450, and 2443 meters/sec. This agreement is considered satisfactory.

At present, it is planned to fabricate a new cell of slightly modified design from Ta-10% W alloy, which will allow extension of these measurements to higher temperatures (~1500°C).

5. Theoretical Calculations of Measured Physical Property Data to High Temperatures

A variational calculational method, based on thermodynamic considerations and mass constraints, has been used to determine the effects of burnup, void volume, and fuel starting composition on the phase composition and pressure of an oxide fuel-fission product system at 3500°K. The predicted vapor pressure is important in contributing to the understanding of certain design-basis accidents; knowledge of the phase composition of the system is necessary for post-accident heat-removal analyses. The initial assumptions used in these computations included temperature uniformity, immiscibility of fission product and fuel condensed phases, and free access of vapor species to void and plenum regions.

Programming modifications have recently been completed to account for the fact that fission-product oxides will be present in the fuel lattice rather than as separate phases. Similarly, the possibility of alloy formation between metallic fission-product species has been introduced. Ideal solution theory has been assumed. The decreased activities of the condensed fission-product species are expected to alter the calculated qualities significantly. In the future, attempts will also be made to consider the effects of coolant and cladding materials for the complete meltdown design-basis accident.

6. Thermal Diffusivity of Reactor Materials

Values of the thermal diffusivity of UO₂ in the liquid state are of importance to the reactor safety program. This information is needed to evaluate means of safely cooling the core of an LMFBR in the event of a meltdown incident. Reliable experimental values of thermal diffusivity and thermal conductivity are available for solid UO₂ up to about 2300°K. There has been speculation that the thermal conductivity of UO₂ will increase above 2300°K and that a contributing factor to such an increase would be increased electronic conductivity. There is also considerable uncertainty about radiative heat transfer in UO₂. It is hoped that the present research will resolve these uncertainties.

⁸T. E. Pochapsky, Phys. Rev. **84**, 553 (1951).

We have selected a method of determining thermal diffusivity which was first proposed by Cowan.⁹ In this method, thermal diffusivity is determined from the phase change in a thermal wave passing through a sample. This wave is produced by heating the sample with a sinusoidally modulated electron beam. Several experimental variations using this approach have been developed and applied to metals up to 3200°K and to oxides up to 2000°K.¹⁰

We plan to obtain thermal-diffusivity data for liquid UO_2 between its melting point and about 3500°K and for solid UO_2 from 2300°K to the melting point. Because tungsten will be used as the container material, values of thermal diffusivity will be obtained for tungsten and checked against the literature values in the range of 2800°K to 3200°K, and additional values will be sought up to 3500°K.

These experiments will be performed in a dual-gun electron beam furnace, formerly used as a high-temperature tensile-test furnace. Extensive electronic modifications to the system, needed for these diffusivity measurements, are currently being made. Cell design and temperature and phase-shift measuring procedures are also currently under test.

7. Reactor Materials--Fuel Phase Studies at High Temperatures

Knowledge of the distribution of fission products to the phases produced in the event of a meltdown of the core of an LMFBR is required to predict the fission-product heat distribution after an incident and to assure that means are available for cooling the products of the meltdown.

One phase of our experimental program is to determine the distribution of fission-product elements between molten UO_2 and molten stainless steel. The fission products to be studied (Nb, La, Mo, Zr, and Ru) are among those that contribute to the major portion of the heat produced soon after shutdown of a fast reactor and that have properties suitable for the experimental method used.

We have performed experiments in an arc-melting furnace to determine how zirconium distributes between liquid phases of UO_2 and iron. Metallographic examination of cross sections of the resultant uranium oxide-iron buttons indicated that there was a clean separation of the oxide and metal phases. Chemical and electron microprobe analyses indicate that the zirconium would be distributed to the oxide phase in the event of a core meltdown incident--as one would predict thermodynamically.

⁹R. D. Cowan, "Proposed Method of Measuring Thermal Diffusivity at High Temperatures," LA-2460, Los Alamos Scientific Laboratory (1960); also, *J. Appl. Phys.* **32**, 1363 (1961).

¹⁰J. B. Ainscough, M. J. Wheeler, *Brit. J. Appl. Phys., Ser. 2*, **1**, 859 (1968); O. A. Kraev, A. A. Stel'makh, *High Temp.* **1**, 5 (1963); M. Serizawa *et al.*, *Proc. of Eighth Conf. on Thermal Conductivity (1968)*, p. 549, Plenum Press, N. Y. (1969); M. J. Wheeler, *Brit. J. Appl. Phys.* **16**, 365 (1965).

The distribution of fission-product (F.P.) elements between liquid UO_2 -concrete and molten steel is under study because of the possible interaction of molten fuel components with the concrete which will lie below the core of a reactor such as FFTF. Molten UO_2 coming into contact with the concrete will cause it to melt. The liquidus point of a typical concrete mixture to be used in FFTF construction will be about 1400°C . Dissolution of SiO_2 , CaO , and Al_2O_3 can further lower the liquidus to about 1100°C . At some point, the density of the magma will become less than that of the molten steel--then the liquid phase of UO_2 -Pu O_2 -F.P. and concrete constituents will rise to the surface and the molten steel will sink to the bottom. A knowledge of the distribution of fission products between the steel and UO_2 -concrete phases becomes important if one is to be able to estimate the heat distribution to the phases.

An effort was made to find a container material for this oxide-metal mixture. Experiments with a tantalum carbide crucible in the arc-melting furnace for a short duration showed little reaction with iron. A preliminary experiment with the concrete- UO_2 -iron mixture plus some inactive fission-product oxides, contained in a zircon crucible welded into a tantalum capsule, has been performed in a resistance-heated furnace, and it appears that this method of investigation may be satisfactory.

C. Calorimetry

The calorimetric program is directed toward the experimental, empirical, or theoretical determination of thermodynamic properties of substances that are of interest in high-temperature chemistry and nuclear technology. Measurements are being made of standard enthalpies of formation (ΔH_{298}°) of the substances. Complementary experimental determinations of high-temperature increments ($\Delta H_T^\circ - \Delta H_{298}^\circ$) are reported elsewhere in this report. Complementary low-temperature thermal measurements of C_p° , ΔH_{tr}° , and S° are being performed in the Chemistry Division and elsewhere.

The method of fluorine bomb calorimetry was developed for measurements on substances not amenable to more conventional calorimetric techniques and has now been used to determine the enthalpies of formation of 35 elemental fluorides and 21 other compounds. The more conventional oxygen bomb calorimetry has been used for studies of fifteen reactions and solution calorimetry for measurements of nine aqueous reactions.

Attempts at the determination of thermodynamic properties by empirical calculations (e.g., the correlation and estimation of enthalpies of formation for the rare earth trifluorides: ANL-7450, p. 64) and by theoretical calculations (e.g., extended Hückel molecular-orbital calculations for the chalcogen hexafluorides: ANL-7450, p. 66) now include ab initio calculations based on the Hartree-Fock-Roothaan approach for the binary fluorides of the chalcogens (OF, SF, and SeF) and the pnictogens (NF and PF) and their ions.

1. Thermochemistry of Plutonium Compounds: Enthalpy of Formation of Plutonium Sesquicarbide

As part of the continuing program to provide accurate thermochemical data for plutonium compounds, the standard enthalpy of formation of plutonium sesquicarbide was determined by oxygen bomb calorimetry. The elucidation of the basic thermodynamic properties of plutonium carbides is important because of the interest in them as fast-breeder-reactor fuels.

The sample of plutonium sesquicarbide used was prepared by J. A. Leary (Los Alamos Scientific Laboratory) by arc melting an appropriate mixture of plutonium and graphite. The combustion technique used was similar to that described previously for plutonium monocarbide,¹ except that several grams of plutonium metal were added to the sample in each experiment to serve as a combustion aid. Even with the addition of the plutonium metal, the combustions were not entirely complete, and it was necessary to make an empirical correction for the carbon residue. Based on four combustions, the energy of combustion of plutonium sesquicarbide was determined to be $-1442.1 \pm 0.7 \text{ cal g}^{-1}$. This result was used to derive a preliminary value for the standard enthalpy of formation of plutonium sesquicarbide, $\Delta H_{298}^{\circ}(\text{PuC}_{1.466}, \text{c})$, of $-19.4 \pm 0.7 \text{ kcal mol}^{-1}$.

2. Thermochemistry of Hydrogen Fluoride

The thermochemistry of hydrogen fluoride in its various states (gas, liquid, aqueous solution) is of fundamental interest, not only because HF is a common and useful chemical in its own right, but because it is involved, either as reactant or product, in a large number of thermochemical investigations. Therefore, to minimize the errors in the results obtained from calorimetric studies involving HF, it is imperative to know $\Delta H_f^{\circ}(\text{HF})$ as accurately as possible. The presently accepted values² for the enthalpies of formation of $\text{HF}(\ell)$ and $\text{HF}(\text{aq})$ are obtained from $\Delta H_f^{\circ}(\text{HF}, \text{g})$ by using the enthalpies of vaporization of $\text{HF}(\ell)$ and the enthalpy of solution of $\text{HF}(\text{g})$, respectively. Thus, the thermodynamic properties of all the states are dependent on $\text{HF}(\text{g})$. This is unfortunate as $\text{HF}(\text{g})$ is a highly associated gas and the corrections to standard states are both large and uncertain.

To elucidate the thermochemistry of aqueous HF by a route which eliminates the uncertainties associated with HF gas, we measured (1) the enthalpy of formation of liquid HF directly from gaseous hydrogen and fluorine, (2) enthalpies of solution of liquid HF in water to form aqueous HF of various concentrations from $\text{HF} \cdot 2\text{H}_2\text{O}$ to $\text{HF} \cdot 5500\text{H}_2\text{O}$, and (3) the

¹G. K. Johnson, E. H. Van Deventer, O. L. Kruger, W. N. Hubbard, *J. Chem. Thermodyn.* **2**, 617 (1970).

²D. D. Wagman, W. H. Evans, V. B. Parker, I. Halow, S. M. Bailey, R. H. Schumm, NBS Technical Note 270-3 (1968).

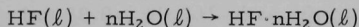
enthalpy of neutralization of liquid HF by dilute aqueous NaOH, from which may be derived the enthalpy of formation of HF at infinite dilution and the enthalpy of formation of the fluoride ion.

a. Enthalpy of Formation of Liquid Hydrogen Fluoride

The enthalpy of formation of liquid hydrogen fluoride was determined by measuring the energy released by the reaction of fluorine with hydrogen in a two-compartment calorimetric combustion bomb.³ The combustion compartment of the nickel bomb was gold-plated to protect it from corrosion by HF. However, the gold plating was slightly reactive with fluorine, and an empirical correction for the thermal effect of the reaction had to be made. Empirical corrections were also made for the vaporization of the liquid HF to saturate the bomb and for the energy of mixing of gaseous HF and F₂. From these measurements, the standard enthalpy of formation of liquid HF, $\Delta H_{f,298}^{\circ}(\text{HF}, \ell)$, was calculated to be $-72.57 \pm 0.09 \text{ kcal mol}^{-1}$, which is $0.9 \text{ kcal mol}^{-1}$ more negative than the previously accepted value of $-71.65 \text{ kcal mol}^{-1}$.³ This datum supersedes the preliminary datum presented earlier.⁴

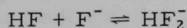
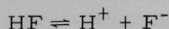
b. The Enthalpy of Solution and Neutralization of Liquid Hydrogen Fluoride

The determination of the enthalpy of solution of liquid HF in water according to the reaction



was discussed previously.⁴ The data presented at that time have since been found to be in error due to a small leakage of HF vapor through the windows (3-mil Kel-F film) of the ampoules used to contain the HF(ℓ). This work has been repeated with 5-mil Kel-F windows, which are impervious to HF at room temperature.

Previously⁴ an attempt was made to extend the enthalpy of solution measurements to infinite dilution based on equilibrium constants and enthalpies for the equilibria



present in aqueous solutions of hydrogen fluoride. A better method to obtain the standard enthalpy of solution is through measurements of the enthalpy of

³J. L. Settle, E. Greenberg, W. N. Hubbard, Rev. Sci. Instr., **38**, 1805 (1967).

⁴ANL-7650, pp. 29 and 34 (1969).

neutralization of $\text{HF}(\ell)$. Six measurements of the enthalpy of neutralization of $\text{HF}(\ell)$ in 0.1N NaOH yielded an average value and standard deviation for $\Delta H_{\text{neut.}}$ of $-21,036 \pm 5 \text{ cal mol}^{-1}$. This result, when combined with the enthalpy of ionization of water, $13,345 \pm 25 \text{ cal mol}^{-1}$, yields the standard enthalpy of solution at 298°K, $\Delta H_{\text{soln}}^{\circ}(\text{HF}, \ell) = -7961 \pm 30 \text{ cal mol}^{-1}$.

Other quantities which are derivable from the work include the standard enthalpy of formation of the fluoride ion, $\Delta H_f^{\circ}(\text{F}^-, \text{aq}) = -80.35 \pm 0.09 \text{ kcal mol}^{-1}$, which is equal to $\Delta H_f^{\circ}(\text{HF} \cdot \infty \text{H}_2\text{O})$ using the usual convention in that $\Delta H_f^{\circ}(\text{H}^+ \cdot \infty \text{H}_2) = 0$, and the enthalpy of formation of $\text{NaF}(\text{c})$ of $-137.95 \pm 0.10 \text{ kcal mol}^{-1}$. The latter quantity is obtained from the neutralization data using values of $\Delta H_f^{\circ}(\text{NaOH}, \text{aq}) = -112.439 \pm 0.015 \text{ kcal mol}^{-1}$ (Ref. 5) and $\Delta H_{\text{soln}}^{\circ}(\text{NaF}, \text{c}) = 218 \pm 10 \text{ cal mol}^{-1}$ (Ref. 6).

3. Enthalpies of Formation of Disodium and Monosodium Acetylides

The thermodynamic and chemical properties of disodium acetylide, Na_2C_2 , are currently of considerable interest because this material is thought to have a role in the transport of carbon in liquid-sodium reactor coolants. Therefore, an investigation was undertaken to determine the standard enthalpy of formation, $\Delta H_f^{\circ}_{298}(\text{Na}_2\text{C}_2, \text{c})$, from measurements of the enthalpy of reaction of Na_2C_2 with water. The enthalpy of formation of monosodium acetylide, NaHC_2 , was also determined by the same technique because its chemistry is closely related to that of Na_2C_2 .

The enthalpies of reaction of the Na_2C_2 and NaHC_2 samples with water were determined to be -548.45 ± 1.09 and $-269.03 \pm 0.95 \text{ cal g}^{-1}$, respectively. From these results, the standard enthalpies of formation, $4.77 \pm 0.40 \text{ kcal mol}^{-1}$ and $23.10 \pm 0.27 \text{ kcal mol}^{-1}$, were calculated for Na_2C_2 and NaHC_2 , respectively.

The enthalpy of formation of Na_2C_2 at 25°C, in itself, does not predict the stability of Na_2C_2 at reactor temperatures; however, estimates of the entropy, $S_T^{\circ}(\text{Na}_2\text{C}_2)$, and enthalpy functions, $(H_T - H_{298}^{\circ})$, would indicate that the free energy of formation from either solid or liquid sodium, ΔG_f , is positive for all temperatures above 25°C, and thus the substance is thermodynamically unstable relative to free sodium and graphite. Until experimental measurements of the entropy and enthalpy functions become available, the estimates on which these conclusions are based must be viewed as highly uncertain. It is also likely that the formation of Na_2C_2 would be enhanced by amorphous carbon in a highly active state, which is probably the case in a reactor.

⁵S. R. Gunn, J. Phys. Chem. 71, 1386 (1967).

⁶V. B. Parker, "Thermal Properties of Aqueous Uni-univalent Electrolytes," NSRDS-NBS 2 (April, 1965).

4. The Thermochemistry of Na_3UO_4 and Na_2O

It has been demonstrated that Na_3UO_4 is the compound likely to be in equilibrium with sodium and uranium dioxide in the presence of excess oxygen (see Section III.A.2). Because there apparently exist no thermodynamic data for this compound, and because of its relation to sodium-cooled oxide fuel reactors, the determination of the enthalpy of formation of Na_3UO_4 has been added to the program of the group. Preliminary measurements by solution calorimetry are under way, and a calorimetric-grade sample is being prepared by the High Temperature Materials Group.

Because the enthalpy of formation of Na_2O is a necessary auxiliary datum for the study of Na_3UO_4 and the literature values are discordant, the determination of the enthalpy of formation of Na_2O has also been placed on the program.

5. Enthalpy of Formation of Molybdenum Disulfide

The calorimetric investigation of MoS_2 , described briefly earlier,⁴ has been concluded. A paper describing the work, titled "A Fluorine Bomb Calorimetric Study of Molybdenum Disulfide. The Standard Enthalpies of Formation of the Di- and Sesquicarbides of Molybdenum," has been published.⁷ The abstract of the paper is as follows:

The energy of the reaction between fluorine and a well-characterized sample of natural molybdenite (MoS_2) to give gaseous MoF_6 and SF_6 , was measured in a fluorine bomb calorimeter. The corresponding standard enthalpy of formation at 298.15 K, $\Delta H_f^\circ(\text{MoS}_2, \text{c}, 298.15 \text{ K})$, is $-(65.8 \pm 1.2) \text{ kcal mol}^{-1}$, in reasonable agreement with several modern high-temperature studies. A survey of thermochemical data in the literature leads to a consensus value of $-(97 \pm 3) \text{ kcal mol}^{-1}$ for $\Delta H_f^\circ(\text{Mo}_2\text{S}_3, \text{c}, 298.15 \text{ K})$.

6. Enthalpy of Formation of Xenon Hexafluoride

An investigation to determine the enthalpy of formation of xenon hexafluoride has been undertaken. Values found in the literature for the energy of the Xe-F bond in XeF_6 , based on calorimetric^{8,9} and equilibrium¹⁰ results, are discordant, varying between -70.4^{10} and $-126^9 \text{ kcal mol}^{-1}$, depending on the auxiliary data used.

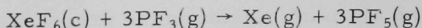
⁷P. A. G. O'Hare, E. Benn, F. Y. Cheng, G. Kuzmycz, *J. Chem. Thermodyn.* **2**, 797-804 (1970).

⁸L. Stein, P. Pluriem, *Noble-Gas Compounds*, p. 144, The Univ. of Chicago Press (1963).

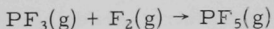
⁹C. C. Selph, thesis, Georgia Inst. of Tech. (1970).

¹⁰B. Weinstock, E. E. Weaver, C. P. Knop, *Inorg. Chem.* **5**, 2189 (1966).

A sample of XeF_6 has been prepared¹¹ and will be reacted with $\text{PF}_3(\text{g})$ according to



This reaction proceeds spontaneously and will necessitate the use of a two-chambered reaction vessel. The necessary auxiliary data for the reaction



have already been determined¹² in this laboratory.

7. Quantum Chemical Investigations of Selected Nonmetal Monofluorides

As part of a continuing effort to (a) rationalize previously observed^{13,14} bond energy trends and (b) establish a scheme to predict reliable thermodynamic data for fluorine-containing molecules, free radicals, and ions, we have been involved for a considerable part of the present year in the calculation of accurate wave functions for gaseous diatomic fluoride molecules and ions. Although this study is far from complete, a substantial amount of useful and informative data has been obtained.

a. The Chalcogen-Fluorine Systems

The results have been described for the oxygen-fluorine system¹⁵ and the sulfur- and selenium-fluorine systems^{16,17} in recent publications. The properties reported in these papers are summarized in Table III-3.

b. The Pnictogen-Fluorine System

Wave functions were computed for the three low-lying states, viz., the $^3\Sigma$ ground state and the excited $^1\Sigma$ and $^1\Delta$ states of NF . Among the hitherto unreported data obtained in this part of the investigation are the electron affinity of $\text{NF}(^3\Sigma)$ and the dipole and quadrupole moments of the three low-lying states. The total Hartree-Fock energy for $\text{NF}(^3\Sigma)$ is approximately 13 eV more stable than that obtained in a previous molecular

¹¹ By J. G. Malm of the Chemistry Division, ANL.

¹² E. Rudzitis, E. H. Van Deventer, W. N. Hubbard, *J. Chem. Thermodyn.* **2**, 221 (1970).

¹³ P. A. G. O'Hare, W. N. Hubbard, H. M. Feder, IUPAC Thermodynamik Symposium, Heidelberg, Germany, Sept. 1967, paper No. II-5.

¹⁴ P. A. G. O'Hare, H. M. Feder, Amer. Chem. Soc., 152nd National Meeting, New York, N. Y., Sept. 1966. Abstracts of papers No. V-163.

¹⁵ P. A. G. O'Hare, A. C. Wahl, *J. Chem. Phys.* **53**, 2469 (1970).

¹⁶ P. A. G. O'Hare, A. C. Wahl, *J. Chem. Phys.* **53**, 2834 (1970).

¹⁷ P. A. G. O'Hare, A. C. Wahl in Proceedings of the 3rd European Symposium on Fluorine Chemistry, Aix-en-Provence, France, Sept. 1970.

orbital study described by Sahni.¹⁸ Derived dissociation energy and ionization potential values are in excellent agreement with results from experimental studies.¹⁹⁻²¹ Based on thermochemical arguments, the NF^- ion is predicted to be only marginally stable at room temperature. In harmony with the latter observation, the NF^- ion has never been detected experimentally. The various properties deduced for NF are summarized in Table III-3.

TABLE III-3. Computed Properties of Diatomic Fluorides

Molecule	D_0^0 (eV)	I (eV)	E_a (eV)	$\mu(\text{D})^a$	$Q(\times 10^{-26}$ $\text{esu cm}^2)^a$
$\text{OF}(^2\Pi)$	$3.0^{+0.3}_{-0.8}$	13.1 ± 0.5	1.4 ± 0.5	-0.36	0.13
$\text{SF}(^2\Pi)$	4.2 ± 0.2	10.0 ± 0.4	2.5 ± 0.5	-1.40	0.57
$\text{SeF}(^2\Pi)$	4.0 ± 0.2	9.5 ± 0.4	$\leq 2.8 \pm 0.5$	-2.21	-1.04
$\text{NF}(^3\Sigma^-)$	3.4 ± 0.2	13.2 ± 0.3	0.6 ± 0.3	-0.41	-0.75
$\text{NF}(^1\Sigma^+)$	3.5 ± 0.5^b			0.08	-0.62
$\text{NF}(^1\Delta)$	1.8 ± 0.5^c			-0.17	-0.68
$\text{PF}(^3\Sigma^-)$	4.5 ± 0.3	9.7 ± 0.2^d	1.4 ± 0.3	-1.17	-0.90

^aValues of μ and Q have also been computed for the positive and negative ion of each molecule.

^bExcitation energy for the process $\text{NF}(^3\Sigma^-) \rightarrow \text{NF}(^1\Sigma^+)$.

^cExcitation energy for the process $\text{NF}(^3\Sigma^-) \rightarrow \text{NF}(^1\Delta)$.

^dAdiabatic ionization potential is 9.5 ± 0.2 eV.

Among the more interesting aspects of the investigation of the phosphorus-fluorine system¹⁷ was the calculation of both the vertical and adiabatic ionization potentials, $I(\text{PF})$. The adiabatic ion, as one would anticipate, was found to be about 0.25 eV more stable than the vertical ion. Rather unexpectedly, however, the vertical ionization potential came out to be almost 4 eV lower than the value implicit in Wada's²² mass spectrometric appearance potential measurements. Wada's data yield an ionization potential almost 100% larger than that for the adjacent SiF and SF and imply, inter alia, that removal of an antibonding electron from PF results in a weakening of the bond. Our calculated ionization potential is much more plausible and is believed to be the most reliable value to date. The desired bonding energy, $D_0^0(\text{PF})$, is identical to that²³ deduced from a modified Birge-Sponer treatment of the spectroscopic data²⁴ (see Table III-3). In contrast with NF^- , the PF^- ion is predicted to be thermodynamically quite stable at moderate temperatures.

¹⁸R. C. Sahni, *Trans. Faraday Soc.* **63**, 801 (1967).

¹⁹W. C. Price, T. R. Passmore, D. M. Roessler, *Discuss. Faraday Soc.* **35**, 201 (1963).

²⁰J. T. Hesson, V. H. Dibeler, *J. Chem. Phys.* **32**, 1884 (1960).

²¹R. M. Reese, V. H. Dibeler, *J. Chem. Phys.* **24**, 1175 (1956).

²²Y. Wada, Ph.D. thesis, Kansas State University (1965).

²³P. A. G. O'Hare, USAEC report ANL-7459 (1968).

²⁴A. E. Douglas, M. Frackowiak, *Can. J. Phys.* **40**, 832 (1962).

IV. ANALYTICAL AND REACTOR CHEMISTRY

A. Chemistry of Irradiated Fast Reactor Fuels and Materials

The study of the chemical behavior of irradiated fast reactor fuels has as its principal objective the collection of chemical data that will aid in the understanding of the complex chemical processes that take place in these fuels during irradiation. The current effort is directed toward the study of irradiated uranium-plutonium mixed-oxide fuels, with emphasis on fuel-cladding interactions, fission-product distributions, uranium-plutonium redistribution, and oxygen gradients.

1. Distribution of Noble Fission-Product Gas in Mixed-Oxide Fuels

Pressure from fission gases retained in ceramic fuels during irradiation may contribute to the swelling of fuel during irradiation. Generally, measurements of fission gases have been made only on the amount released from the fuel matrix during irradiation. This amount may vary from 30 to 80% of the total amount of gas calculated to be present, depending primarily on fuel density, power density, and thermal cycling. The distribution of the gas remaining in the fuel is thought to be a function of such parameters as temperature gradient and fuel porosity; that is, the central hotter regions would contain less gas per unit volume than the outer, cooler regions. However, because of greater porosity, small particle sizes, and cracking of the fuel in the cooler regions, gas may be released rapidly in local regions and, therefore, the data indicate wider scattering in gas concentration than in the inner regions.

Experimental data on the radial distribution of fission gases retained in irradiated fuels is needed in the development of fuel-swelling models. A method has therefore been developed for determining the relative distribution of ^{85}Kr in irradiated fuels as a function of radial position. The method utilizes laser-beam vaporization to release the krypton contained in a small sample of fuel. The experimental procedure is as follows: (1) the laser is focused on a selected area of the fuel sample held within a vacuum chamber, (2) the chamber is evacuated and inactive krypton carrier gas is added to prevent adsorption of ^{85}Kr on the walls of the system, (3) the laser is fired, and (4) the released ^{85}Kr and carrier gas are mixed and pumped cryogenically through a Millipore filter (to remove other fission-product activity) to a sample tube for subsequent beta counting. The craters produced by volatilization of the fuel samples are 60-80 μm in diameter. The volumes of the volatilized samples are determined from measurements of silicone rubber replicas of the specimen surface.

Preliminary experimental work was done on a cross section of a vibratorily compacted (vibrapacked) fuel of UO_2 -20 wt % PuO_2 . The sample,

designated SOV-3, had an average density 83% of theoretical and had been irradiated to 3.7 at. % burnup at a maximum linear power rating of 21.4 kW/ft. Laser samples were taken from three regions of the fuel: (1) the inner and outer columnar-grain region (the innermost region of the fuel, which attained the highest temperature during irradiation), (2) the equiaxed-grain region (an intermediate temperature zone), and (3) the unrestructured region (the outermost, coolest region). The amount of ^{85}Kr in the columnar grains was greater than in the equiaxed region, and the largest amount was in the unrestructured region. The ^{85}Kr contents of various regions of SOV-3 are given in Table IV-1 in units of cpm/ μm^3 of fuel. It should be emphasized that these values represent concentrations relative to each other and are not absolute values for the ^{85}Kr content.

TABLE IV-1. Radial Distribution of ^{85}Kr in Irradiated
 UO_2 -20 wt % PuO_2 Fuel (SOV-3)

Fuel Region	Distance from Fuel Center (mm)	^{85}Kr (10^3 cpm/ μm^3)
Void edge ^a	1.10	-
Inner columnar grains	1.29	9.34
Middle columnar grains	1.95	17.2
Outer columnar grains	2.47	10.7
Equiaxed grains	2.76	5.40
Unrestructured region	3.02	38.2
Inner cladding wall	3.175	-

^aOxide fuels that have attained high burnups usually have a void space in the center of the fuel, which results from densification during irradiation.

A more detailed examination was made of the radial distribution of ^{85}Kr in a specimen of pellet fuel of 95% theoretical density, irradiated to 6.5 at. % burnup at a maximum linear power rating of 16 kW/ft. This fuel sample (F2R) was obtained from the General Electric Laboratory at Vallecitos. The examination of F2R was made in three separate experiments. The data are given in Fig. IV-1, where cpm of $^{85}\text{Kr}/\mu\text{m}^3$ of fuel is plotted as a function of radial position.

The results from SOV-3 and F2R show major differences in the relative distribution of ^{85}Kr in the two types of fuel. However, the high-density pellet fuel sample (F2R) that was irradiated at a lower maximum linear power is of greater interest because it is more representative of LMFBR prototype fuels than the low-density, vibrapacked SOV-3 fuel. The data from F2R show good reproducibility in the columnar-grain region. The greater variation in the data for the unrestructured region and

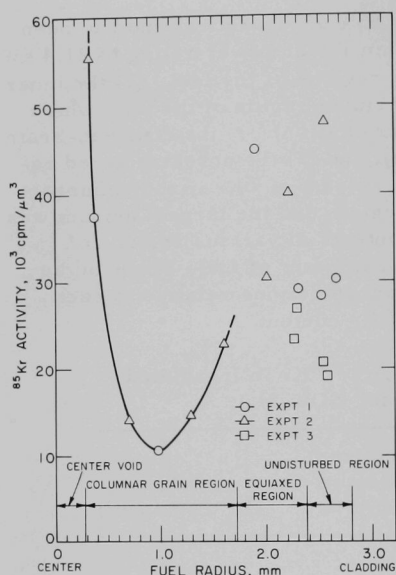


Fig. IV-1. Radial Distribution of ^{85}Kr in Irradiated UO_2 -20 wt % PuO_2 Fuel (F2R).
ANL Neg. No. 308-2325 Rev. 1.

microsampling and microanalysis directly, is being used to provide information about fuel-cladding interactions, the distribution of fission products, and the formation of metal inclusions in irradiated fuels. A detailed examination has been made of metal inclusions found in transverse cross sections of the mixed-oxide fuels, HOV-15 and F2R. HOV-15, a vibra-packed UO_2 -20 wt % PuO_2 fuel of 79.8% average density, was clad with Hastelloy X and had been irradiated in EBR-II to a maximum burnup of 3.5 at. % at 21.4 kW/ft. A description of F2R was given in the preceding subsection.

In each fuel, metal inclusions were examined along several different radial sectors. Each radial sector extended along a line roughly corresponding to a single columnar grain, from the void edge to the termination of the columnar grain and beyond to the cladding wall. The metal inclusions varied in size from 3 to 10 μm and were irregular in shape. All inclusions found in the columnar-grain region contained the noble metal fission products molybdenum, technetium, ruthenium, rhodium, and palladium, as well as iron, which we believe is transported into the fuel from the cladding. The metal inclusions varied in composition as a function of radial position but all were free of uranium and plutonium. In HOV-15, a group of inclusions found near the cladding contained a mixture of cladding

equiaxed-grain region may reflect the heterogeneity of the gas distribution on a microscale or it may be a consequence of the more open fuel structure in this region, which would allow gas communication over larger fuel volumes. The high krypton concentration at the hot void edge suggests that pore migration toward the hotter end of the thermal gradient is occurring, with trapped bubbles of gas accumulating at the void edge. Pore migration at the cooler ends of the columnar grains does not appear to lower the gas concentration as effectively as in the mid-columnar grain region; moreover, substantial amounts of fission gas remain in the outer regions of the fuel.

2. Electron Microprobe Analysis of Irradiated Mixed-Oxide Fuels

The electron probe microanalyzer, which accomplishes

and fission-product components: iron, molybdenum, palladium, nickel, copper and cobalt. The data for one radial sector of HOV-15 are given in Table IV-2 and those for one radial sector of F2R, in Table IV-3.

TABLE IV-2. Metal Inclusions in Irradiated UO_2 -20 wt % PuO_2 Fuel (HOV-15)

Radial Distance (mm)	Concentration (wt %)								
	Fe	Mo	Tc	Ru	Rh	Pd	Ni	Co	Cu
1.19	Void Edge								
1.26	0.13	26.9	16.8	45.0	8.4	2.7	<0.01 ^a	<0.01 ^a	<0.01 ^a
1.39	0.15	22.4	14.6	51.1	9.1	2.7	<0.01 ^a	<0.01 ^a	<0.01 ^a
1.73	0.36	31.3	11.7	41.9	12.0	2.9	<0.01 ^a	<0.01 ^a	<0.01 ^a
1.94	0.46	28.2	11.9	41.0	15.7	2.8	<0.01 ^a	<0.01 ^a	<0.01 ^a
2.06	0.46	31.1	13.2	41.7	10.8	2.8	<0.01 ^a	<0.01 ^a	<0.01 ^a
2.24	0.27	30.3	12.4	40.9	12.6	3.5	<0.01 ^a	<0.01 ^a	<0.01 ^a
2.35	0.32	32.5	13.2	38.0	11.3	4.7	<0.01 ^a	<0.01 ^a	<0.01 ^a
2.48	0.33	37.8	13.4	30.5	10.9	7.0	<0.01 ^a	<0.01 ^a	<0.01 ^a
2.71	0.13	25.5	48.9	11.7	10.8	2.9	<0.01 ^a	<0.01 ^a	<0.01 ^a
2.76	13.1	51.3	19.7	1.7	10.9	1.7	1.5	<0.01 ^a	<0.01 ^a
2.85	39.0	9.8	<0.04 ^a	<0.04 ^a	<0.04 ^a	23.8	20.2	0.7	6.4
2.87	37.1	10.8	<0.04 ^a	<0.04 ^a	<0.04 ^a	20.6	23.0	1.2	7.2
2.91	37.7	8.0	<0.04 ^a	<0.04 ^a	<0.04 ^a	21.2	23.8	1.3	8.0
3.17	Cladding Edge								

^aMinimum detection limits.

TABLE IV-3. Metal Inclusions in Irradiated UO_2 -20 wt % PuO_2 Fuel (F2R)

Radial Distance (mm)	Concentration (wt %)					
	Mo	Tc	Ru	Rh	Pd	Fe
0.30	Void Edge					
0.38	55.4	12.7	21.5	5.0	5.0	0.5
0.84	51.3	8.6	23.0	7.3	9.2	0.6
1.16	47.9	12.6	29.4	9.9	0.1	0.2
1.45	48.0	14.2	29.0	8.2	0.4	0.2
1.69	43.2	15.9	31.5	9.1	0.1	0.1
1.91	30.5	19.5	39.0	11.0	0.1	0.1
2.21	45.5	14.8	31.3	8.1	0.1	0.1
3.17	Cladding Edge					

For HOV-15, the ratios of fission-product concentrations in the inclusions were compared with the ratios that would be expected on the basis of their fission yields. In the first seven inclusions listed in Table IV-2 (those from the fuel interior), the ratios of the three fission products Ru:Rh:Tc agree reasonably well with the calculated fission-yield ratios of 3.8:1.5:1.0; however, the observed concentrations of molybdenum are only one-half of those expected from the fission yields. The palla-

dium content of inclusions in the high-temperature regions is also lower than expected. The high vapor pressure of palladium, along with the greatly increased concentrations observed in the three outermost inclusions, suggest that palladium is transported to the outer, cooler regions by vaporization. In the outer regions, the formation of iron-palladium alloys lowers the vapor pressures of both palladium and iron. It is seen that the three inclusions nearest the cladding (see Table IV-2) contain appreciable amounts

of both iron and palladium. These three inclusions were relatively large and, on a mass basis, it appears that a large percentage of the fission product palladium has been transported to the outer regions of the fuel.

The three inclusions nearest the cladding also contained large concentrations of cladding constituents. The cladding material, Hastelloy X, has a nominal composition of 47% Ni, 9% Mo, 22% Cr, 18% Fe, and small amounts of cobalt, copper, and tungsten. The cladding components were homogeneously distributed throughout each inclusion, iron and nickel being the major constituents. The transport of iron from stainless steel by a van Arkel-de Boer type of process has been previously reported (ANL-7650, p. 35). This type of transport process, however, would not account for the large amounts of nickel found in the inclusions described above. Analysis of several inclusions in HOV-15 in the region near the cladding has shown evidence of the presence of chlorine. Chlorine in the fuel during irradiation could cause significant vapor-phase transport of cladding constituents, particularly nickel.

For the high-density pellet fuel, F2R, the ratios of the concentrations of the three fission products Ru:Rh:Tc again show good agreement with ratios calculated from fission-yield data. However, we see a significant difference, as compared with the low density fuel, in the distribution of iron and the metallic fission-product components that have an appreciable vapor pressure, i.e., palladium and molybdenum. In the cooler regions of the high-density fuel, the concentrations of these components are smaller, and in the interior fuel regions, the concentrations are larger. The marked difference in the behavior of these fission products could be the result of the difference in connected porosity of the two fuels. In F2R, the vapor species appear to be contained in the fuel interior by the high density of the unrestructured region, whereas in HOV-15, the greater porosity of the low-density fuel allows greater transport of the vapor species to cooler regions of the fuel.

In F2R, the distribution of palladium, iron, and molybdenum throughout the columnar-grain region is expected to be governed by transport of elemental vapor species, since all three have significant elemental vapor pressures and would not be oxidized in the higher temperature regions. The metallic inclusions nearest the void edge show a sharp increase in molybdenum, palladium, and iron contents. This finding is somewhat unexpected; however, similar increases in concentration near the void edge have been observed for ^{85}Kr and cesium. This distribution is believed to be characteristic of gaseous components. Pore sweeping is known to occur in this region of the fuel and the thermal gradient diminishes at the void edge. Thus, this region is a potential location for the pile-up of gas-filled pores sweeping toward the void edge. Also, with cracks in the fuel providing a communication line to the central void, palladium, molybdenum, and iron vapor species trapped in the central void cavity may, upon slow cooling of

the fuel, diffuse back into the fuel and condense as alloy inclusions near the void edge. The relatively small total amounts of molybdenum, iron, and palladium involved in the metal inclusions indicate that the transport of vapor back into the fuel has not been extensive.

B. Fast-Reactor Cross-Section Measurements

An understanding of fast-neutron processes is essential to the design and development of fast breeder reactors. The objectives of the cross-sections program are (1) to provide data for defining the breeding characteristics of a fast reactor and for characterizing the irradiation environment of a fast reactor, (2) to measure spectrum-averaged cross sections and fast-neutron fission yields in various fast-reactor neutron spectra, and (3) to apply these data to problems of interest to the overall fast breeder reactor program. The emphasis of this program has historically involved measurements of cross sections and reaction rates in the EBR-II reactor. The more recent trend has been to carry out cooperative experiments with both the EBR-II Project and the Materials Science Division so that our expertise in foil-activation rate measurements, cross sections, and general nuclear chemistry may be combined with their expertise in irradiation-damage effects and reactor physics in an attempt to consider more multidisciplinary problems.

The work of the group during the past year has included the following: (1) measurements of capture-to-fission ratios (α) of the principal heavy elements that constitute both present and future fast reactor fuels, (2) some studies of helium production in EBR-II irradiated stainless steels and the possible relationship of helium production to irradiation damage effects, (3) a comprehensive program to measure the fast-neutron fission yields of tritium and other low-mass fission products, and (4) fast-neutron spectral characterization studies, with particular emphasis on the foil-activation studies conducted in the ZPR-3 mockup studies of EBR-II.

1. Spectrum-Averaged Measurements

a. Capture-to-Fission Ratios in EBR-II

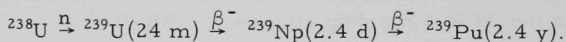
The economics of a breeder reactor is largely dependent upon the reactor's capability for breeding, i.e., producing more fissile fuel than it consumes. For this reason it is very important to determine the breeding capability of a fast reactor. One measure of the breeding capability is the breeding potential, defined as the maximum number of neutrons available for breeding. This quantity can be calculated as follows:

$$B = \frac{(\nu - 1 - \alpha)}{(1 + \alpha)}$$

where ν is the number of neutrons emitted per fission event in the primary fuel and α is the ratio of the number of captures to the number of fissions taking place in the fuel. Each of these quantities is spectrum dependent, that is, each varies with neutron energy spectrum and hence with position in the reactor. Since $\nu(E)$ is a function that varies relatively slowly with neutron energy, the breeding potential is largely determined by the variation of α with neutron energy, i.e., with position within the reactor. Our program has involved measuring α for ^{233}U at 9 locations throughout EBR-II, ^{235}U at 11 locations, ^{238}U at 5 locations, ^{239}Pu at 15 locations, ^{240}Pu at 10 locations, and ^{242}Pu at 14 locations.

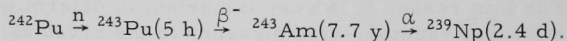
The measurements were performed by irradiating these 64 samples in EBR-II for periods of 0.5 to 1.6 yr. The number of fissions occurring in each sample was measured by radiochemically separating the fission product ^{137}Cs , assaying the activity by counting on Ge(Li) detectors relative to an absolute standard of ^{137}Cs , and computing the number of fissions from the measured number of ^{137}Cs atoms in the sample and the known fission yields of ^{137}Cs for each isotope. The number of captures was measured in the ^{233}U , ^{235}U , ^{239}Pu , and ^{240}Pu samples by radiochemically separating the uranium or plutonium from stainless steel encapsulation material and fission products, and determining the number of atoms of capture products by mass-spectrometric isotope-dilution techniques.¹ For ^{233}U , ^{235}U , ^{239}Pu , and ^{240}Pu , the number of atoms of the respective capture products, ^{234}U (2.5×10^5 y), ^{236}U (2.4×10^7 y), ^{240}Pu (6.8×10^3 y) and ^{241}Pu (13 y), could be determined directly because their half-lives are suitably long. However for ^{238}U and ^{242}Pu , whose capture products have shorter half-lives, the number of captures was determined by measurement of a daughter of the capture product.

For ^{238}U , the following reactions are involved:



The number of captures in these samples was determined by radiochemically separating plutonium and determining the number of atoms of ^{239}Pu by high-resolution alpha counting.

For ^{242}Pu , the following reactions are involved:



The number of captures in the ^{242}Pu samples was determined by first radiochemically separating the americium and then determining the number of atoms of ^{243}Am . This was accomplished by allowing the ^{243}Am to reach

¹The mass spectrometry was performed by M. Laug, Idaho Division.

equilibrium with its decay product ^{239}Np , separating the ^{239}Np , and counting the ^{239}Np on Ge(Li) detectors relative to an absolute standard of ^{243}Am - ^{239}Np .

The results of these measurements are shown in Figs. IV-2 to IV-5. In these figures, the measured values of alpha are plotted against the axial or radial distance of the samples from the center of the core of EBR-II. Error estimates for the experimental measurements have been made on the basis of a propagation-of-error analysis. In general, the relative errors are about 2-3% except for the ^{242}Pu values. The results for ^{242}Pu shown in Figs. IV-4 and IV-5 have not yet been corrected for fissions resulting from ^{239}Pu and ^{241}Pu impurities in the samples; consequently, no error estimates have been made. The error estimates of 2-3% do not include any uncertainties in the assumed fission yield of ^{137}Cs , which is probably of the order of 5-15%. Table IV-4 summarizes the breeding potential, $(\nu - 1 - \alpha)/(1 + \alpha)$, for the fissile nuclides ^{233}U , ^{235}U , ^{239}Pu , and ^{240}Pu .

b. Helium Production in EBR-II Irradiated Stainless Steel

In cooperation with the Materials Science Division, a study was made of helium generation in sections of the control and safety-rod thimbles in EBR-II, and the results of the study have been published.² The

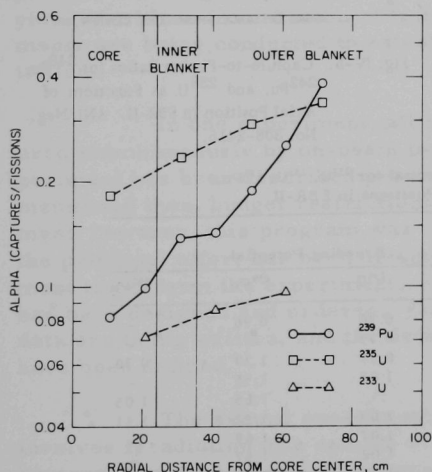


Fig. IV-2. Capture-to-Fission Ratios for ^{239}Pu , ^{235}U , and ^{233}U as Functions of Radial Position in EBR-II. ANL Neg. No. 308-2418.

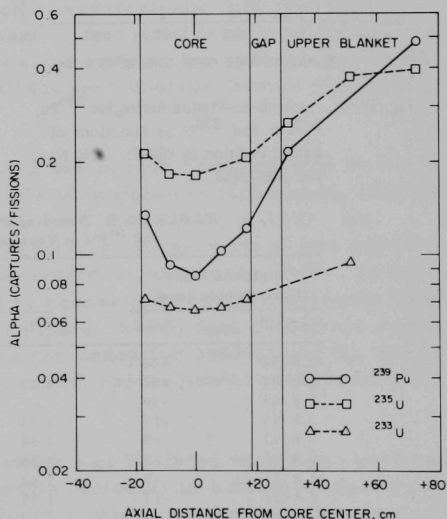


Fig. IV-3. Capture-to-Fission Ratios for ^{239}Pu , ^{235}U , and ^{233}U as Functions of Axial Position in EBR-II. ANL Neg. No. 308-2417.

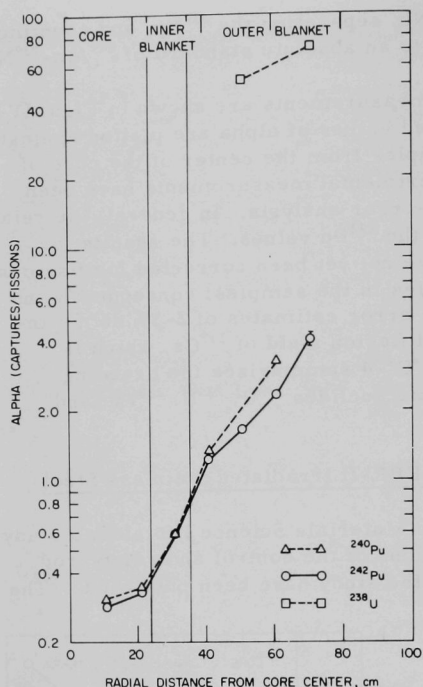


Fig. IV-4. Capture-to-Fission Ratios for ^{240}Pu , ^{242}Pu , and ^{238}U as Functions of Radial Position in EBR-II. ANL Neg. No. 308-2416.

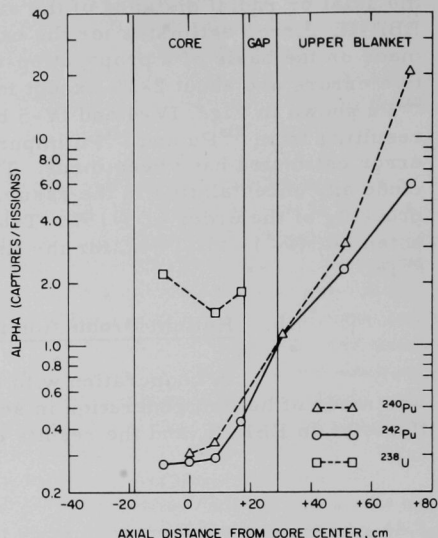


Fig. IV-5. Capture-to-Fission Ratios for ^{240}Pu , ^{242}Pu , and ^{238}U as Functions of Axial Position in EBR-II. ANL Neg. No. 308-2415.

TABLE IV-4. Breeding Potential for ^{233}U , ^{235}U , ^{239}Pu , and ^{240}Pu at Various Positions in EBR-II

Distance from Core Center (cm)		Breeding Potential			
Radial ^a	Axial	^{233}U	^{235}U	^{239}Pu	^{240}Pu
2.8 (1)	+73	-	0.76	0.96	-
2.8 (1)	+52	1.29	0.79	-	-
2.8 (1)	+30	-	0.93	1.39	0.30
2.8 (1)	+17	1.33	1.03	1.58	-
2.8 (1)	+9	1.34	-	1.65	1.05
2.8 (1)	0	1.35	1.07	1.72	1.11
2.8 (1)	-9	1.34	1.07	1.69	-
2.8 (1)	-17	1.33	1.02	1.57	-
10.2 (3)	0	-	1.07	1.71	1.11
21.3 (5)	0	1.33	-	1.65	1.04
30.6 (7)	0	-	0.989	1.55	0.73
40.8 (9)	0	1.30	-	1.54	0.18
51.0 (11)	0	-	0.895	1.44	-
61.2 (13)	0	1.28	-	1.31	-
71.5 (15)	0	-	0.830	1.09	-

^aThe numbers in parentheses indicate the row in which the samples were irradiated.

helium concentrations were measured at selected sampling positions and, on the basis of cross-section data and dosimetry measurements on the samples, the helium concentrations were calculated. This study indicated that helium generation rates in stainless steels can be calculated for EBR-II irradiations with an accuracy of about 25-30%. The most significant finding in this study was the observation of helium and nitrogen concentration gradients along the thimbles; these concentration gradients were very strongly correlated with the temperature of the thimble during irradiation. This phenomenon is thought to result from transport of nitrogen by the sodium coolant from the cooler to the hotter regions of the reactor; in the hotter regions, the nitrogen diffuses into stainless steel, where it can undergo (n,α) reactions to produce helium. Because helium acts to stabilize voids in stainless steels irradiated at high temperatures, it can thereby accelerate deterioration of the mechanical properties of stainless steel under fast-neutron irradiations. Nitrogen transport in LMFBRs has the potential of creating the same problem in fast reactors that boron creates in thermal reactors, namely, an accelerated loss of ductility of steels under neutron irradiation.

2. Low-Mass Fast-Neutron Fission Yields

The purpose of this program is to establish information on tritium that will be useful in the design of reactors and fuel processing plants. The single most important quantity that must be determined is the yield of tritium from fission of fast reactor fuels. Two independent experiments are being conducted to establish the fast-neutron fission yields of tritium.

In one experiment, all low-mass fission products will be measured simultaneously by on-beam particle identification techniques; this experiment has been described previously (see ANL-7675, p. 119). As mentioned then, budget restrictions required a curtailment of this experiment; however, this program was reactivated in September 1970. To date, the principal effort has been directed to reassembly of the electronic equipment to perform the experiment. A computer-based data collection system has been designed and ordered. Computer codes for analysis of the expected data are being written, and the details of the experimental measurements have been defined.

The second experiment, which was initiated within the past year, involves irradiation of a sample of fissile material in a monoenergetic fast-neutron flux, radiochemical separation of tritium, and quantitative determination of the tritium by means of low-level gas proportional counting. The equipment for the radiochemical separation has been assembled and checked out. In the separation scheme, the irradiated sample is hydrided with natural hydrogen for a sufficient length of time to allow isotopic exchange with the tritium, and the hydrogen (containing the tritium) is pumped through a

palladium valve, which is permeable only to hydrogen isotopes, to effect separation from other sample constituents. At present, the entire technique for the yield determination is being verified by performing tritium-yield measurements on thermal-neutron-irradiated ^{235}U , for which tritium yields have been reported in the literature. Samples of ^{239}Pu , ^{233}U , and ^{235}U were irradiated at three different energies with monoenergetic neutrons. The number of fissions occurring in each sample was determined by nondestructive gamma-spectrometric analysis for fission products whose fission yields are well known. After verification of the tritium radiochemical separation procedure, these samples will be analyzed for tritium and the tritium yields determined.

3. Dosimetry Characterization of a Fast-Neutron Irradiation Environment

The principal objective of this program is to develop methods and to perform measurements to characterize the flux intensity, fluence, and neutron spectrum of a fast-reactor environment. Several experiments have been performed in collaboration with the EBR-II Project. The experiments are being conducted in the ZPR-3 critical assembly, which has been mocked-up to simulate the irradiation conditions of EBR-II. Our participation in the experiments has been to perform activation-rate measurements using ^{235}U , ^{238}U , nickel, gold, and aluminum foil dosimeters. The foil data provide information for the comparison of experimental measurements with reactor physics calculations. These experiments thus provide dosimetry data that can be directly related to EBR-II measurements, and they also enable an evaluation and definition of the accuracy of the theoretical calculations to be made. Measurements in four different assemblies on over 500 individual samples have been completed.

More general work in the area of dosimetry has been conducted on a rather limited basis. A computer code, MODSIG, is being developed with which neutron flux and neutron energy spectra can be deduced from foil-activation-rate data. Also, a computer code is being developed that will relate neutron flux and spectrum to atomic displacements. The need for computing atomic displacement is twofold. Firstly, this quantity, which is derived from flux and spectrum measurements, is more directly applicable to studies of materials irradiation effects. Secondly, atomic displacement calculations are required for relating the results of charged-particle simulation experiments (being conducted by the Materials Science Division) with fast-neutron irradiation effects.

C. Fission Yields as a Function of Neutron Energy

Currently, determinations of burnup of both driver fuel and test fuels irradiated in EBR-II are made by analyzing the fuel for such fission products as ^{99}Tc , ^{139}La , and ^{148}Nd . The fission yields of these nuclides have

been determined in a thermal neutron spectrum and in the relatively hard spectrum of EBR-I; however, no information is available on the fission yields in the spectrum of EBR-II nor on the variation of the yields with neutron energy. Therefore, the fission yields being used for burnup determinations in EBR-II are, of necessity, estimates. A 4-yr irradiation of samples of fissile nuclides in the core of EBR-II (see ANL-7350, p. 94) was recently completed and it is expected that the analysis of these samples will provide accurate fission-yield data for the core of EBR-II.

An experimental evaluation of the variation of fission yields with neutron energy is also being carried out to establish the applicability of the fission-yield data obtained in the spectrum of the EBR-II core to other neutron spectra. This information is necessary because the neutron spectrum in which the 4-yr irradiation was conducted was somewhat harder than the spectra of most other EBR-II irradiations and also harder than the spectra expected in the Fast Flux Test Facility (FFTF) and other LMFBRs. The evaluation is being accomplished by performing brief, low-power irradiations in the Zero Power Reactor-3 (ZPR-3) and determining the absolute and "relative" fission yields of a number of gamma-active fission products as a function of neutron energy.

The irradiations in ZPR-3 were carried out in Assembly 60, which was a mockup of the present loading of EBR-II, and in Assembly 61, in which the ^{238}U blanket of Assembly 60 was replaced with a nickel reflector. Three sets of samples were irradiated in each subassembly in positions corresponding to the core, interface, and blanket (or reflector) of EBR-II. The hardest spectrum was the same as that of the 4-yr EBR-II irradiation and the softest spectrum was softer than any spectrum expected in the large LMFBRs.

Metal foils of ^{235}U , ^{238}U , and ^{239}Pu were irradiated in packages of the type shown in Fig. IV-6. The foils were cut into 0.25-in. sections after the irradiation, and each section was assayed repeatedly with a calibrated

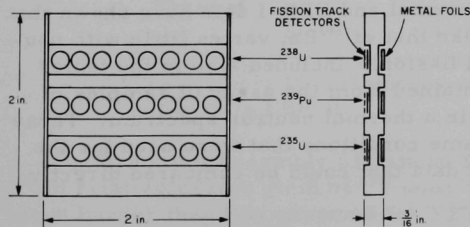


Fig. IV-6. Irradiation Package for Experiments in ZPR-3. ANL Neg. No. 308-2414.

gamma-ray spectrometer over a period of 64 days. For the fission products having a high and known gamma branching ratio, a relatively high fission yield ($>3\%$), and a relatively short half-life (<100 days), the number of atoms of each fission product per gram of fissile nuclide in each section of foil was determined with a precision of 1 to 2%.

The number of fissions that were induced in the foils was determined with mica fission-track detectors, consisting of strips of mica in contact with nanogram depositions

(on platinum) of ^{235}U , ^{238}U , and ^{239}Pu . Each irradiation package contained eight fission-track detectors of each fissile nuclide, one for each 0.25-in. section of foil. (The fission track detectors are represented by the circles in Fig. IV-6.) After the irradiation, the mica was etched with hydrofluoric acid and the number of fission tracks counted under a microscope. The platinum was sectioned and the mass of fissile nuclide on each section measured--the ^{239}Pu by alpha counting, the ^{235}U and ^{238}U by mass-spectrometric isotope-dilution analysis. In previous experiments using this technique, the number of fissions per gram of fissile nuclide has been determined, for a single track detector, with a precision of $\pm 1.5\%$.

The counting of the fission tracks and the assay of the ^{235}U and ^{238}U have not been completed; therefore, a comparison of the absolute fission yields at the various neutron energies cannot yet be made. Calculations have been made, however, of ^{235}U and ^{239}Pu relative fission yields, and these values have been compared as a function of neutron energy. The relative fission yield is defined here as the ratio of atoms of a particular fission product to the atoms of a fission product whose absolute yield does not vary significantly with neutron energy (based on fission yields determined in a thermal spectrum and in the relatively hard spectrum of EBR-I). The yield of ^{140}Ba (12.8 d) shows little variation with neutron energy in either ^{235}U or ^{239}Pu fission; therefore, it has been chosen as the basis of comparison. The absolute yields of several of the fission products assayed on the foils from the ZPR-3 irradiations are known to vary markedly between thermal and EBR-I spectra. For ^{235}U fission, the yields of ^{103}Ru (40 d) and ^{131}I (8.0 d) increase by 17 and 13%, respectively (thermal to EBR-I); for ^{239}Pu fission, the yield of ^{131}I increases by 13%. Any change in yields within the neutron energy range encompassed by the ZPR-3 experiments should, therefore, be most pronounced for these fission products.

The fission yields of ^{95}Zr , ^{103}Ru , and ^{131}I , relative to ^{140}Ba , for ^{235}U and ^{239}Pu fission are summarized as a function of reactor position in Tables IV-5 and IV-6. The ^{95}Zr relative fission yields are included in these tables for comparative purposes (thermal and EBR-I data have shown that the absolute fission yield of ^{95}Zr , like that of ^{140}Ba , varies little with neutron energy for either ^{235}U or ^{239}Pu fission). Included also in the tables are relative fission-yield values obtained from the assay of samples of ^{235}U and ^{239}Pu that were irradiated in a thermal neutron spectrum. These samples were assayed under the same conditions that were used for the ZPR-3 samples to provide thermal data that could be compared directly with the ZPR-3 data.

Since the ^{235}U relative fission yields of ^{103}Ru and ^{131}I (Table IV-5) and the ^{239}Pu relative fission yield of ^{131}I (Table IV-6) do not change from the core spectrum of Assembly 60 (Row 2 of EBR-II) to the blanket spectrum of Assembly 60 (Row 12 of EBR-II), the conclusion is drawn that the fission yields of the other nuclides are also not changing. It follows,

therefore, that for irradiations carried out in EBR-II, the variation in neutron spectrum does not affect the yield of the fission product used to determine burnup on that fuel.

TABLE IV-5. ^{235}U Fission Yields of ^{95}Zr , ^{103}Ru , and ^{131}I , Relative to ^{140}Ba , as a Function of Reactor Position

ZPR-3 Assembly and Sample Location ^a	^{95}Zr	^{103}Ru	^{131}I
60 Core (2)	1.117	0.553	0.561
61 Core	1.139	0.555	0.563
60 Interface (7)	1.101	0.551	0.551
61 Interface	1.110	0.540	0.569
60 Blanket (12)	1.120	0.548	0.548
61 Reflector	1.086	0.516	0.519
Thermal	1.121	0.486	0.443
Std. Dev.	± 0.015	± 0.005	± 0.010

^aThe numbers in parentheses are the corresponding row numbers in EBR-II.

TABLE IV-6. ^{239}Pu Fission Yields of ^{95}Zr , ^{103}Ru , and ^{131}I , Relative to ^{140}Ba , as a Function of Reactor Position

ZPR-3 Assembly and Sample Location ^a	^{95}Zr	^{103}Ru	^{131}I
60 Core (2)	0.910	1.281	0.841
61 Core	0.891	1.272	0.837
60 Interface (7)	-	-	-
61 Interface	0.895	1.265	0.858
60 Blanket (12)	0.880	1.303	0.838
61 Reflector	0.880	1.289	0.837
Thermal	0.910	1.277	0.718
Std. Dev.	± 0.015	± 0.010	± 0.010

^aThe numbers in parentheses are the corresponding row numbers in EBR-II.

From the Assembly 61 data in Table IV-6, it is apparent that the ^{239}Pu relative fission yield of ^{131}I does not change from the core, a spectrum much harder than that expected for FFTF, to the nickel reflector, a spectrum somewhat softer than that expected for FFTF. (In FFTF the principal source of fission will be ^{239}Pu .) It is, therefore, concluded that (1) the absolute yields of the fission products to be used to monitor burnup on FFTF fuel are independent of the neutron spectra in which they will be irradiated, and (2) the analysis of samples from the long-term irradiations in the core of EBR-II will provide ^{239}Pu fission-yield data of the accuracy required for FFTF irradiations.

V. CHEMISTRY OF LIQUID METALS AND MOLTEN SALTS

A. Liquid Metal Studies

Research is being conducted to increase the understanding of liquid metals and semi-metals. Particular emphasis is given to the study of sodium and lithium because of their projected use as coolants in nuclear fission and fusion reactors, respectively. Experimental and theoretical programs under way include the determination of thermodynamic properties (such as binary metallic phase equilibria, metal-metal-hydrogen ternary systems, gas solubilities, and calculation of liquid metal binding) and the measurement of transport properties (such as electronic conductivity of sulfur and sulfur-containing mixtures, diffusion of reaction products in sulfur-containing cathodes of electrochemical cells, surface diffusivity of iron in liquid sodium, and measurement of surface and volume diffusion coefficients).

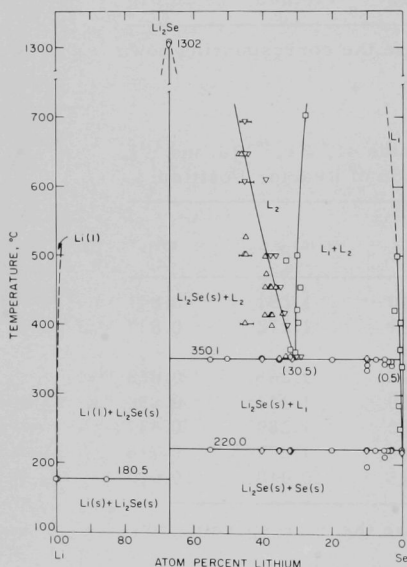


Fig. V-1. Phase Diagram of the Lithium-Selenium System. ANL Neg. No. 308-2327 Rev. 1.

1. Thermodynamics

a. Phase Equilibrium Studies of Binary Lithium-Chalcogen Systems

(1) The Lithium-Selenium System

Phase equilibrium studies of the lithium-selenium system were reported in part earlier (see ANL-7650, p. 42). This system has been studied over the whole range of composition from pure lithium to pure selenium. Various experimental techniques were used to determine the lithium-selenium phase diagram, which is presented in Fig. V-1.

Thermal analysis was used to determine the thermal invariants in the system. The only thermal effect noted on the lithium-rich side of Li₂Se was 180.5°C, the melting point of pure lithium. On the selenium-rich side of Li₂Se, thermal effects were noted at 220.0°C and 350.1°C for all compositions from 55 to 3 at. % lithium. The 220°C effect is associated with selenium melting, whereas the 350°C effect has been interpreted as the temperature of a monotectic reaction. The melting point of Li₂Se was determined by two methods. In the first method, the sample

was placed in a niobium crucible and heated in an argon atmosphere in a molybdenum-wound resistance furnace. Fusion of the Li_2Se occurred at 1303°C . The second method, high-temperature differential thermal analysis with the sample in a niobium capsule, yielded a melting point of 1302°C . From these two types of measurements, the melting point is concluded to be $1302 \pm 5^\circ\text{C}$. There was no indication that the Li_2Se had reacted with the niobium containers.

The indications of a miscibility gap in the lithium-selenium system, based on the thermal analysis results, were confirmed by quenching samples containing from 2 to 26 at. % lithium from temperatures above 350°C . The boundaries of the miscibility gap were determined by chemical analysis of the quenched samples. Samples having compositions within the miscibility gap were held at temperature in sealed quartz vials for periods of up to several days to insure equilibrium and phase separation, and then quenched in liquid nitrogen. The two phases present, which are quite different in appearance, were then separated and analyzed for lithium and selenium. The results of these analyses are shown in Fig. V-1 by the square symbols. The region of immiscibility extends to a relatively high temperature, the consolute temperature being above 800°C . Microscopic study of quenched samples was used to locate the upper liquidus. Samples of various known compositions were heated to a temperature sufficiently high to insure that they were in the liquid region, and then cooled to the temperature of interest, which was maintained for several hours prior to quenching in liquid nitrogen. Compositions which were below the liquidus at the holding temperature contained large, well-formed crystals of Li_2Se , while those above the liquidus prior to quenching contained only fine dendritic crystals of Li_2Se . The different structures were easily distinguishable at low magnification (about 14X), allowing the liquidus composition to be closely bracketed at several temperatures. The results of these experiments are shown by triangles in Fig. V-1, where the base-down orientation indicates that the sample was quenched from below the liquidus and the apex-down orientation indicates quenching from above the liquidus. X-ray diffraction patterns were obtained for a number of samples of various compositions and thermal histories. The only intermediate phase detected was Li_2Se .

(2) The Lithium-Sulfur System

The lithium-sulfur system has proven to be a difficult system to study. Fewer data are available than for the lithium-selenium system discussed above. Qualitatively, however, the two systems appear to be very similar.

Thermal analysis was used to determine the thermal invariants for the system. The results are shown in Fig. V-2 as circles.

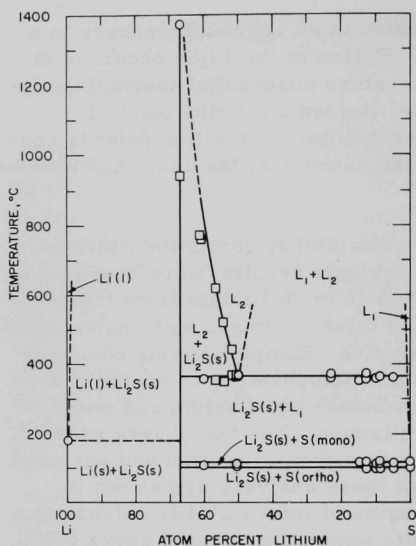


Fig. V-2. Partial Phase Diagram of the Lithium-Sulfur System. ANL Neg. No. 308-2413.

out a eutectic reaction at 365°C. Furthermore, Li_2S does not appear to be polymorphic in this temperature range, and its simple antiferroite structure would not be expected to change with increasing temperature.

The melting point of Li_2S was measured in a molybdenum-wound resistance furnace. Samples were contained in both niobium and vitreous carbon crucibles. The temperature was measured using a calibrated optical pyrometer. The melting point was found to be $1372 \pm 10^\circ \text{C}$, which should represent a lower limit for the melting point of pure Li_2S . This value is considerably higher than that reported by Pearson and Robinson¹ (900-975°C), who observed rapid reaction between Li_2S and their porcelain container.

Work on the lithium-sulfur system will continue in order to establish the validity of the interpretation of the limited amount of data now available.

Previous thermal analysis data by Pearson and Robinson¹ are also shown in Fig. V-2 as squares. There is considerable scatter in the data primarily due to severe undercooling and to the relatively small heats of transformation. The thermal effects noted are at 100°C, 115°C, and 365°C. The effect at 100°C is associated with the transformation from orthorhombic to monoclinic sulfur, whereas the effect at 115°C is associated with the melting of monoclinic sulfur. Neither of these effects is observed on cooling without extreme undercooling (40-60°C). The effect noted at 365°C is presumed to be due to a monotectic reaction, similar to that observed in the lithium-selenium system, since it is present over a wide range of compositions (5-60 at. % lithium). The failure of X-ray diffraction patterns to show any intermediate phase other than Li_2S would seem to rule

¹T. G. Pearson, P. L. Robinson, *J. Chem. Soc.* 1931, 413.

b. Thermodynamics of Lithium-Hydrogen-Metal Systems of Importance to Fusion Reactors

In view of the increasing optimism over obtaining thermonuclear power from controlled fusion reactions,²⁻⁵ the program of experimental studies of liquid metals has been extended to include systems of potential importance to controlled thermonuclear reactor (CTR) technology. In the past year, we have reviewed in depth CTR conceptual designs advanced by other laboratories^{3,6} for deuterium-tritium (D-T) fueled reactors to ascertain the critical and design-independent physicochemical parameters that must be known before operational fusion power plants can be built. These reviews have brought forth several salient points. The first is that it will be economically and ecologically very important to maintain a well confined, well controlled tritium inventory;⁷⁻⁹ another is that much of the basic physicochemical data necessary to accurately estimate tritium inventory are not available. Also, it is apparent that a number of aspects of the recently advanced concepts for D-T fueled reactors are common to all designs. These design-independent aspects are likely to prevail regardless of the size or shape of the reactor. In virtually all designs, the plasma is confined within a metal vessel, the walls of which are held between 800 and 1000°C by means of liquid lithium coolant or in some designs with molten lithium-beryllium fluoride coolant. Tritium needed for fueling the reactor is bred within the cooling fluid by making use of the $\text{Li}(n,\alpha)$ and $\text{Li}(n,\alpha n)$ reactions.¹⁰

Niobium has been selected as the vessel material in most conceptual designs because of its favorable structural, neutron-transmission, and heat-transfer properties. Molybdenum has also received some consideration as a vessel material.³ Nevertheless, it remains to be demonstrated that niobium or molybdenum will be physicochemically compatible with the proposed tritium recovery cycles.^{8,9,11}

In light of these observations and in view of previous experience with lithium hydride-containing systems in this laboratory,¹² an

²D. J. Rose, private communication.

³D. J. Rose, Nuclear Fusion **11**, 183 (1969).

⁴A. J. Hatch et al., "Report of the Argonne Senate Subcommittee on Controlled Thermonuclear Research," Argonne National Laboratory Reviews **6**(1), 30 (1970).

⁵T. Alexander, "The Hot New Promise of Thermonuclear Power," Fortune, p. 94 (June 1970).

⁶Nuclear Fusion Reactors, Proceedings of the British Nuclear Energy Society Conference on Nuclear Fusion Reactors held at the UKAEA Culham Laboratory, 17-19 September 1969, British Nuclear Energy Society (1970).

⁷Ibid., p. 54.

⁸Ibid., p. 441.

⁹A. P. Fraas, H. Postma, "Preliminary Appraisal of the Hazards Problems of a D-T Fusion Reactor Power Plant," USAEC report ORNL-TM 2822 (1970).

¹⁰J. D. Lee, "Some Neutronics Aspects of a D-T Fusion Reactor," USAEC report UCRL-72493 (1970).

¹¹R. W. Werner, "Heat Pipes for Recovery of Tritium in Thermonuclear Reactor Blankets," USAEC report UCRL-72329 (1970).

¹²E. J. Cairns et al., "Galvanic Cells With Fused-Salt Electrolytes," USAEC report ANL-7316 (1967).

experimental program has been initiated to determine thermodynamic and transport properties of lithium-hydrogen-metal systems of expected importance to CTR technology. The metals and alloys under investigation include niobium, molybdenum, TZM (Ta-Zr-Mo alloy), and niobium-1% zirconium.

c. Theoretical Studies in Thermodynamics

(1) Gas Solubility in Liquid Metals

To better understand the unusual solvency properties of liquid metals, it is useful to examine their behavior with respect to the simplest solutes, the noble gases. (Knowledge of the solubility of noble gas blanketing materials and fission products in liquid sodium is also of practical significance to the reactor technologist.) This section presents the results of an effort to develop a physically realistic model of such solutions. In contrast to models previously proposed,¹³ this model explicitly accounts for the effects of the conduction electrons in a liquid metal.

The excess molecular free energy of formation of a dilute solution, Δg^{xs} , may be set equal to the total reversible isothermal work done during three sequential operations: (1) A solute molecule from the gas phase is compressed into a small volume, δV , in which it exerts a pressure, P_h , equal to the internal pressure of the solvent, P_i ; (2) a spherical cavity of volume δV is created in the solvent; (3) the solute molecule is inserted into the cavity and work is done by the attractive forces acting between the solute molecule and the surrounding solvent. The excess molecular free energy, Δg^{xs} , is equal to $w_{comp} + w_{cav} + w_{attr}$.

1) For the calculation of the isothermal work of compression, w_{comp} , hard-sphere theory¹⁴ may be applied; an appropriate equation of state for the hard-sphere gas is the scaled particle or Percus-Yevick approximation

$$\frac{P_h \frac{\pi}{6} a^3}{k_B T} = \frac{y(1+y+y^2)}{(1-y)^3} \quad (1)$$

where P_h is the pressure of a hard-sphere gas; k_B , Boltzmann's constant; T , the absolute temperature; a , the effective hard-sphere diameter; and y , the packing fraction, defined by $\frac{\pi}{6} a^3 \rho$, ρ being the number density of the hard-sphere gas.

¹³G. W. Johnson, R. Shuttleworth, *Phil. Mag.* **4**, 957 (1959); L. F. Epstein, KAPL-MEMO-LFE-10 (1952);

H. Mandel, NAA-SR-MEMO-10745; T. Emi, R. D. Pehlke, *Met. Trans.* **1**, 2733 (1970).

¹⁴H. Reiss, *Adv. Chem. Phys.* vol. IX, I. Prigogine, ed., Interscience Publishers, New York, 1965.

$$w_{\text{comp}} = - \int_{k_B T}^{\delta V} P_h dV - k_B T \int_{\Omega}^{k_B T} \frac{dV}{V} \quad (2)$$

The second term in Eq. 2 is included in order to refer the excess free energy of solution to a standard state appropriate to the definition of the Ostwald coefficient,¹⁵ i.e., the solute gas (considered to be ideal) at the molecular volume Ω of the liquid. On substitution of Eq. 1 into Eq. 2, one obtains

$$w_{\text{comp}} = k_B T \left[\ln \frac{\Omega}{\delta V(1-y)} + \frac{3}{2} \frac{y(2-y)}{(1-y)^2} \right] \quad (3)$$

2) To calculate w_{cav} for a liquid metal, one must allow for the effects of mobile conduction electrons; a simple way to do so is to employ the nearly-free-electron (NFE) model of metals. (In the NFE model, a spatially uniform, immobile distribution of positive charge, corresponding to N positive ions of valence z in a spherical volume V , is counterbalanced by a mobile distribution of conduction electrons having a uniform density $n_0 = zN/V$.) When one removes a small spherical volume, δV , of positive charge from the center of a large metal sphere and distributes it uniformly over the surface, the net electronic work can be analyzed as the sum of three terms. First, the excess negative charge ($en_0\delta V$) left in the cavity repels all the electrons in the conduction band and increases their potential energy; the work of repulsion is given¹⁶ by $n_0\delta V/\eta_F$, where η_F is the density of electronic states at the Fermi energy, E_F , the energy of the highest occupied level in the conduction band. Second, the expansion of the NFE sphere reduces the average kinetic energy of the conduction electrons; because E_F varies as $V^{-2/3}$, the reduction for the most energetic electrons is given by $\delta E_F/E_F = -\frac{2}{3} \frac{\delta V}{V}$. If $\bar{\kappa}_F$ is the ratio of the average kinetic energy (per electron) to the maximum, the total change in the electronic kinetic energy, w_{kin} , is $-\frac{2}{3} \bar{\kappa}_F E_F n_0 \delta V$. Third, the conduction electrons redistribute in the presence of an excess charge in such a way as to completely screen¹⁶ the potential due to the excess charge at large distances. During this redistribution, which takes the form of spatial oscillations¹⁷ of the electron density about its mean value, n_0 , work is done by the electrons; the exact amount depends upon the details of how the excess charge is distributed. For simplicity, the present model assumes the excess charge ($en_0\delta V$) to be uniformly spread over the surface of a spherical cavity of radius $R = (3\delta V/4\pi)^{1/3}$. The work, w_{osc} , done by the electron gas as it responds to this excess charge has been found to be

¹⁵The Ostwald coefficient is defined as the volume of gas dissolved per unit volume of solvent.

¹⁶D. Pines, P. Nozières, The Theory of Quantum Liquids, vol. I, pp. 168, 220, and 292, W. A. Benjamin, Inc., New York (1966).

¹⁷J. Friedel, Nuovo Cim. Suppl. 7, 287 (1958).

$$w_{\text{osc}} = -(n_0 \delta V)^2 \frac{k_F}{2\pi} \int_0^\infty dx \frac{1}{\epsilon(x,0)} \left(\frac{1}{\epsilon(x,0)} - 1 \right) \left(\frac{\sin bx}{bx} \right)^2 \quad (4)$$

where the parameter $b = (9\pi n_0 \delta V^{1/3})/4$, the wave number at the Fermi energy $k_F = (3\pi^2 n_0)^{1/3}$, $\epsilon(x, \omega)$ is the wave number and frequency-dependent dielectric function for the electron gas, and $x = k/k_F$. Summing the contributions, one finds

$$w_{\text{cav}} = (\eta_F^{-1} - \frac{2}{3} \bar{\kappa}_F E_F) n_0 \delta V + w_{\text{osc}} \quad (5)$$

3) The generalized potential due to dispersion forces, ϕ_{disp} , felt by a single molecule B near or within a macroscopic body A has been shown by Linder¹⁸ to be given by the equation

$$\phi_{\text{disp}} = -\frac{3}{4} \hbar \frac{\bar{\omega}_B \bar{\omega}_A}{\bar{\omega}_B + \bar{\omega}_A} \alpha_B(0) g_A(0) \quad (6)$$

where \hbar is Planck's constant divided by 2π , $\alpha_B(0)$ is the static polarizability of the molecule in question, $g_A(0)$ is the static reaction field due to the macroscopic body, and $\bar{\omega}_B$ and $\bar{\omega}_A$ are the frequencies at which the corresponding frequency-dependent functions $\alpha_B(\omega)$ and $g_A(\omega)$ have dominant resonances. The work done in bringing a molecule from a region of zero potential into the fluid is $w_{\text{attr}} \approx \phi_{\text{disp}}$. (The approximation is not important and only amounts to neglect of quadrupolar and higher-order multipolar forces.) For a situation in which the macroscopic body is represented by a solvent continuum having a cavity of radius R in which a solute molecule resides, the reaction field is given by

$$g_A(\omega) = \frac{2\epsilon_A(0, \omega) - 2}{2\epsilon_A(0, \omega) + 1} \left(\frac{1}{R^3} \right) \quad (7)$$

The long wavelength limit of the dielectric function has a particularly simple form for a metal¹⁶

$$\epsilon_A(0, \omega) = 1 - \frac{\omega_p^2}{\omega^2} \quad (8)$$

where ω_p is the plasmon frequency of the metal. Substituting Eq. 8 into Eq. 7, one finds $g_A(0) = R^{-3}$ and $\bar{\omega}_A = (2/3)^{1/2} \omega_p$.

Langhoff and Karplus¹⁹ have derived lowest-order Padé approximants to $\alpha_B(\omega)$, which are, respectively, an upper bound

¹⁸B. Linder, *Advan. Chem. Phys.*, vol. 12, p. 225, J. O. Hirschfelder, ed., Interscience Publishers, New York (1967).

¹⁹P. W. Langhoff, M. Karplus, *J. Chem. Phys.* **53**, 233 (1970); *J. Opt. Soc. Amer.* **59**, 863 (1969).

$$\alpha_B^{(u)}(\omega) = \frac{Z}{(Z/\alpha_0) - \omega^2}; \quad \bar{\omega}_B^{(u)} = (Z/\alpha_0)^{1/2} \quad (9a)$$

and a lower bound

$$\alpha_B^{(\ell)}(\omega) = \frac{\alpha_0^2/\alpha_1}{(\alpha_0/\alpha_1) - \omega^2}; \quad \bar{\omega}_B^{(\ell)} = (\alpha_0/\alpha_1)^{1/2} \quad (9b)$$

In these equations, Z is the total number of electrons in the solute molecule, and α_0 and α_1 are the first two coefficients in the Cauchy series,¹⁹ which represents the experimental frequency-dependent polarizability. Appropriate substitutions yield upper and lower bound values to w_{attr} ; within the expected accuracy of the present model, w_{attr} can be taken as the mean of these two (fairly close) estimates.

4) The total work, Δg^{XS} , done in the solution of an atom of gaseous solute in a liquid metal is related to the molar excess free energy of solution and the Ostwald coefficient, λ , by

$$N_0 \Delta g^{\text{XS}} = \Delta G^{\text{XS}} = -RT \ln \lambda \quad (10)$$

where N_0 is Avogadro's number.

5) Calculations have been carried out for the solution of noble gases in liquid sodium. The input data and the results are collected in Table V-1. The internal pressure P_i of the metallic solvent was computed from its volume expansion coefficient, β_T , and its isothermal compressibility, κ_T , via the relation $P_i \equiv T\beta_T/\kappa_T$. Temperature-independent effective hard-sphere diameters, a , for the solute molecules were taken from the values determined by fitting experimental second virial coefficient data for the gases. With these values, the left hand side of Eq. 1 is known and can be solved for γ , and δV can be determined from $\gamma\delta V = \frac{1}{6}a^3$. Because liquid sodium approximates very well to an ideal, univalent, free-electron metal, further simplifications are possible, e.g., $\eta_F = (\frac{2}{3}E_F)^{-1}$; $E_F = \hbar^2 k_F^2/2m_e$ where m_e is the electronic mass; $\bar{\kappa}_F = \frac{3}{5}$ and $\epsilon(x,0)$ is given by the Lindhard²⁰ formula.

For the computation of w_{attr} , the plasmon frequency, ω_p , is needed. Measurements of this quantity by electron-loss experiments are usually carried out at only one temperature. We have assumed that ω_p can be scaled to the temperatures of interest by the known temperature dependence (ω_p^0 proportioned to $\rho^{1/2}$) of the ideal plasmon frequency of a free-electron gas. In the few cases where the temperature dependence of ω_p has been measured, this assumption appears to be valid.

²⁰J. Lindhard, Kgl. Danske Videnskab. Selskab, Mat. Fys. Medd., 28(8) (1954).

TABLE V-1. Solubility of Noble Gases in Liquid Sodium (500°C)

A. Physical Properties of Liquid Sodium (500°C)							
P_i	= 7650 atm			n_0	$= 2.179 \times 10^{22} \text{ (cc}^{-1}\text{)}^a$		
$\bar{\Omega}$	$= 27.64 \text{ (cc mol}^{-1}\text{)}^a$			β_T	$= 2.86 \times 10^{-4} \text{ (}^\circ\text{C}^{-1}\text{)}^a$		
ω_p	$= 5.24 \text{ eV}^b$			κ_T	$= 2.891 \times 10^{-5} \text{ (atm}^{-1}\text{)}^c$		
B. Physical Properties of Noble Gases				C. Contributions to the Excess Free Energies of Solution ^f			
	He	Ar	Xe		He	Ar	Xe
$(\alpha_0)^d$	1.384	11.091	27.340	$N_0 w_{\text{comp}}$	2.2	2.8	3.4
$(\alpha_1)^d$	1.550	28.16	116.2	$N_0 w_{\text{cav}}$	12.6	20.2	26.8
$(\alpha), \text{\AA}^e$	2.56	3.41	3.97	$N_0 w_{\text{attr}}$	-1.5	-6.7	-12.0
Z	2	18	54	$N_0 g^{\text{XS}} \text{ (calc)}$	13.3	16.3	18.2
$\delta V, \text{\AA}^3/\text{atom}$	38.5	63.9	86.8	$\Delta G^{\text{XS}} \text{ (exp)}$	12.3 ^g	16.6 ^j	18.1 ^k
					12.7 ^h	15.8 ^h	

^aE. I. Goltsova, *High Temp.* **4**, 348 (1966).^b $\omega_p(25^\circ\text{C}) = 5.9 \text{ eV}$, J. L. Robins, P. E. Best, *Proc. Phys. Soc. (London)* **79**, 110 (1962).^cY. S. Trelin, J. N. Vasil'ev, V. B. Proskurin, T. A. Tsyganova, *High Temp.* **4**, 352 (1966).^dRef. 19. Atomic units, $\hbar = m = e = 1$, used.^eSee H. Reiss, *Adv. Chem. Phys.*, vol. 9, 1 (1965); C. C. Lim, D. H. Bowman, R. A. Aziz, *Can. J. Chem.* **46**, 3477 (1968); G. Boato, G. Casanova, *Physica* **27**, 571 (1961).^fValues in kcal mol⁻¹.^gRef. 21.^hRef. 22.^jRef. 23.^kRef. 24.

Reliable experimental Ostwald coefficients for helium,^{21,22} argon,^{22,23} and xenon²⁴ in liquid sodium are presented in Fig. V-3 as the mean values of multiple determinations at each temperature. Calculated values of λ from Eq. 10 are indicated by straight lines. Considering the relative magnitudes of the free energy terms, their uncertainties, and the uncertainty in the experimental results, we conclude that the proposed model provides a fairly reliable calculation of the solubility of noble gases in a liquid metal.

(2) Binding Calculations for Liquid Metals

As the interatomic distance increases, the potential energy of a pair of rare gas atoms decreases, passes through a minimum, and then increases asymptotically to zero. The interaction is repulsive only at the very small interatomic distances where electron overlap is

²¹E. Veleckis, G. Redding, ANL-7675, p. 64 (1970).²²K. Thormeier, *Atomkernenergie* **14**, 449 (1969).²³E. Veleckis, R. Blomquist, R. Yonco, M. Perin, ANL-7325, p. 128 (1967).²⁴E. Veleckis, W. Kremsner, ANL/ST-4, p. 44 (December 1970).

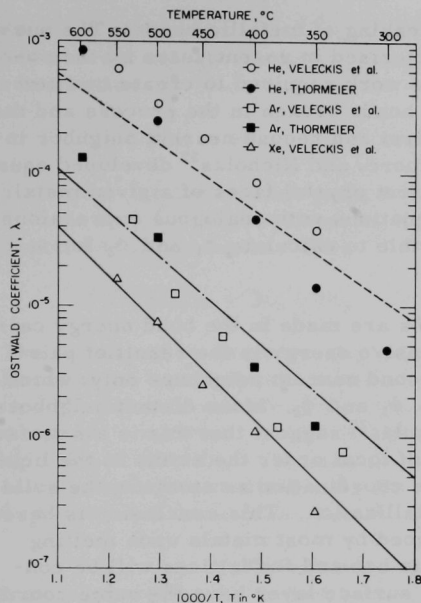


Fig. V-3. Ostwald Coefficients of Helium, Argon, and Xenon in Liquid Sodium (dashed, dot-dashed, and solid lines, respectively, represent Eq. 10 for helium, argon, and xenon dissolved in sodium). ANL Neg. No. 308-2412.

ence of repulsive interactions in liquid metals at longer ranges. The bond energy which characterizes the interaction between a particular pair of atoms in a metal is not related in any simple way to the ion-ion potential for metals which was discussed above. This long-range oscillatory potential provides information on the work necessary to separate the pair of ions in the metallic state. The bond energy, by contrast, is defined in terms of the vaporization process, where the final state is an atomic vapor with localized electrons. Thus, bond energies can be expected to be considerably larger than the ion-ion potential energies in the region of oscillation. Both properties, however, can provide an indication of whether repulsive interactions exist in the metallic state at the larger interionic distances.

To find evidence of repulsive interactions at larger distances, it is necessary to calculate at least the first and second nearest neighbor bond energies, ϕ_1 and ϕ_2 , and this requires two thermodynamic

constrained according to the Pauli exclusion principle. At all larger separations, the interaction is attractive resulting from the induced dipoles of the atoms.

The situation for a crystalline metal or a liquid metal is quite different. According to pseudopotential theory,²⁵ the potential for a pair of ions immersed in the sea of conduction electrons does not asymptotically approach zero at the larger interionic distances, but exhibits instead a damped oscillation about zero. Thus, instead of being attractive at all the larger separations, the interaction is alternately attractive and repulsive as distance increases. This long-range oscillatory behavior is a consequence of the dielectric screening of the ionic core by the surrounding conduction electrons. A potential of this form was first suggested by Friedel,²⁶ and this behavior is often called Friedel oscillations.

It is the purpose of this study to show that simple calculations of bond energies also suggest the presence

²⁵W. A. Harrison, *Pseudopotentials in the Theory of Metals*, p. 52, W. A. Benjamin, Inc., New York (1966).

²⁶J. Friedel, *Phil. Mag.* **43**, 153 (1952).

properties which are related to the breaking of metallic bonds. The surface energy of metals has been characterized in recent years by the so-called broken-bond model by which the work required to create two new interfaces is related to the number of bonds broken in the process and the energy of each type of bond. Taking first and second nearest neighbor interactions into account, Mackenzie, Moore, and Nicholas²⁷ developed equations for the surface energies of different crystal faces of a given metal. Supplementing their surface energy equations with analogous expressions for the heat of vaporization, it is possible to calculate ϕ_1 and ϕ_2 for a variety of metals.

Three assumptions are made in the bond energy calculations. First, the liquid-metal cohesive energy is the result of pairwise interactions between first and second nearest neighbors only, which can be characterized by bond energies ϕ_1 and ϕ_2 . More distant neighbors are neglected; the calculations of Nicholas²⁸ suggest that this is a satisfactory approximation. Second, because of local order the atoms in the liquid interior are assumed to have the same coordination as atoms in the solid lattice formed by the metal upon crystallization. This conclusion is based on the modest volume change experienced by most metals upon melting (2 to 4%). Metals which crystallize into bcc and fcc lattices will be considered here. Third, the atoms in the surface layer have the same coordination that would be expected from cleavage along the closest-packed plane with no relaxation or rearrangement in the surface. The closest-packed surface plane is selected because it has the lowest surface energy.

The heat of vaporization at absolute zero, L_0 , is related to the bond energies ϕ_1 and ϕ_2 through the bulk coordination numbers. In a bcc lattice, the coordination numbers for the first and second nearest neighbor atoms are 8 and 6. Thus, for every atom vaporized, four first and three second nearest neighbor bonds are broken and

$$L_0 = 4\phi_1 + 3\phi_2 \quad (\text{bcc}) \quad (11)$$

Similarly, from the coordination numbers of 12 and 6 in a fcc lattice, it follows that

$$L_0 = 6\phi_1 + 3\phi_2 \quad (\text{fcc}) \quad (12)$$

The surface energy, which is also the surface tension at absolute zero, γ_0 , can similarly be related to the bond energies by noting that the cleavage of a liquid or solid to produce two new surfaces each of area A requires an amount of work $2A\gamma$. For the closest-packed (110) plane of a bcc lattice with a unit cell edge length of a_0 at absolute zero, the

²⁷J. K. Mackenzie, A. J. W. Moore, J. F. Nicholas, *J. Phys. Chem., Solids* **23**, 185 (1962).

²⁸J. F. Nicholas, *Aust. J. Phys.* **21**, 21 (1968).

cleavage of an area $\sqrt{2} a_0^2$ requires the breaking of four first and four second nearest neighbor bonds. Thus, the work required to produce these two new surfaces is

$$2\sqrt{2} a_0^2 \gamma_0 = 4\phi_1 + 4\phi_2 \quad (\text{bcc}) \quad (13)$$

Similarly, for the closest-packed (111) plane of a fcc lattice, the cleavage of an area $(\sqrt{3}/4)a_0^2$ requires the breaking of three first and three second nearest neighbor bonds. Thus

$$(\sqrt{3}/2)a_0^2 \gamma_0 = 3\phi_1 + 3\phi_2 \quad (\text{fcc}) \quad (14)$$

The density of the liquid at absolute zero, ρ_0 , can be used to calculate a_0 . Because the bcc unit cell contains two atoms, $a_0^3 = 2\Omega_0 = 2M/N\rho_0$, where Ω_0 is the atomic volume at absolute zero, M is the molar mass, and N is Avogadro's number. Similarly, from the fcc unit cell with four atoms, $a_0^3 = 4\Omega_0 = 4M/N\rho_0$. To calculate ϕ_1 and ϕ_2 for bcc metals, it is thus necessary to solve simultaneously Eqs. 11 and 13, while for the fcc metals, ϕ_1 and ϕ_2 are found from Eqs. 12 and 14.

Calculations of ϕ_1 and ϕ_2 were performed on all liquid metals where the L , γ , and ρ data were sufficiently reliable to extrapolate to absolute zero. At absolute zero, L , which is an enthalpy, and γ , which is a Helmholtz free energy, both become energies and yield energies for ϕ_1 and ϕ_2 . Tables V-2 and V-3 show the data employed and the calculated bond energies. The results are that (1) ϕ_1 is positive, corresponding to an attractive first nearest neighbor interaction, and (2) ϕ_2 is negative, which implies that the second nearest neighbor interaction is repulsive. Thus, even from this extremely simple model, an indication is obtained of the existence of repulsive interactions at larger interionic distances in metals.

TABLE V-2. Bond Energies for bcc Metals

Metal	L_0 (eV/atom)	ρ_0 (g/cm ³)	γ_0 (erg/cm ²)	ϕ_1 (eV/bond)	ϕ_2 (eV/bond)
Li	1.624	0.546	470	0.869	-0.618
Na	1.096	1.02	220	0.579	-0.406
K	0.914	0.9105	125	0.462	-0.311
Rb	0.840	1.587	95	0.440	-0.307
Cs	0.804	2.02	80	0.419	-0.291
Ca	1.747	1.613	472	0.563	-0.168
Fe	4.135	8.618	2758	1.310	-0.368

TABLE V-3. Bond Energies for fcc Metals

Metal	L_0 (eV/atom)	ρ_0 (g/cm ³)	γ_0 (erg/cm ²)	ϕ_1 (eV/bond)	ϕ_2 (eV/bond)
Ni	4.256	9.908	2348	0.928	-0.437
Cu	3.359	9.077	1629	0.740	-0.361
Ag	2.877	10.53	1136	0.618	-0.277
Al	3.221	2.626	996	0.602	-0.330
Pb	1.979	11.41	538	0.423	-0.186

2. Transport Properties

a. Conductivities of Sulfur and Sulfur-Containing Mixtures

Although much information has been published on the electrical conductivities of solid, crystalline semiconductors, few data are available on the electronic conductivities of liquid elemental semiconductors. Because the mechanism of conduction in liquid semiconductors is not well understood, conductivity data on systems of this type are of considerable theoretical interest. These data are also of practical importance because of the possible use of these materials as cathode reactants in secondary electrochemical cells.

Additional measurements of the conductivity of elemental sulfur and P_4S_3 were made at various temperatures with dc and with ac at frequencies of 0.1, 1.0 and 10.0 kHz. The conductivity cells were made of quartz or Pyrex, and the electrodes were 6.3-mm dia, spectrographic graphite rods with an interelectrode distance of about 4 mm. The sulfur was obtained from the American Smelting and Refining Co. with a purity specification of 99.999+%, and was used without further purification. The P_4S_3 , a relatively impure grade of material from the Eastman Kodak Co., was purified by extraction with CS_2 , followed by sublimation.

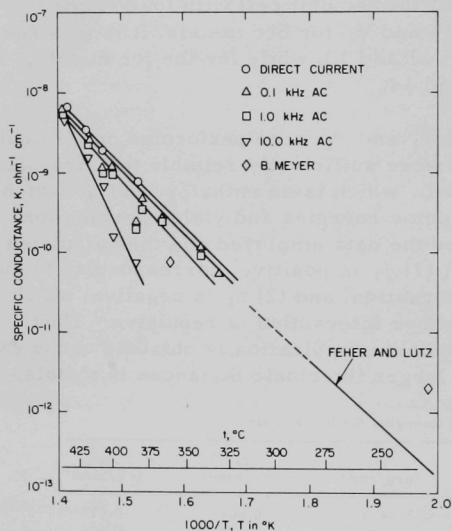


Fig. V-4. Specific Conductance of High-Purity Sulfur. Cell Material: quartz. Leads: tungsten. Electrodes: spectrographic graphite. Atmosphere: helium, 1 atm. ANL Neg. No. 308-2411.

The results of the conductivity measurements on sulfur are presented in Fig. V-4. These values are nearly two orders of magnitude lower than those obtained previously (ANL-7650, p. 48), and they are in reasonable agreement with an extrapolation of the lower-temperature data of Feher and Lutz,²⁹ as well as the

two values quoted by Meyer.³⁰ The conductivity shows the expected linear relationship between $\log \kappa$ and $1/T$ ($^{\circ}K$) over the temperature range of the

²⁹F. Feher and H. D. Lutz, *Z. Anorg. Allg. Chem.* 333, 216 (1964).

³⁰B. Meyer, *Elemental Sulfur*, Interscience Publishers, New York (1965).

measurements (about 300 to 440°C). The conductivity decreased with increasing frequency, and extrapolation of the ac data to zero frequency gave values that agreed well with the dc data. The temperature dependence of the dc conductivities corresponds to an activation energy of 37.2 kcal/g-atom, or 1.62 eV.

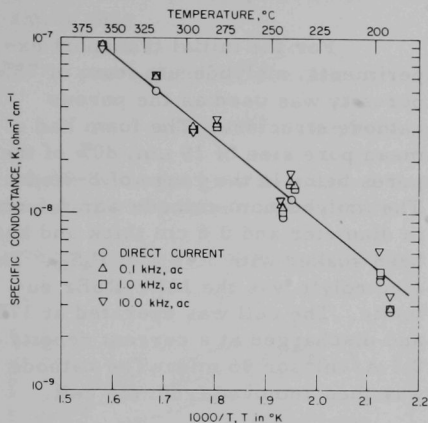


Fig. V-5. Specific Conductance of P_4S_3 (Pyrex cell material, molybdenum leads, spectrographic graphite electrodes, 1-atm helium atmosphere). ANL Neg. No. 308-2410.

increased within this range, the activation energy of the conductivity shows a decrease. These are regarded only as preliminary results; additional data are needed to gain a fuller understanding of the conduction mechanism in these mixtures.

b. Transport Studies in Sulfur-Containing Cathodes

An understanding of transport mechanisms is essential to total understanding of the chemical and electrochemical processes taking place in sulfur cathodes (which are used in lithium/sulfur secondary cells). To gain insight into these mechanisms, a study was undertaken of the transport of reaction products in cathodes containing sulfur and sulfur-phosphorus compounds. The experimental plan was to operate a $Li/LiBr-RbBr/Li$ in S or P_4S_{10} cell so as to deposit a known amount of lithium at the cathode-electrolyte interface, and then to determine analytically the concentration profiles of lithium-containing reaction products in the porous cathode structure. By studying these profiles as a function of temperature, deposition rate, and cathode structure, it was intended that transport properties such as diffusion coefficients would be determined.

The cell designed for these experiments is shown in Fig. V-6. After lithium has been electrochemically transferred to the

The results of the P_4S_3 conductivity measurements are shown in Fig. V-5. The data show a linear $\log \kappa$ vs $1/T$ ($^{\circ}K$) relationship with an activation energy of 10.8 kcal/mol, or 0.47 eV. Although the data scatter somewhat, particularly at the lower temperatures, there appears to be no systematic dependence of the conductivity upon frequency. These results, together with those for sulfur and some earlier data on sulfur-phosphorus mixtures, show that the conductivity of sulfur increases sharply with increasing additions of phosphorus up to a concentration of about 10 at. %. As the phosphorus concentration is in-

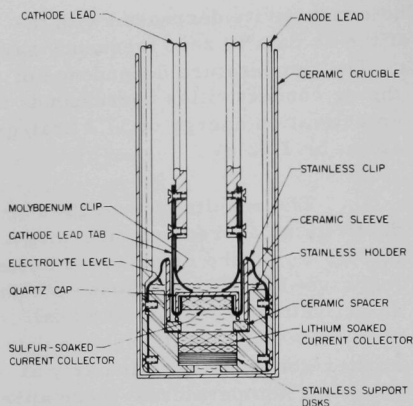


Fig. V-6. Experimental Lithium/Sulfur Cell for Mass-Transport Studies. ANL Neg. No. 308-2409.

cathode, the cathode is removed and allowed to cool. The quartz cap is then broken and the cathode is sectioned for analysis.

For the initial transport experiments, molybdenum foam of 75% porosity was used as the porous cathode structure. The foam had a mean pore size of $19\text{ }\mu\text{m}$, 80% of the pores being in the range of $8\text{--}36\text{ }\mu\text{m}$. The molybdenum cathode was 2.5 cm in diameter and 0.6 cm thick and had been soaked with 3.46 g of P_4S_{10} . The electrolyte was the LiBr-RbBr eutectic. The cell was operated at 375°C and discharged at a current density of 0.1 A/cm^2 for 96 min. The cathode was then removed from the cell.

A core 0.8 cm in diameter was taken from the cathode. Two sections 0.13 cm thick were taken from the end of the core that had been in contact with electrolyte. Analysis showed less than 5 mg of sulfide in each section. This contrasts with approximately 50 mg of sulfide expected on the basis of the amount of lithium transferred.

The analysis indicates that very little reaction product is transported into the porous molybdenum structure. Microscopic examination supports this conclusion, since the reaction products appear to be concentrated in a very thin layer at the surface that was in contact with the electrolyte. The charge-discharge behavior of similar cells also indicates that very little product diffuses into the cathode. Since this behavior would not be expected on the basis of temperature, viscosity, or deposition rate, it appears that the cathode current collector structure is of great importance in determining the mass-transport behavior of reaction products in the cathode.

c. Surface Diffusivity of Iron in Liquid Sodium

A study of the rate of grain-boundary grooving of α -iron (bcc) in liquid sodium has been carried out to determine (1) the importance of surface diffusion in the corrosion and transport processes that occur in a sodium environment and (2) whether the sodium environment enhances surface-tension-driven mass transport over that observed in a vacuum environment. In the last annual report of the Chemical Engineering Division (ANL-7675, p. 66), a discussion of sample preparation, annealing, and interferometric examination was presented, along with some preliminary results at 800°C . Since then experiments were performed at 600, 700, 800, and 880°C , and the results of this further analysis are presented here.

Since the development by Mullins^{31,32} of a theory of grain-boundary grooving, it has been possible to distinguish between the mass-transport mechanisms of surface and volume diffusion and to determine the diffusion coefficient through the rate of groove growth. Mullins has shown that

$$w = 4.6 (Bt)^{1/4} \quad \text{for surface diffusion} \quad (15)$$

$$w = 5.0 (Ct)^{1/3} \quad \text{for volume diffusion} \quad (16)$$

where w is the groove width, t is the annealing time, and B and C are constants at a given temperature.

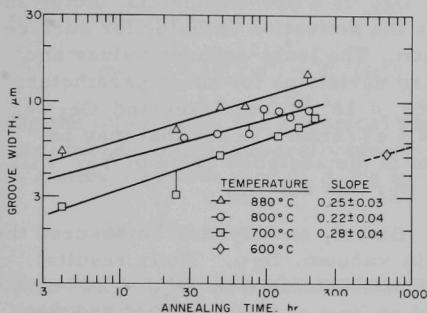


Fig. V-7. Log-Log Plot of the Maximum Groove Width Versus Annealing Time for α -Iron in Liquid Sodium. ANL Neg. No. 308-2408.

agree with the exponent of $1/4$ in Eq. 15. Thus, the groove-growth kinetics suggest a surface-diffusion mechanism for α -iron in a liquid sodium environment.

From the intercepts at 880, 800, and 700°C, as well as from the maximum groove width on the single 600°C specimen, the parameter B was calculated using Eq. 15. Mullins' analysis of grain-boundary grooving showed that

$$B = D_{SL} \nu \gamma_{SL} \Omega^2 / kT \quad (17)$$

where D_{SL} is the diffusion coefficient for transport of solid atoms along the solid-liquid interface, ν is the surface atom concentration of the solid, γ_{SL} is the solid-liquid interfacial tension, Ω is the atomic volume of the

³¹W. W. Mullins, *J. Appl. Phys.* **28**, 333 (1957).

³²W. W. Mullins, *Trans. Met. Soc. AIME* **218**, 354 (1960).

Examination of many grooves on each annealed α -iron surface showed a variability in groove width. To facilitate comparison of grooves on different specimens, the widest groove observed on each specimen was selected for kinetic analysis. The results are shown in Fig. V-7. The data at 880, 800, and 700°C were fitted to a straight line by the method of least squares, with the resulting slopes and their standard deviations shown. At 600°C, only the specimen annealed for the longest time had sufficiently well-developed grooves for width measurement. Within experimental error, the slopes

solid, k is the Boltzmann constant, and T is the absolute temperature. Equation 17 was used to calculate D_{SL} from B . Here it was assumed that the iron surface atom concentration is that of the closest packed (110) plane

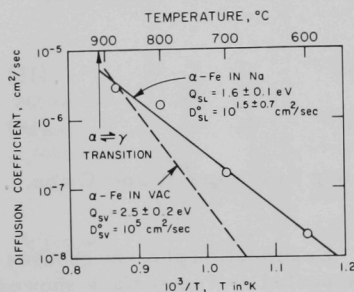


Fig. V-8. Surface Diffusion Coefficient versus Reciprocal Temperature for α -Iron in Liquid Sodium (the dashed line is for α -iron in vacuum, from ref. 33). ANL Neg. No. 308-2407.

with $\nu = 2^{-1/6} \Omega^{-2/3}$. At the temperature of the experiments, $\Omega = 7.8 \times 10^{-24} \text{ cm}^3/\text{atom}$. The interfacial tension is taken to be $\gamma_{SL} = 2000 \text{ erg/cm}^2$. The resulting values of D_{SL} are shown in Fig. V-8. They are fit to an Arrhenius equation

$$D_{SL} = D_{SL}^0 \exp(-Q_{SL}/kT) \quad (18)$$

where D_{SL}^0 is a pre-exponential factor and Q_{SL} is the activation enthalpy for surface diffusion. The least-squares values and standard deviations for these parameters are $D_{SL}^0 = 10^{1.5 \pm 0.7} \text{ cm}^2/\text{sec}$ and $Q_{SL} = 1.6 \pm 0.1 \text{ eV/atom}$. Error that may be present in the assigned value of γ_{SL} will affect D_{SL}^0 but not Q_{SL} .

Blakely and Mykura³³ measured the surface-diffusion coefficient of α -iron in vacuum, D_{SV} . Their results, shown for comparison in Fig. V-7, were characterized by $D_{SV}^0 = 10^5 \text{ cm}^2/\text{sec}$ and $Q_{SV} = 2.5 \pm 0.2 \text{ eV/atom}$, based on $\gamma_{SV} = 2000 \text{ erg/cm}^2$ and the same values of ν and Ω . It can be seen that over nearly all the α -iron range (up to 911°C) surface diffusion is more rapid in a liquid sodium environment than in vacuum. Furthermore, surface diffusion in sodium is found to occur with a lower activation enthalpy than in vacuum.

d. The Simultaneous Determination of Surface and Volume Diffusion Coefficients

Mullins has shown that the time dependence of the width of a grain boundary groove, w , is $t^{1/4}$ for surface diffusion³¹ and $t^{1/3}$ for volume diffusion³² (Eqs. 15 and 16). In many studies an empirical growth law of the form $w \propto t^{1/n}$, where n is a constant and $3 < n < 4$, has been demonstrated, implying the combined action of surface and volume diffusion. Mullins and Shewmon³⁴ developed a theoretical equation for groove growth under the combined mechanisms, where the value of D_v is used in an iterative procedure with the groove-width measurements to calculate the surface diffusion coefficient, D_s . This procedure is not suitable in situations where D_v is unknown. For this case, an alternative method of analysis was first suggested by Chang³⁵ and further developed here which is capable of yielding

³³J. M. Blakely, H. Mykura, *Acta. Met.* **11**, 399 (1963).

³⁴W. W. Mullins and P. G. Shewmon, *Acta. Met.* **7**, 163 (1959).

³⁵R. Chang, *Proceedings of the Conference on Nuclear Applications of Non-fissionable Ceramics*, Washington, D.C., 1966, A. Boltax, ed., p. 101, American Nuclear Society, Hinsdale, Ill.

values of D_s and D_v simultaneously. It is based on a combination of the Mullins and Shewmon equation and the empirical $w \propto t^{1/n}$ growth law.

According to the theory of Mullins,^{31,32} the development of a grain-boundary groove proceeds at the rate $dw/dt = \beta_s/w^3$ for surface diffusion only and $dw/dt = \beta_v/w^2$ for volume diffusion only. If integrated, these equations become $w^4 = 4\beta_s t$ and $w^3 = 3\beta_v t$, or, in more familiar notation, Eqs. 15 and 16, where $4\beta_s = (4.6)^4 B$ and $3\beta_v = (5.0)^3 C$. Mullins has shown that the parameters B and C are functions of temperature given by $B = D_s \gamma \Omega^2 \nu / kT$ and $C = D_v \gamma \Omega / kT$, where γ is the surface tension, Ω is the atomic volume, and ν is the surface atom concentration. According to Mullins and Shewmon, the groove growth rate for the combined action of surface and volume diffusion is the sum of the rates by each mechanism and thus

$$dw/dt = (\beta_s/w^3) + (\beta_v/w^2) \quad (19)$$

On the other hand, the empirical growth law referred to previously, which is deduced from the generally observed linearity of log-log plots of w versus t , yields a growth rate of $d \log w / d \log t = 1/n$, or

$$dw/dt = w/nt \quad (20)$$

Equating the right-hand members of Eqs. 19 and 20 then yields, after rearrangement,

$$w^4/t = n\beta_s + n\beta_v w \quad (21)$$

Equation 21 is thus a hybrid of the existing theoretical and empirical equations for groove growth. The result implies that a plot of w^4/t versus w should be linear with a slope of $n\beta_v$ and an intercept of $n\beta_s$. To calculate β_v and β_s , it is then only necessary to obtain $1/n$ from the slope of a log-log plot of w versus t .

To test this method of analysis of grooving kinetics, it is necessary to employ data for a metal for which D_v is known from independent measurements. Suitable groove-width data were available in N. A. Gjostein's study of the groove development of copper in a hydrogen atmosphere.³⁶ Figure V-9 shows a log-log plot for Gjostein's copper

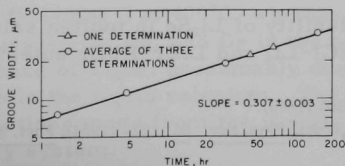


Fig. V-9

Log-Log Plot of Groove Width versus Annealing Time for Copper in Hydrogen at 1020°C (data of Gjostein³⁶). ANL Neg. No. 308-2406.

³⁶N. A. Gjostein, *Trans. AIME* 221, 1039 (1961).

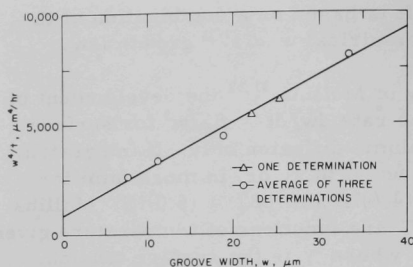


Fig. V-10. Linear Analysis for the Simultaneous Determination of Surface and Volume Diffusion Coefficients for Copper in Hydrogen at 1020°C (data of Gjostein³⁶). ANL Neg. No. 308-2405.

10^{-9} cm²/sec is obtained. Considering the uncertainty in γ , this result compares favorably with existing values (from tracer sectioning experiments) for copper,³⁷⁻⁴¹ which range from 2.7×10^{-9} to 4.0×10^{-9} cm²/sec at 1020°C after correction for correlation effects.⁴²

B. Molten Salt Studies

The physicochemical, thermodynamic, and structural properties of molten salts continue to be of interest. The present program includes study of the complicated behavior of alkali halide-lithium chalcogenide-chalcogen systems using a variety of experimental techniques. This work is of particular interest in view of the energy conversion program discussed in Section V.C of this report. Structure studies, carried out using spectrographic methods, have continued with recent emphasis on phosphorus-chalcogen compounds, iodate ion in nitrate melts, and divalent metal ions in alkali halide melts.

The latter study is of interest to the pyrochemical dechlorination of LMFBR fuels described in Section I.A of this report.

1. Thermodynamics

a. Phase Equilibria of Chalcogen-Containing Systems by Solubility Methods

Measurements of the solubility of Li₂Se in molten salt have been extended to include the LiF-LiCl-LiI and LiBr-RbBr eutectics.

³⁷S. J. Rothman, N. L. Peterson, *Physica Status Solidi*, **35**, 305 (1969).

³⁸A. Kuper, H. Letaw, Jr., L. Slifkin, E. Sonder, C. T. Tomizuka, *Phys. Rev.*, **96**, 1224 (1954); *Phys. Rev.*, **98**, 1870 (1955).

³⁹M. S. Maier, H. R. Nelson, *Trans. AIME*, **147**, 39 (1942).

⁴⁰J. Steigman, W. Shockley, F. C. Nix, *Phys. Rev.*, **56**, 13 (1939).

⁴¹B. V. Rollin, *Phys. Rev.*, **55**, 231 (1939).

⁴²P. G. Shewmon, *Diffusion in Solids*, p. 100, McGraw-Hill Book Co., Inc. (1963).

specimen annealed at 1020°C. From a linear regression analysis, a slope of $1/n = 0.307 \pm 0.003$ is obtained. In Fig. V-10, a plot of w^4/t versus w is shown, and a linear regression analysis provides a slope of $n\beta_v = 210 \pm 7 \mu\text{m}^3/\text{hr}$ and an intercept of $n\beta_s = 870 \pm 140 \mu\text{m}^4/\text{hr}$. From the value of $1/n$, it is found that $\beta_v = 64.5 \pm 2.2 \mu\text{m}^3/\text{hr}$ and $\beta_s = 267 \pm 44 \mu\text{m}^4/\text{hr}$. Thus $C = 3\beta_v/(5.0)^3 = (4.30 \pm 0.15) \times 10^{-16}$ cm³/sec. Finally, with Gjostein's values of $\gamma = 1670$ erg/cm² and $\Omega = 1.18 \times 10^{-23}$ cm³/atom, a volume self-diffusion coefficient of $D_v = CkT/\gamma\Omega = (3.89 \pm 0.13) \times$

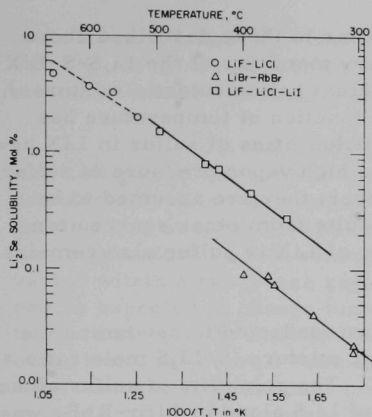


Fig. V-11. Solubilities of Li_2Se in Various Lithium Halide Containing Eutectics. ANL Neg. No. 308-2404.

conducted to determine the effect of the presence of Li_2Se on the solubility of selenium in molten lithium halides. Saturated solutions were prepared of Li_2Se , selenium, and an Li_2Se -selenium mixture ($\text{Se}/\text{Li}_2\text{Se}$ mole ratio = 4.0) in the LiBr-RbBr eutectic at $365 \pm 1^\circ\text{C}$. After each solute was equilibrated with the salt, a portion was filtered and analyzed for selenium content. A substantial increase was noted in the solubility of selenium from the $\text{Li}_2\text{Se-Se}$ mixture (1.5 mol %) when compared with the cases where Li_2Se alone (0.03 mol %) and selenium alone (0.03 mol %) were the solutes. This is presumed to be due to the formation of soluble polyselenides, Se_x^{-n} , where the values of x and n remain to be determined.

Measurements of the solubility of the LiCl-CsCl and LiBr-RbBr eutectics in selenium have been made as a function of the amount of Li_2Se present. After saturation of the selenium with a sample of each salt at $395 \pm 10^\circ\text{C}$, a portion of the selenium phase was filtered and analyzed for the constituent elements of the salt. These experiments were then repeated with Li_2Se added to the salt-selenium mixtures prior to equilibration.

The solubility of halide in selenium was found to be very low (<0.1 mol % at 400°C) whether or not Li_2Se was present. The concentrations of Li , Rb , and Cs in the selenium phase were increased by the presence of Li_2Se , presumably due to the dissolution of Li_2Se , Rb_2Se , and Cs_2Se in the liquid selenium. The latter solubilities are consistent with predictions made from the results of a study of the lithium-selenium binary system.

The recently measured solubilities of Li_2Se are plotted in Fig. V-11 together with previously reported results for the LiF-LiCl eutectic (ANL-7650, p. 43). Results for the all-lithium eutectics lie on a reasonably straight line with a slope corresponding to a heat of solution (ΔH_f°) of 13.3 kcal/mol. The data points for the LiBr-RbBr eutectic lie on a line of nearly the same slope, but displaced significantly to lower solubility values. The presence of a large cation such as Rb^{+1} apparently suppresses the solubility of Se^{-2} ion.

Previously reported values for the solubility of selenium in molten LiF-LiCl-LiI (ANL-7650, p. 43) indicated that very little selenium (<0.1 mol %) dissolves in molten lithium halides in the $350\text{--}500^\circ\text{C}$ range. A study has been con-

Solubility experiments similar to those described above were also conducted on the constituent binary members of the $\text{Li}_2\text{S-S-LiX}$ pseudo-ternary system (LiX represents lithium halide eutectic mixtures). The solubility of Li_2S in LiF-LiCl-LiI as a function of temperature has already been reported (ANL-7650, p. 43). Solubilities of sulfur in LiX have not been measured extensively, owing to the high vapor pressure of sulfur in the temperature region of interest; however, they are assumed to be very low, and preliminary experimental results from other sources tend to support this assumption.⁴³ The solubility of LiX in sulfur also remains to be measured.

A series of experiments was conducted to determine the solubilities of sulfur, Li_2S , and a Li_2S -sulfur mixture ($\text{S/Li}_2\text{S}$ mole ratio = 4.0) in the LiBr-RbBr eutectic at $365 \pm 5^\circ\text{C}$. The solubility of sulfur alone in LiBr-RbBr was only 0.3 mol % and that of Li_2S alone in LiBr-RbBr was 1.5 mol %, but as in the case of the selenium-selenide mixtures, the solubility of the chalcogen increased markedly in the presence of the lithium chalcogenide. The solubilities of the sulfur-sulfide mixtures in LiBr-RbBr (8-10 mol %) were generally higher than those for the selenium-selenide mixtures.

An experiment to determine the solubility of a $\text{Li}_2\text{S-P}_4\text{S}_{10}$ mixture ($\text{P}_4\text{S}_{10}/\text{Li}_2\text{S}$ mole ratio = 0.4) was also conducted. The solubility of P_4S_{10} in LiBr-RbBr in the presence of Li_2S was significantly lower than the solubility of the $\text{Li}_2\text{S-S}$ mixture, and the phosphorus and sulfur were observed to dissolve nearly stoichiometrically. Apparently the sulfide ions, S^{2-} , have more difficulty attaching to the compact P_4S_{10} cages than to the long sulfur chains in elemental molten sulfur.

b. Phase Diagrams of Pseudo-Ternary Lithium Selenide-Selenium-Alkali Halide Systems

Investigation of these pseudo-ternary systems was undertaken to resolve apparent discrepancies between the lithium-selenium phase diagram (see Section V.A.1) and results of the emf studies reported in the next subsection (see also ANL-7650, p. 42). The original assumption that the cathode of the emf cell could be considered to be a simple binary lithium-selenium mixture was also brought into question by the results of the solubility studies presented in the preceding subsection. The emf results were, therefore, interpreted in terms of a cathode mixture in which a pseudo-ternary system existed composed of the cell product (lithium selenide), the pure cathode material (selenium), and the molten salt electrolyte (alkali halide eutectic mixtures). The electrolytes considered are the eutectic mixtures 59 mol % LiBr -41 mol % RbBr , which melts at 276°C ,

⁴³D. M. Gruen (Chemistry Division) has indicated that the solubility of sulfur in LiCl-KCl is extremely low based on results of absorption spectral studies.

and 11.7 mol % LiF-29.1 mol % LiCl-59.2 mol % LiI, which melts at 340.1°C. It is assumed in describing the ternary systems that the eutectic mixtures behave essentially as single components.

Having concluded that the behavior of the cathode of the emf cell can be interpreted in terms of a pseudo-ternary system, phase boundaries within that system can be located by examining the behavior of the cell emf as a function of composition and temperature. If, for example, the temperature is held constant and the overall cathode composition is varied within a two-phase region, then the composition of the two phases can be expected to change (unless the changing overall composition happens to move along a tie line) and hence the cell emf will change. If, on the other hand, the overall composition lies in a three-phase region, changing the composition at constant temperature will merely alter the relative amounts of the three phases present, but will not alter their compositions, and the emf must remain constant. Thus in a constant-temperature plot of emf versus cathode composition, phase boundaries are identified by discontinuities in slope. Such a plot is shown in Fig. V-12. Details of the emf measurements are presented in the next subsection. It can be seen that discontinuities in slope occur at 18.8, 28 and 32 mol % lithium. The cathode composition can be represented in several equivalent ways since the quantities of alkali halide eutectic and selenium in the cell cathode, which are determined by the cell design and the amounts of selenium and electrolyte placed in the cell, do not change during cell operation. In Fig. V-12, the percent Li is based on the ratio of the moles of Li in the cathode to the sum of moles of Li plus moles of Se, exclusive of the lithium in the alkali halide electrolyte. Similar plots can be made using data obtained from cells with different relative amounts of selenium and alkali halide eutectic in the cathode. The phase-boundary information obtained in this way is plotted for the system $\text{Li}_2\text{Se}-\text{Se}-(\text{LiBr}-\text{RbBr})$ in Fig. V-13 and for the system $\text{Li}_2\text{Se}-\text{Se}-(\text{LiF}-\text{LiCl}-\text{LiI})$ in Fig. V-14.

Before considering further the pseudo-ternary systems, it is necessary to review what is known or presumed concerning the binary

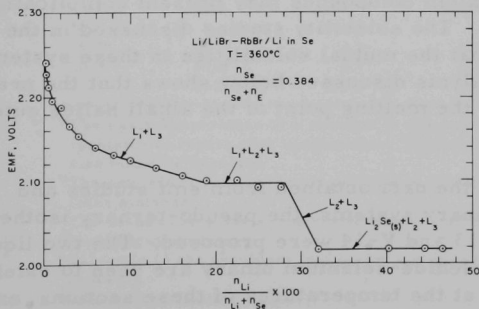


Fig. V-12

Emf as Function of Temperature for
Li/LiBr-RbBr/Li in Se Cell. ANL
Neg. No. 308-2403.

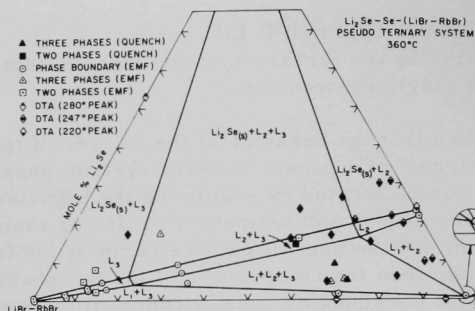
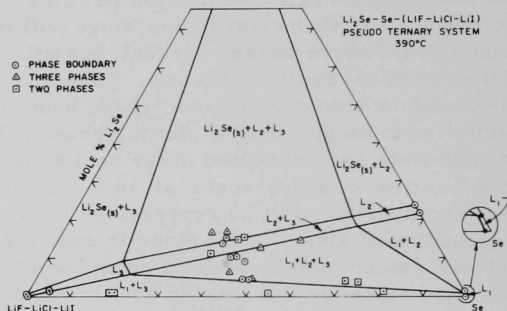


Fig. V-13

$\text{Li}_2\text{Se}-\text{Se}-(\text{LiBr}-\text{RbBr})$ Pseudo-Ternary System at 360°C . ANL Neg. No. 308-2402.

Fig. V-14

$\text{Li}_2\text{Se}-\text{Se}-(\text{LiF}-\text{LiCl}-\text{LiI})$ Pseudo-Ternary System at 390°C . ANL Neg. No. 308-2401.



and pseudo-binary systems involved. The lithium selenide-selenium binary system is known from the work on the lithium-selenium system discussed in Section V.A.1. This system has a simple monotectic structure with a monotectic temperature of 350°C and a miscibility gap extending from below 0.4 mol % Li_2Se to 22 mol % Li_2Se . The selenium-rich liquid L_1 freezes at 220°C , the freezing point of pure selenium. The relatively lithium-rich liquid, L_2 , exists between the upper liquidus and the immiscibility boundary, both of which rise steeply. Less is known about the selenium-alkali halide systems. Presumably they have no intermediate phases, although rubidium-selenium compounds may present complications for the $\text{Se}-(\text{LiBr}-\text{RbBr})$ system. The solubility studies discussed in the preceding subsection indicate that the mutual solubilities in these systems are quite low. The thermal analysis discussed below shows that the presence of selenium does not alter the melting point of the alkali halide eutectics and vice versa.

On the basis of the data obtained from emf studies and from what is known about the binary systems, the pseudo-ternary isothermal sections shown in Figs. V-13 and V-14 were proposed. The two liquid phases present in the lithium selenide-selenium binary are seen to extend into the ternary phase diagram at the temperatures of these sections, and

the designations L_1 and L_2 are retained. The alkali halide-rich liquid, L_3 , also extends into the ternary diagram. The region of three-liquid equilibrium is a particularly interesting feature of this system.

To further characterize these systems, a series of differential thermal analysis (DTA) curves was obtained for the pseudo-ternary system containing LiBr-RbBr. The results are given in Table V-4; the compositions of the samples investigated are also indicated on Fig. V-13. It can be seen that there are three thermal peaks observed at about 280, 247, and 220°C. These are associated with the disappearance of L_3 , L_2 , and L_1 , respectively. According to this interpretation, there would be four four-phase equilibria or thermal invariants, two of which occur very close to pure LiBr-RbBr and are essentially isothermal. These thermal data are entirely consistent with the proposed pseudo-ternary system. The thermal data can provide a qualitative idea as to the range of compositions covered by L_2 and L_3 . For compositions lying near the lithium selenide-selenium binary, the peak associated with the disappearance of L_3 is not observed.

TABLE V-4. Summary of DTA Data on Se, Li_2Se , LiBr-RbBr Eutectic, and Their Binary and Ternary Mixtures

Composition (mol %)			Peak Temperatures of Endothermic Effects Noted ^a (°C)		
Li_2Se	Se	Eutectic			
100					1302 ^b
	100		221		
		100		280	
23.4	76.6		223		358 ^c
16.2	60.3	23.5	221 ^d	247	275
22.1	71.4	6.5	221	245	(267) ^e 350 ^f
	70.0	30.0	221		283
	93.0	7.0	221		284
10.0	85.0	5.0	222	247	(270) ^e
20.0	75.0	5.0	222	246	(270) ^e
30.0	65.0	5.0	221	244	(260) ^e
6.0	80.5	13.5	222	247	277
14.9	69.8	15.3	221 ^d	247	280
21.2	63.8	15.0	225 ^d	246	(263) ^e
26.2	58.7	15.1	221 ^d	247	282
4.7	65.8	29.5	222	247	277
16.0	51.8	32.2	222	247	276
22.8	50.1	27.1	228	247	272
52.4		47.6			278
10.7	86.8	2.4	222	248	(274) ^e 350 ^f
30.4	67.5	2.1	223	246	
17.4	14.2	68.4	222	245	274

^aThe exact temperature of a reaction is difficult to determine using DTA. Here we consistently report peak temperature. Uncertainties of $\pm 2^\circ\text{C}$ due to changing peak size might be expected.

^bThe only effect seen is the mp of Li_2Se at 1302°C. This value is confirmed by other methods.

^cThe Li-Se binary has a monotectic reaction at 350°C.

^dPeak shows doubling.

^eValues in () are shoulders (not peaks) and may be associated with a liquidus crossing.

^fSeen on first heating only.

This would seem to indicate that L_2 extends far enough into the phase diagram to prevent formation of L_3 from these compositions.

An effort has been made to determine the degree to which L_2 and L_3 extend into the phase diagram by equilibration of samples having compositions lying within the three-liquid region followed by separation of the phases for chemical analyses after quenching. To date these efforts have failed since, despite rapid separation of L_1 , L_2 and L_3 do not separate completely. Microscopic examination of the quenched samples shows that there are indeed two phases present in addition to L_1 , but their densities are apparently quite similar. Other quenched samples having compositions in the two-liquid region between L_2 and L_3 have been examined and have been found to contain two phases, as expected. It seems likely that the consolute temperature of the miscibility gap between L_2 and L_3 is not very high, probably below 500°C.

Fewer supplemental supporting data are available for the pseudo-ternary system involving the LiF-LiCl-LiI eutectic. Qualitatively, at least, it does not seem to differ greatly from the systems involving the LiBr-RbBr eutectic since the emf data show very similar behavior.

c. Thermodynamics of Pseudo-Ternary Lithium Selenide-Selenium-Alkali Halide Systems by Emf Methods

As explained in Section B.1.b above, it has been found that fused lithium halide-containing electrolytes and lithium-selenium mixtures of certain compositions show significant solubilities in each other. This makes it necessary to include the influence of the electrolytes on the behavior of emf (and other) cells using these combinations of electrolytes and cathodes. This influence has been taken into account by considering the electrolyte mixture to be a single component in the pseudo-ternary lithium selenide-selenium-electrolyte system.

The experiments were performed in two ways: (1) The effect of temperature (280-525°C) on emf was studied for various cathode alloy compositions. (2) The effect of lithium-selenium alloy composition on emf was studied for a given temperature. Two electrolytes were used in the cells: 59 mol % LiBr-41 mol % RbBr (mp = 278°C) and 11.7 mol % LiF-29.1 mol % LiCl-59.2 mol % LiBr (mp = 341.9°C). The emf readings for a given temperature and composition with the same cell were reproducible within 3 mV; readings from cell to cell were reproducible within about 5 mV.

Typical results for emf as a function of temperature for various lithium-to-selenium mole ratios are shown in Fig. V-15. The data points for the lines marked 10.0 to 27.62 are too numerous and too closely spaced to be shown. Note that all of the data in this figure were taken

from a cell using the LiBr-RbBr eutectic electrolyte, with a given selenium-to-electrolyte ratio in the selenium compartment $[n_{\text{Se}}/(n_{\text{Se}} + n_{\text{E}}) = 0.384]$. Three general types of behavior can be noted in Fig. V-15. (1) For lithium contents below about 19 mol %, i.e., $[n_{\text{Li}}/(n_{\text{Li}} + n_{\text{Se}})] \times 100 < 19.0$, $\partial E/\partial T$ is positive and $\partial E/\partial \ln x_{\text{Li}} = RT/2F$. (2) In the range ~19 to ~28 mol % Li, $\partial E/\partial T \approx 0$; $\partial E/\partial \ln x_{\text{Li}} \approx 0$. (3) For lithium contents of 32 to at least 46.4 mol %, $\partial E/\partial T$ is negative and $\partial E/\partial \ln x_{\text{Li}} = 0$. Figure V-12 shows these three regions in terms of an emf-vs-composition plot for a temperature of 360°C and introduces a fourth region between 28 and 32 mol % Li in Se. These four regions can be understood on the basis of the pseudo-ternary phase diagram shown in Fig. V-13.

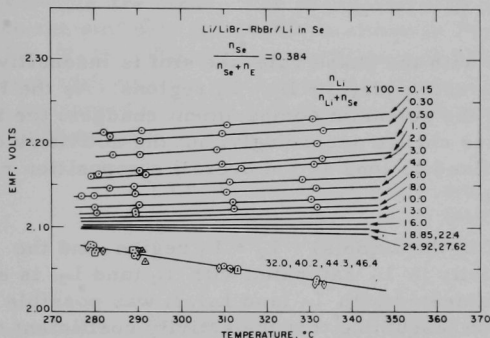


Fig. V-15

Emf Measurements of the Li/LiBr-RbBr/Li in Se Cell. ANL Neg. No. 308-2400.

The results shown in Fig. V-15 correspond to a line in Fig. V-13 drawn parallel to the Li_2Se -Se side of the diagram, but located at 38.4% of the distance between the LiBr-RbBr corner and the Li_2Se -Se side. The discontinuous change of slope at 18.8% in Li in Fig. V-15 corresponds to the point located at 4.4% Li_2Se , 33.9% Se, and 61.7% LiBr-RbBr in Fig. V-13. This is the location of the phase boundary between the regions labeled $L_1 + L_3$ and $L_1 + L_2 + L_3$ on the two figures. In this manner, the phase boundaries shown in Fig. V-13 were located from the emf results and were found to be consistent with the results of the thermal analyses and other results discussed in Section V.B.1.

It can be seen from Fig. V-13 that liquid L_1 is selenium containing small concentrations of salt (<0.02 mol %) and lithium (<0.5 mol %); liquid L_2 is a lithium-selenium-salt mixture containing (at 360°C) the equivalent of 16-23 mol % Li_2Se and up to several percent salt; liquid L_3 is the salt-rich phase containing up to about 6 mol % Li_2Se and up to about 21 mol % Se (at 360°C). In all two-phase regions, the emf is a function of composition (except along tie-lines).

In the case of the $L_1 + L_3$ region, it is found from data such as those in Fig. V-12 that $\partial E/\partial \ln x_{\text{Li}} = RT/2F$, indicating that two electrons and two lithium atoms are involved in the overall cell reaction, which may be written



The corresponding Nernst equation (with pure lithium as the reference electrode) is then

$$E = -\frac{RT}{2F} \ln \gamma_{\text{Li}} x_{\text{Li}} \quad (23)$$

The activity coefficient of lithium in liquid L_1 has been calculated from Eq. 22 and the results from $\text{Li}/\text{LiBr}-\text{RbBr}/\text{Li}$ in Se cells at 360°C . The activity coefficient is found to be 3×10^{-15} and is insensitive to composition over the range from $n_{\text{Li}}/(n_{\text{Li}} + n_{\text{Se}}) \times 100 = 0.2 \text{ mol } \%$ to saturation of L_1 , which can be as high as $20 \text{ mol } \%$.

In accordance with the phase rule, the emf is insensitive to composition in the $\text{L}_1 + \text{L}_2 + \text{L}_3$ and $\text{Li}_2\text{Se}(\text{s}) + \text{L}_2 + \text{L}_3$ regions. As the lithium (or electrolyte) content of the selenium compartment changes, the relative amounts of the three phases change accordingly, but the activities of the three components remain fixed as long as the overall composition remains in a three-phase region.

From the emf in the $\text{Li}_2\text{Se}(\text{s}) + \text{L}_2 + \text{L}_3$ region, and the knowledge that the lithium activity in L_1 saturated with L_2 (and L_3) is equal to the lithium activity in L_2 saturated with L_1 (and L_3), it was possible to apply the Gibbs-Duhem equation (assuming that the activity coefficient of salt in L_2 and L_3 was constant) in correcting the free energy of formation of Li_2Se to unit activities of lithium and selenium. At 360°C , $\Delta G_f^\circ(\text{Li}_2\text{Se}, \text{s}) = -94.0 \text{ kcal/mol}$.

Experiments similar to those described above were also performed with the $\text{LiF}-\text{LiCl}-\text{LiI}$ eutectic as the electrolyte. Typical emf-vs-temperature and emf-vs-composition curves are shown in Figs. V-16 and V-17. The resemblances to the corresponding figures with the bromide

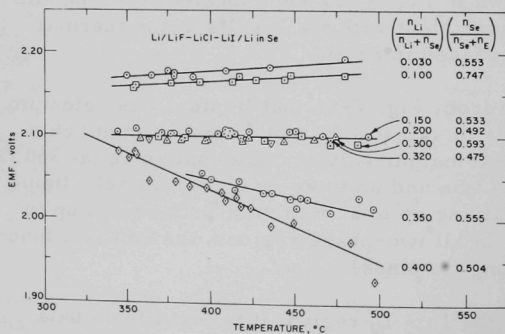


Fig. V-16

Emf Measurements as a Function of Temperature for $\text{Li}/\text{LiF}-\text{LiCl}-\text{LiI}/\text{Li}$ in Se Cell. ANL Neg. No. 308-2399.

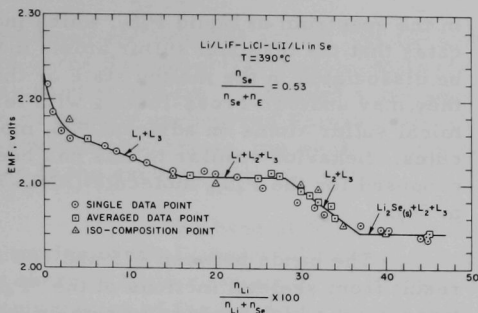


Fig. V-17

Emf Measurements as a Function of Composition for Li/LiF-LiCl-LiI/Li in Se Cell. ANL Neg. No. 308-2398.

electrolyte are clear. The pseudo-ternary phase diagram, constructed from the emf data for 390°C, is shown in Fig. V-14, and is similar to that of Fig. V-13. The activity coefficient of lithium in liquid L_1 and the free energy of formation of $\text{Li}_2\text{Se}(s)$ were calculated from the emf results and are presented in Table V-5 together with the values from the bromide electrolyte cell.

TABLE V-5. Thermodynamic Results from Li/LiX/Li in Se Emf Cells

Electrolyte	γ_{Li} in L_1 , 360°C	$\Delta G_f(\text{Li}_2\text{Se}, s)$, 360°C (kcal/mol)
LiBr-RbBr	3×10^{-15}	-94.0
LiF-LiCl-LiI	3×10^{-15}	-94.5

2. Structure Investigations by Spectroscopic Methods

a. Spectra of P_4S_7 and P_4Se_3

Two phosphorus-chalcogen compounds, P_4S_7 and P_4Se_3 , under investigation as cathode reactants for electrochemical cells, have been studied by Raman spectroscopy. The spectra of solid and liquid P_4S_7 are shown in Figs. V-18a and V-18b. The bands in the liquid spectrum are broad and poorly resolved compared with those in the solid spectrum. However, the peak frequencies of the principal bands and their relative intensities are nearly the same for the two spectra in the region from 450 to 100 cm^{-1} .

In P_4S_7 , five of the sulfur atoms are present in P-S-P bridges, and two of the sulfur atoms are in terminal P-S bonds. The bands at 663 and 667 cm^{-1} in the spectrum of the solid are the two stretching modes expected for the terminal P-S bonds. These bands are not observed

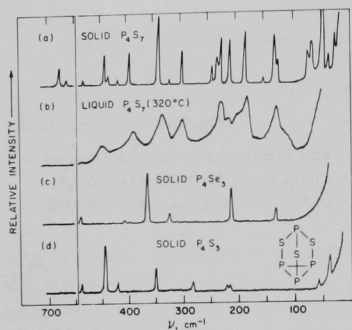


Fig. V-18. Raman Spectra of P_4S_7 , P_4Se_3 , and P_4S_3 . ANL Neg. No. 308-2397.

in the spectrum of liquid P_4S_7 , which indicates that the terminal sulfur atoms may be dissociated in the molten state or that they may undergo cross-linking with terminal sulfur atoms on adjacent P_4S_7 molecules. Behavior similar to this has been proposed for the P_4S_{10} molecule (ANL-7650, p. 50).

The bands between 475 and 100 cm^{-1} result from skeletal motions of the " P_4S_5 " inner cage, which appears to remain intact in the liquid state. Frequencies below 100 cm^{-1} for the solid are either lattice modes or low-frequency skeletal modes.

The Raman spectrum of solid P_4Se_3 is shown in Fig. V-18c and the spectrum of solid P_4S_3 in Fig. V-18d for comparison. The spectral frequencies and relative intensities are listed in Table V-6 along with results of a previous Raman study of P_4Se_3 in CS_2 solution by Irgolic et al.⁴⁴ The band observed at 601 cm^{-1} in the CS_2 solution was probably due to unreacted phosphorus in their sample (ν_1 for P_4 was reported by Pistorius⁴⁵ to be at 606 cm^{-1}). The Raman data for solid P_4S_3 are in good agreement with previously reported results of Gerding, Maarsen, and Nobel.⁴⁶

TABLE V-6. Raman Frequencies (cm^{-1}) for P_4X_3 ($X = \text{Se}, \text{S}$)^a

P_4Se_3		P_4S_3	Assignment
CS_2 Solutions ^b	Solid ^c	Solid ^c	
601	-	-	P_4
-	481 (10)	484 (19)	P_4X_3
-	405 (2)	-	$P_4X_3(?)$
363	363 (100)	441 (100)	P_4X_3
317	322 (14)	418 (20)	P_4X_3
214	215 (53)	342 (60)	P_4X_3
-	133 (24)	285 (21)	P_4X_3
-	-	227, 220 (9)	P_4X_3
-	-	57 (13)	lattice mode
-	-	34 (47)	lattice mode

^aNumbers in parentheses indicate relative intensity.

^bIrgolic et al.

^cThis work.

P_4Se_3 , like P_4S_3 , has the cage structure shown as an insert in Fig. V-18d. For this structure with C_{3v} point-group symmetry, ten frequencies are expected: four A_1 , one A_2 , and five E. The A_1 and E modes

⁴⁴K. Irgolic, R. A. Zingaro, M. Kudchadker, *Inorg. Chem.* **4**, 1421 (1965).

⁴⁵C. W. F. T. Pistorius, *J. Chem. Phys.* **29**, 1421 (1958).

⁴⁶H. Gerding, J. W. Maarsen, P. C. Nobel, *Rec. trav. chim.* **76**, 757 (1957).

are Raman and infrared active, and the A_2 mode is infrared active only. Five of the Raman-active fundamentals for P_4Se_3 , and possibly a sixth (if the weak band at 405 cm^{-1} is indeed a genuine vibration of P_4Se_3), are observed. The remaining unobserved Raman bands may be coincident with some of the observed fundamentals, too weak in intensity to be detected or at frequencies close to the exciting line.

The band at 481 cm^{-1} is attributed to the symmetric stretching motion of the P_3 base. This band occurs at 484 cm^{-1} for P_4S_3 , indicating that there is little coupling of the bridging chalcogen motions with the symmetric motion of the P_3 base. Irgolic et al. have assigned the most intense band in the spectrum, 363 cm^{-1} , to the symmetric stretch of the apex phosphorus atom. The corresponding vibration in P_4S_3 is shifted to higher frequency (441 cm^{-1}), as expected, due to the lighter sulfur atoms. An attempt is made in Table V-6 to correlate the remaining P_4Se_3 bands with P_4S_3 bands on the basis of relative intensities, but specific assignments for these vibrations must await a complete normal coordinate analysis.

b. Iodate Spectrum

An investigation of the Raman spectrum of the iodate ion, IO_3^{-1} , dissolved in molten nitrates, has been carried out as part of a program to study reactions of elemental iodine and iodine-containing species with fused nitrates. The reaction of elemental iodine with silver nitrate at 200°C is of particular interest because of its role in the silver nitrate scrubber towers used to remove ^{131}I from the gases released during the reprocessing of nuclear fuels.⁴⁷ The iodate ion was selected for investigation because it is one of the major reaction products formed when I_2 is contacted with a molten nitrate. We have also found the I_2O_5 reacts with molten nitrates to produce IO_3^{-1} .

Melts containing iodate dissolved in molten nitrate were prepared by heating 15 mol % I_2O_5 -85 mol % MNO_3 mixtures ($M = \text{Li, Na, K, Rb, Cs, Ag, and Tl}$) for several hours at or near the melting point of the nitrate. Raman spectral results for the entire series of experiments are presented in Table V-7. The frequencies of the nitrate peaks for the various cations are in good agreement with previously published spectra.⁴⁸ Three Raman bands that could be attributed to IO_3^{-1} were observed for all of the cations. The strong band in the $770\text{--}810\text{ cm}^{-1}$ region was polarized in all cases, and the lowest frequency band in the $290\text{--}340\text{ cm}^{-1}$ region was depolarized in all cases. The shoulder in the $340\text{--}380\text{ cm}^{-1}$ region appeared to be partially polarized in some of the spectra. For the cations Cs^{+1} , Ag^{+1} , and Tl^{+1} , a weak depolarized band was observed near 820 cm^{-1} that may also be due to IO_3^{-1} . However, the normally Raman-inactive A_2 mode of NO_3^{-1} has been observed in Raman spectra of molten $AgNO_3$ and $TlNO_3$ near 820 cm^{-1} .⁴⁸

⁴⁷W. A. Rodger, S. L. Reese, Reactor Fuel-Process. Technol. 12(2), 173 (1969).

⁴⁸S. C. Wait, Jr., A. T. Ward, G. J. Janz, J. Chem. Phys. 45, 133 (1966).

TABLE V-7. Raman Data for Molten $\text{MIO}_3\text{-MNO}_3$ Mixtures

Composition	Temp. (°C)	Iodate Vibrations				Nitrate Vibrations	
		ν_3	ν_1	ν_2	ν_4	ν_1	ν_4
15 mol % $\text{I}_2\text{O}_5\text{-LiNO}_3$	280	-	807	344	290	1061	719
15 mol % $\text{I}_2\text{O}_5\text{-NaNO}_3$	300	-	795	366	323	1053	718
	340						
15 mol % $\text{I}_2\text{O}_5\text{-KNO}_3$	450	-	793	351	318	1046	717
15 mol % $\text{I}_2\text{O}_5\text{-RbNO}_3$	470	-	793	361	315	1045	712
15 mol % $\text{I}_2\text{O}_5\text{-CsNO}_3$	455	822	786	350	308	1042	712
12 mol % $\text{I}_2\text{O}_5\text{-AgNO}_3$	175	822	776	383	342	1039	729
18 mol % $\text{I}_2\text{O}_5\text{-TlNO}_3$	300	817	773	348	308	1033	708

The observed spectra for IO_3^{-1} are most consistent with a pyramidal structure having C_{3v} symmetry. We believe that for most of the cations the antisymmetric stretching mode $\nu_3(\text{E})$ is buried under the symmetric stretching mode, $\nu_1(\text{A}_1)$, in the $770\text{-}810\text{ cm}^{-1}$ region. This observation is not unprecedented for iodates. Dureg, Bonner, and Breazeale⁴⁹ were able to resolve ν_1 and ν_3 in solid NaIO_3 , but found that in concentrated aqueous solutions of NaIO_3 , the two vibrations merged into one symmetrically shaped band.

The effect of changing the cation on the symmetric stretching vibration of each of the anions is similar. Both ν_1 frequencies are observed to shift steadily to lower frequencies with the cation sequence Li, Na, K, Rb, Cs, Ag, and Tl, which indicates in a qualitative way that the cation polarization effects on IO_3^{-1} and NO_3^{-1} are similar.

c. Divalent Metal Ion Spectra

Raman studies of divalent metal ions in molten-halide media have continued with investigations of the $\text{ZnI}_2\text{-LiCl-KCl}$ system and a reinvestigation of the $\text{MgCl}_2\text{-KCl}$ system. Raman spectra of molten samples containing 5 mol % ZnI_2 in LiCl-KCl and 5 mol % ZnCl_2 in LiCl-KCl were identical, indicating that in chloride melts containing zinc (II) and low levels of iodide, the zinc (II) is almost exclusively tied up in chloride complexes. The spectra are most consistent with the presence of ZnCl_4^{-2} ; however, due to the low levels of zinc (II), all of the expected vibrations for ZnCl_4^{-2} were not observed. These studies have helped in understanding the high ZnI_2 removal efficiency of the LiCl-KCl cover salt used in the liquid zinc decladding process (see Section I.D of this report).

The fact that very little if any of the ZnI_2 dissolving in the cover salt remains intact explains the low vapor pressure of ZnI_2 in the

⁴⁹J. R. Dureg, O. D. Bonner, W. H. Breazeale, *J. Phys. Chem.* **69**, 3886 (1965).

system even at temperatures near the melting point of liquid zinc. (Raman spectra of $\text{ZnI}_2\text{-LiCl-KCl}$ samples generated in the decladding process have been identical to samples of the same composition prepared by the addition of ZnI_2 to LiCl-KCl .)

The complete Raman spectrum of MgCl_4^{2-} has been obtained using the 5145 Å line of a Coherent Radiation Laboratories MG-52 mixed-gas (argon-krypton) ion laser for excitation. Bands are observed at $325 \pm 5 \text{ cm}^{-1}$ (depolarized), $250 \pm 2 \text{ cm}^{-1}$ (polarized), $120 \pm 5 \text{ cm}^{-1}$ (depolarized), and $94 \pm 5 \text{ cm}^{-1}$ (depolarized). The four-band Raman spectrum, one band polarized and three bands depolarized, is characteristic of a five-atom tetrahedral species. The following assignments for MgCl_4^{2-} under the point group T_d can now be made: $\nu_1(A_1) = 250 \text{ cm}^{-1}$, $\nu_2(E) = 94 \text{ cm}^{-1}$, $\nu_3(T_2) = 325 \text{ cm}^{-1}$, and $\nu_4(T_2) = 120 \text{ cm}^{-1}$. This study confirms an earlier conclusion that the principal monomeric species in $\text{MgCl}_2\text{-KCl}$ melts is MgCl_4^{2-} (ANL-7650, p. 51). It is now possible to make a complete normal-coordinate analysis for tetrahedral MgCl_4^{2-} . This analysis is in progress.

C. Energy Conversion

1. High-Specific-Energy Lithium/Selenium Batteries for Implantation

A program has been undertaken by the Chemical Engineering Division of Argonne National Laboratory under the Medical Devices Applications Program of the National Heart and Lung Institute to develop a lithium/selenium battery suitable for use as an implantable, rechargeable power source for an artificial heart or heart-assist device. For this application, the critical measures of performance are the specific energy (W-hr/kg), the energy density (W-hr/cm³), and the cycle life (number of charge-discharge cycles before failure). The specific power (W/kg) objective is less critical, with a total power of 10-30 W required for an electrically driven heart-pump system. The specific energy requirement is in the vicinity of 100 W-hr/kg, which would permit operation of an artificial heart for 10 hr with a battery weight of 1 kg if the average power demand were 10 W. The battery is to be recharged by transmitting electromagnetic energy through the skin.

In the first year's effort on this program, the major emphasis was on cell design, including the development of suitable paste electrolytes, sealants, insulators, current collectors, and housings for the anode and cathode. Eighteen 7.5-cm dia cells were constructed, subjected to electrical performance tests, and examined after disassembly. Two batteries of 7.5-cm dia cells were built and tested. The first battery was unsealed and contained five cells. The second one contained six cells and was hermetically sealed from the environment.

a. Single-Cell Studies

The development of reliable single cells is an essential step in achieving a successful battery. Consequently, much of the effort has been directed toward the construction and testing of experimental cells. Eighteen single cells, approximately 7.5 cm in diameter with an active electrode area of about 32 cm², have been built and subjected to electrical performance tests.

(1) Cell Design

Cell design has undergone a process of evolution with several design improvements being adopted during the course of the eighteen single-cell tests. A schematic diagram of a recent cell design is given in Fig. V-19. The anode and cathode

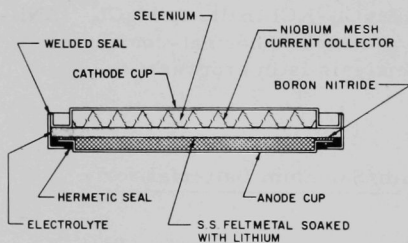


Fig. V-19. Single-Cell Design for an Implantable Battery. ANL Neg. No. 308-2220.

some of the cells, concentric grooves were machined in the lip of the cup, where it bears against the paste-electrolyte disk, to effect a seal. This technique proved especially useful in sealing the liquid selenium within the cathode cup.

Most of the paste-electrolyte disks consisted of 60 wt % LiF-LiCl-LiI electrolyte (a eutectic mixture of 11.7 mol % LiF, 29.1 mol % LiCl, and 59.2 mol % LiI; mp 340.9°C) and 40 wt % α -LiAlO₂ filler. They were pressed at temperatures ranging from room temperature to 200°C with a force of about 1,200 kg/cm². Some of the disks were coated with a low-melting salt mixture in an effort to decrease or eliminate permeation by selenium.

The cells were assembled by the following general procedure. Liquid lithium metal was soaked into the stainless steel Feltmetal⁵¹ anode current collector at 500-600°C, this temperature being

⁵⁰A registered name of a product of the Westinghouse Electric Corporation with the approximate composition (wt %): Fe, 53.7; Ni, 29.0; Co, 17.0; Mn, 0.3.

⁵¹Trade name of a product of the Huyck Metals Company with a porosity of 80 to 87% and a mean pore diameter of 0.02 cm.

required to achieve satisfactory wetting. In some of the cells, a small amount of the molten-salt electrolyte was added to the lithium to promote wetting of the paste electrolyte by the lithium. The cathode was prepared by melting selenium (mp, 220°C) into a corrugated niobium expanded-mesh cathode current collector within the cathode cup. This design was used to obtain a light-weight, relatively open structure that would promote convection and diffusion within the cathode. The assembled test cells were held under a compressive force by clamping or by tack-welding the peripheral ring to the cathode cup.

(2) Electrical Performance Results

The results of the cell performance tests are summarized in Table V-8. The early cells were operated primarily to gain experience in the assembly and testing of full-size (7.5-cm dia) cells. A cell design incorporating a corrugated niobium-mesh cathode current collector was tested in Cell No. 7 in which the paste-electrolyte disk was coated with a low-melting salt mixture (LiCl-LiI-KI, mp 260.5°C), and the cell was oriented vertically⁵² during the test. The voltage-capacity density curve is shown in Fig. V-20. The capacity density, 0.64 A-hr/cm², was the

TABLE V-8. Electrical Performance of Experimental Cells

Cell No.	Operating Temp. (°C)	Total Duration of Test (hr)	Theoretical Capacity Density (A-hr/cm ²)	Maximum Capacity Density Achieved (A-hr/cm ²)	Initial Open-Circuit Voltage (V)	Average Voltage (V)	Current Density (A/cm ²)	Short-Circuit Current Density (A/cm ²)	Purpose of Experiment
1	375-400	~2	0.64	0.002	2.3	0.6	0.02	0.032	Test first 7.5-cm dia cell design; Li uppermost.
2	385	24	0.64	0.098	2.1	0.6	0.01	0.021	Test modified Nb mesh current collector; Li uppermost.
3	385	43	1.32	0.23	2.16	1.5	0.02	0.095	Test stainless steel Feltmetal current collector; Li uppermost.
4	385	48	0.71	0.13	2.16	1.0	0.04	0.4	Test modified cell design (grooved cathode cup lip); Li uppermost.
5	375	20	0.65	0.32	2.12	1.7	0.04	0.5	Test Se-uppermost orientation.
6	350	138 ^a	0.65	0.30	2.12	1.8	0.04	0.5	Test Se-uppermost orientation.
7	~365	72	1.04	0.64	2.3	1.6	0.04	0.25	Test modified cell design (corrugated current collector); vertical orientation.
8	~375	~16	0.51	0.08	1.9	0.94	0.04	0.05	Test modified cell design (polyimide composite insulator); Se uppermost.
9	~375	~16	0.50	0.08	2.1	1.2	0.04	0.76	Test modified cell design (polyimide composite insulator); Se uppermost.
10	380	24	1.04	0.25	2.25	1.8	0.04	0.25	Test cell with BN insulator and coated paste; vertical.
11	375	7	0.58	0.29	1.9	1.5	0.04	0.35	Test cell with cast-in-place electrolyte; Se uppermost.
12	365	7	1.04	0.29	2.25	1.75	0.04	0.45	Test modified cell design; vertical.
13	370	14	1.04	0.25	2.30	1.82	0.04	0.5	Test modified cell design; Se uppermost.
14	370	24	1.04	0.025	2.2	1.98	0.004	0.04	Test 50 wt % electrolyte-50 wt % filler paste; vertical.
15	375	3	1.04	0	1.1	0	0	0	Test sealed cell; vertical.
16	360	2	0.97	0.082	2.1	1.4	0.04	0.32	Test modified cell design; vertical.
17	380	2	0.97	0.082	2.2	1.7	0.04	0.13	Test modified cell design; vertical.
18	380	35	0.53	0.37	2.2	1.5	0.036	0.32	Test modified cell design with BN insulator; vertical.

^aIncludes 105 hr on open circuit.

⁵²The plane of the electrolyte disk was oriented vertically.

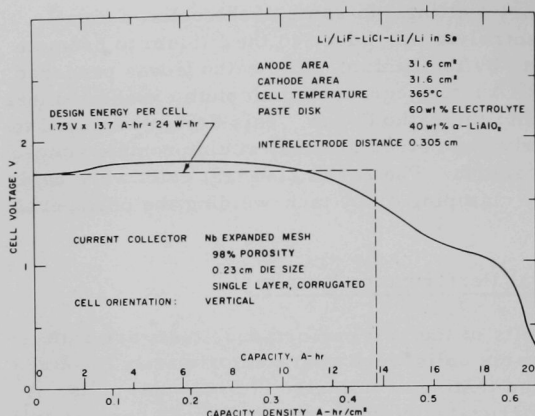


Fig. V-20

Voltage-Capacity Density Characteristics for Cell No. 7. ANL Neg. No. 308-2218 Corr.

highest observed in any of the single-cell tests. The electrical performance of Cell No. 7 on one discharge was sufficient to meet the requirements of a 120 W-hr, 10-W battery of five 7.5-cm-dia cells.

Cells No. 8, 9, and 11 were of a design that employed a polyimide- LiAlO_2 composite insulator in the anode cup. The highest short-circuit current density, 0.76 A/cm^2 , was achieved with Cell No. 9. Cell No. 11 was the only one tested in which the paste electrolyte was cast in place within the cell. A relatively high percentage (50%) of the theoretical capacity density was achieved, suggesting that the cast-in-place electrolyte might be investigated further.

Cell No. 10 was similar to Cell No. 7, except that a boron nitride ring was used in place of a polyimide gasket as an electrical insulator between the anode cup and the electrolyte. The cell was discharged and charged in 6-hr cycles. During the first 6-hr discharge at 0.04 A/cm^2 , the cell voltage remained constant at 1.92 V. The IR loss during this period was 0.16 V, or about 47% of the total overvoltage. In the following 6-hr period, while on automatic charge, the cell became overcharged, with resulting electrolysis of the electrolyte. During the second discharge period, the voltage decreased from 1.9 V to 1.5 V, and in the following charge period, the cell developed a short circuit after about 2 hr. These results indicate that recharging without short circuiting is possible when a suitable material is used as an insulator, but that the current density must be limited to avoid increasing the IR-free voltage above the decomposition potential of the electrolyte.

A new cathode cup design was used in Cells No. 12-15, but did not result in a significant improvement in cell performance. Cell No. 13 showed that a smooth recharge can be achieved in the horizontal orientation without short circuiting.

Cells No. 16, 17, and 18 were assembled to test a hot-pressing technique to effect a tight seal between the paste electrolyte and the grooved sealing surface of the cathode cup. Cells No. 16 and 17 had a glass insulating seal between the anode cup and the peripheral ring. The anode and cathode compartments were reversed as the peripheral ring was operated at the cathode potential, thus minimizing the possibility of lithium deposition on the ring during recharge (and possible short-circuiting of the cell). Early short circuits were experienced in Cells 16 and 17, apparently because of failure of the glass seals. Cell No. 18 was of a similar design, with the exception of a boron nitride ring used as the insulator between the anode cup and peripheral ring and another boron nitride ring between the anode cup and the paste electrolyte. The maximum open-circuit voltage was 2.2 V, but a high internal resistance of 0.64 ohm was observed. The cell was discharged about 10 hr at a current density of 0.036 A/cm^2 . During the first 2 hr, the voltage was about 1.5 V; it then increased to about 1.75 V where it remained for 8 hr, producing approximately 2 W and 12 A-hr. The cell was then recharged for 6 hr at 0.02 A/cm^2 . During this period, the open-circuit voltage increased rapidly to 2.05 V, where it remained constant. Data on the first discharge-charge cycle are presented in Fig. V-21. The cell was then discharged again and recharged for 6 hr with the open-circuit voltage increasing steadily from 2.08 V to 2.1 V, followed by a discharge at 0.035 A/cm^2 for 1 hr, with an average terminal voltage of 1.5 V. The test was terminated after 35 hr of operation when a short circuit developed. The performance of this cell was better than that of the previous 17 cells. On the first discharge, 72% of the theoretical capacity density was obtained. The design and cell assembly techniques used for Cell No. 18 were selected for the six cells that were used in the sealed-battery test (Section V.C.1.b of this report).

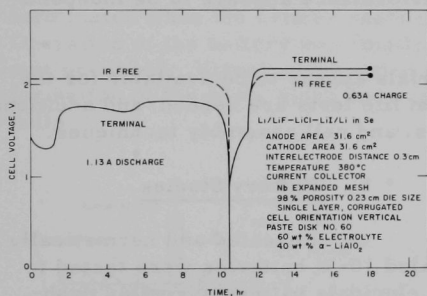


Fig. V-21. Electrical Performance of Cell No. 18.
ANL Neg. No. 308-2396.

In several of the cells, Li_2Se was observed in large amounts at the interface between the anode and the paste-electrolyte disk. This was attributed either to leakage of selenium past the paste electrolyte, where there was evidence of cracks or a poor seal, or to permeation of the electrolyte by selenium. The short cell lifetimes experienced in these tests are attributed to the transport of selenium from cathode to anode. A study to determine how to avoid selenium permeation of the electrolyte is under way.

(3) Conclusions from Single-Cell Studies

a) The electrical performance studies have indicated that a battery of five 7.5-cm-dia lithium/selenium cells will be capable of meeting the goals of 10 W of power and an energy-storage capacity of 120 W-hr. Calculations indicate that such a battery will fall within the design limits of weight (1.1 kg) and size (10-cm-dia, 8.4-cm-high cylinder).

b) A substantial improvement is needed in the cycle life and longevity of the cells. This problem is believed to be related to the transport of selenium to the anode by leakage, permeation of the electrolyte, or solubility of selenium-bearing species in the electrolyte. Means to avoid selenium transport are being investigated.

c) Further work is needed to improve cell recharge characteristics. This is closely related to the preceding item.

d) Short-term performance appears to be independent of cell orientation.

e) Suitable materials appear to be available for the cell components. However, longer-term life tests are needed, and additional work is required on sealants, insulators, and cell assembly techniques.

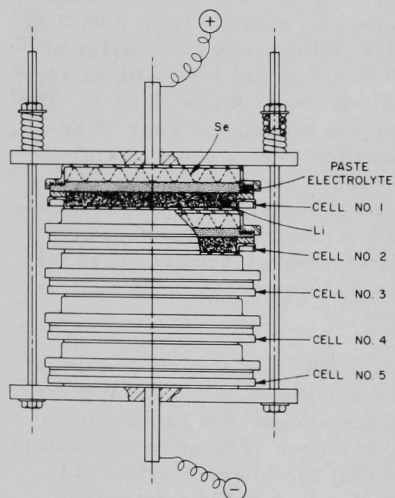


Fig. V-22. Schematic Diagram of Unsealed, Five-Cell Battery. ANL Neg. No. 308-2395.

b. Battery Studies

Unsealed and hermetically sealed 10-W batteries were tested to (1) elucidate battery assembly problems, (2) determine electrical performance, (3) study cell interactions, and (4) determine the performance of materials of construction under operating conditions. Future work will be directed toward increasing the power level to 30 W, and the cylindrical shape may be modified for implantation.

(1) Unsealed Battery Test

For the unsealed, five-cell battery (Fig. V-22), the cell design was similar to that used in Cells 12 to 15. The battery was assembled in a bipolar configuration with the cathode of each cell electrically connected to

the anode of the adjacent cell. The cells and battery were assembled in a helium glovebox to prevent contamination of the lithium and electrolyte disks by water. The battery was operated with the selenium uppermost in each cell. During the test, the total battery voltage, the voltage of each cell, and the current were continuously monitored and recorded.

During operation of the battery, a maximum open-circuit voltage of 10.45 V was obtained. Upon discharge at 1.3 A (0.04 A/cm^2), a terminal voltage of over 9.0 V (or the equivalent of about 12 W) was maintained for about 1 hr. After about 1.5 hr of operation, the two cells located at the lower end of the battery shorted, resulting in a three-cell battery instead of the original five-cell battery. The short circuit was attributed to softening of the paste disks, which resulted in a decrease in thickness of the paste below that required for separation of the anode and cathode. The discharge was terminated after 4 hr when the three-cell battery reached a potential of 4 V. After the battery had been held on open circuit for 1 hr, a charge of 1 A-hr was carried out. The battery was then discharged as a two-cell battery at a current of 1.3 A. This discharge was terminated when the battery reached a potential of 2.2 V after about 1 hr. Operation of the battery was finally terminated when a general short circuit occurred. Visual examination of the disassembled battery showed deformation of the paste disks and resulting leakage of selenium from the cells.

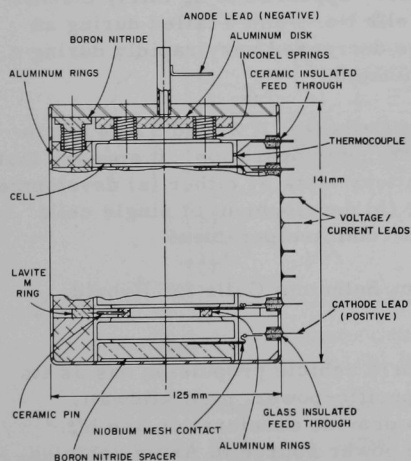


Fig. V-23. Schematic Diagram of Sealed Battery.
ANL Neg. No. 308-2394.

This was the first attempt to build and operate a 10-W battery. The operation of the battery at 12 W for 1.5 hr demonstrated that the lightweight design employed was capable of achieving the specified power level. The early failure of the battery illustrated the need for sealed single cells which are free from deformation of the paste electrolyte and leakage of selenium.

(2) Sealed Battery Test

An experimental six-cell battery (Fig. V-23) was developed which would allow (a) loading the hot cells into the housing, (b) welding the loaded battery at temperature, hermetically sealing the battery from the environment, (c) leak-testing the sealed battery, (d) transferring the battery at operating temperature from the helium glovebox to a hood in an air environment, (e) good temperature monitoring, and (f) shunting any inoperable cells out of the circuit.

Each cell was assembled and sealed in a helium glove-box using hot-pressing techniques (see Section V.C.1.a.). Each of the six cells exhibited good electrical performance prior to transfer to the housing, which was heated to 350°C. The first cell was placed on a niobium mesh contact with its anode side up. After all six cells were in place, with Lavite insulators and aluminum contact rings, Inconel springs were loaded and a stainless steel lid was arc-welded in place to seal the battery. The effects of various orientations and mild motion on battery performance were investigated. During the test, battery voltage, the voltage of each cell, and current were continuously recorded.

During the sealed-battery test, a maximum open-circuit voltage of 6.8 V was obtained with Cells No. 3, 4, and 6 functioning normally and Cells No. 1, 2, and 5 developing less than 0.5 V each. It is suspected that Cells No. 1, 2, and 5 experienced excessive temperature cycling during the cell-transfer operations, which resulted in cracking of the paste electrolytes. These cells were shunted out of the electrical circuit, and the system was operated as a 3-cell battery. After 1 hr of operation in a helium glovebox, the battery was transferred out of the glovebox to an air environment with no appreciable change in performance. The first discharge was conducted at 1.25 A (0.04 A/cm^2) with an average voltage of 4.6 V. The battery produced about 6 W of power for over 4 hr with a total discharge time of 5.5 hr. About 33 W-hr of electrical energy was obtained in the first discharge. The battery appeared to be fairly insensitive to motion as well as orientation. Cells No. 3 and 4 failed during an attempted recharge. The battery voltage decreased very rapidly during a second discharge, and the test was terminated.

The early failure of Cells No. 1, 2, and 5 was attributed to excessive cooling during the cell transfer operation. It appears that this problem can be avoided in future battery tests by either (a) development of isothermal cell-loading techniques or (b) development of single cells which can be assembled into a battery at room temperature.

2. High-Specific-Power Lithium/Selenium Cells for Hybrid Vehicle Propulsion⁵³

The battery program for hybrid vehicle propulsion has as its ultimate goal the development of high-specific-power, multikilowatt, lithium/selenium secondary batteries to provide acceleration and hill-climbing power to supplement the prime power source in Army vehicles. The present, shorter-term objective is to develop 7.5-cm-dia cells capable of 1 to 3 W/cm² short-time peak power densities with lifetimes of 1000 to 2000 hr and 1000 to 2000 charge-discharge cycles.

⁵³This work is sponsored by the U. S. Army Mobility Equipment Research and Development Center, Ft. Belvoir, Virginia.

The lithium/selenium cells operate at temperatures of 375°C or lower, and are composed of liquid lithium anodes, immobilized fused-salt electrolytes (in the form of a rigid paste), and liquid selenium cathodes.

Cells with an energy density of 0.5 W-hr/cm^2 at the 1-hr discharge rate (0.27 A/cm^2), a short-time peak power density of 2.3 W/cm^2 , improved charging characteristics (0.92 A-hr efficiency), and the capability of delivering 52% of the theoretical capacity density at the 1-hr rate have been demonstrated. Development of sealed cells with a 100-hr life at high performance has been unsuccessful. Cycle lives of 10 to 13 cycles, with decreasing performance, have been obtained during operating periods of 120 hr. The life-limiting factor has been the transference of selenium through the paste electrolyte to the lithium electrode, causing an increase of internal resistance and a loss of capacity.

a. Single-Cell Studies

An assembled 7.5-cm-dia cell, similar to all cells tested, is shown in Fig. V-24. The cells were operated in the vertical position. The cathode compartment contained about 50% void volume to allow for lithium transfer.

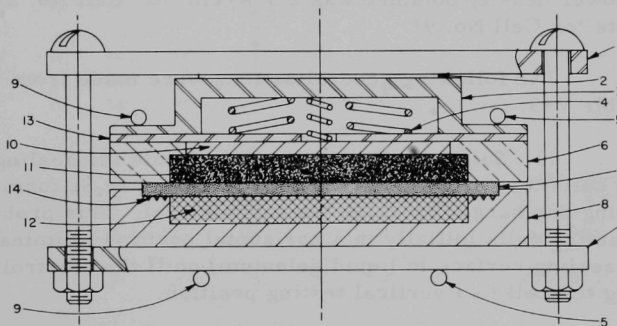


Fig. V-24. Components of Lithium/Selenium Cell with 7.5-cm Dia Paste Electrolyte. ANL Neg. No. 308-2393.

- | | | |
|---------------------------------------|---|--|
| 1. Clamping Plate, SS | 7. Paste Electrolyte | 12. Nb Mesh, 63% Porosity,
0.23-cm Die Size,
Containing Se |
| 2. Insulator, Al_2O_3 | 8. Cathode Cup, Nb-1 Zr | 13. Spring Plate, SS |
| 3. Anode Cover, SS | 9. Voltage Lead, SS | 14. Grooved Cathode
Sealing Surface |
| 4. Springs, Inconel-X | 10. Spacer Plate, Nb-1 Zr | |
| 5. Current Lead, SS | 11. SS Feltmetal, 90% Porosity,
67- μm Mean Pore Size,
Containing Li | |
| 6. Insulator, BN | | |

The paste electrolytes were prepared using lithium aluminate and/or boron nitride filler (of approximately $46 \text{ m}^2/\text{g}$ and $7 \text{ m}^2/\text{g}$ specific surface area, respectively) and LiF-LiCl-LiI eutectic (described in Section V.C.1.a). The surfaces of some paste electrolyte disks were coated with the lower-melting LiCl-LiBr-LiI-KI-CsI eutectic in an attempt to eliminate the permeability of the paste electrolyte to selenium. This eutectic has a composition (in mole percent) of 3.7% LiCl-9.1% LiBr-52.3% LiI-15.7% KI-19.2% CsI, and has a melting point of 184°C .

The electrical performance of single cells is evaluated in terms of voltage-current density and voltage-time behavior during constant-current discharge as a function of cell structure and number of charge-discharge cycles. The effects of various paste-electrolyte treatments, structural configurations of the cathode current collector, and changes of other cell parameters are being studied to identify the cell design that yields the highest power density and highest capacity density (with efficient selenium utilization). Table V-9 summarizes the electrical performance, experimental purpose, and results for the cells tested most recently. The maximum cell life observed was 120 hr and 13 cycles (to 1.0 V) for Cell No. 17. Figure V-25 shows the voltage as a function of capacity and capacity density for this cell. A constant discharge voltage of 1.6 V was observed for approximately 20 minutes during discharge 1. The maximum short-time peak power density obtained was $2.3 \text{ W}/\text{cm}^2$ for Cell No. 21 (similar to the results for Cell No. 9).

The following generalizations were made from the cells listed in Table V-9.

- 1) Selenium apparently leaked onto the sealing surface in some of the cells tested in the vertical position, and Li_2Se formed at this surface during discharge, breaking the cathode seal. This problem can be solved by heating cells initially in a horizontal position (eliminating exposure of the sealing surface to liquid selenium) until the electrolyte melts, then rotating the cell to a vertical testing position.

- 2) Cells using a paste electrolyte coated with LiCl-LiBr-LiI-KI-CsI showed better charging characteristics and a slower decrease in performance with time, e.g., Cell No. 17, Fig. V-25.

- 3) Capacity density, short-time peak power density, and selenium utilization appear to be dependent on the salt content of the paste electrolyte. Paste electrolyte cells with the highest LiF-LiCl-LiI content (Cells No. 14 and 19, containing 57 to 70 wt % LiF-LiCl-LiI) showed the highest capacity density (at the 1-hr rate) and the highest short-time peak power density. Addition of electrolyte to selenium (Cell No. 19) also increased the capacity density achieved. There is some indication, however, that the pastes of very high LiF-LiCl-LiI content (70 wt % for Cell No. 19)

are susceptible to cracking due to thermal expansion of the electrolyte. Further tests are required to verify this observation. The percent of selenium utilized at the 1-hr rate increases with the weight percent LiF-LiCl-LiI eutectic in the paste electrolyte. This relation may result from an increase in the size of the reaction zone for Li_2Se formation caused either by solubility of electrolyte in the cathode material or by electrolyte flooding at the paste-cathode interface. A 37% change in selenium utilization was observed for a 20 wt % change in LiF-LiCl-LiI content of the paste; more information is required at the higher and lower LiF-LiCl-LiI weight percentages to verify this.

TABLE V-9. Electrical Performance of 31.6-cm² Lithium/Selenium Cells at 380°C

Cell No.	Peak Power Density ^a (W/cm ²)	Discharge Current Density (A/cm ²)	Average Discharge Voltage (V)	Discharge Time (hr)	Capacity Density ^b (A-hr/cm ²)	Energy Density (W-hr/cm ²)	Fraction of Theoretical Capacity	Fraction of 1-hr Rate Current Density ^c	No. of Cycles	Testing Period (hr)	Purpose of Experiment	Results
9	2.2	0.15	1.8	0.27	0.04	0.07	0.074	0.59	5	72	Test cathode seal groove	Li ₂ Se at anode, ^d poor seal, low O.C.V. at end of test. ^e
10 ^f	0.8	-	-	-	-	-	-	-	-	24	Test paste (60 wt % eutectic) permeability to Se vapor	Li ₂ Se at anode, good seal, ^g low O.C.V. at end of test.
11 ^f	-	-	-	-	-	-	-	-	-	-	Test LiBr-RbBr coated paste	Li ₂ Se at anode, electrical short.
12 ^f	-	-	-	-	-	-	-	-	-	24	Test LiBr-RbBr coated paste	Li ₂ Se at anode, good seal, low O.C.V. at end of test.
13 ^f	0.9	-	-	-	-	-	-	-	-	30	LiCl-LiBr-LiI-KI-Csl in seal grooves ^h	Li ₂ Se at anode, good seal, low O.C.V. at end of test.
14	1.7	0.29	1.7	0.78	0.23	0.39	0.40	1.1	6	60	LiCl-LiBr-LiI-KI-Csl coated paste	Li ₂ Se at anode and at outer cathode perimeter, no Se loss, normal O.C.V. at end of test. ^h
15	0.4	0.15	1.3	1.70	0.25	0.32	0.38	0.55	2	30	Test BN filler paste	Li ₂ Se at anode and outer cathode perimeter, no Se loss, mushy paste.
16	0.6	0.26	1.4	0.77	0.20	0.28	0.33	1.0	6	56	LiCl-LiBr-LiI-KI-Csl coated paste	Li ₂ Se at anode and at outer cathode perimeter, no Se loss.
17	0.7	0.27	1.5	0.65	0.18	0.27	0.33	1.0	13	120	LiCl-LiBr-LiI-KI-Csl coated BN and LiAlO ₂ filler paste	Li ₂ Se at anode and at outer cathode perimeter, no Se loss, longest testing period, paste fractured near seal.
18 ^f	0.7	-	-	-	-	-	-	-	-	-	LiF-LiCl-LiI coated paste	Se leakage, distorted paste.
19	1.6	0.27	1.7	1.0	0.27	0.46	0.52	1.0	2	8	70 wt % LiF-LiCl-LiI paste and salt in Se	Paste cracked, good capacity.
20	1.2	0.26	1.6	1.2	0.31	0.50	0.43	1.0	2	8	LiCl-LiBr-LiI-KI-Csl coated 70 wt % paste	Li ₂ Se at anode and at outer cathode perimeter, no Se loss.
21	2.3	0.27	1.6	1.0	0.27	0.43	0.39	1.0	5	60	LiCl-LiBr-LiI-KI-Csl coated BN and LiAlO ₂ paste	Li ₂ Se at anode and at outer cathode perimeter, no Se loss, paste fractured near seal.
22	0.7	0.12	1.6	1.0	0.12	0.19	0.23	0.44	3	40	Insulator on cathode seal	Li ₂ Se at anode and at outer cathode perimeter, no Se loss.
L-1	0.6	0.26	1.3	0.13	0.04	0.05	0.09	1.0	1	45	LiCl-LiBr-LiI-KI-Csl coated paste	Paste cracked.
L-2	0.4	0.21	1.3	0.51	0.12	0.14	0.22	0.8	3	20	LiCl-LiBr-LiI-KI-Csl coated paste	Li ₂ Se at anode, poor seal.
L-3	0.3	0.30	1.2	0.28	0.08	0.10	0.15	1.1	2	28	LiCl-LiBr-LiI-KI-Csl coated paste	Li ₂ Se at anode, poor seal.

^aShort-time peak power density measured a few seconds after closing the circuit.

^bCapacity density measured for the first discharge during the first hour of cell testing to a 1.0 V cut-off.

^cRatio of the discharge current density divided by the current density (0.27 A/cm²) for a 1-hr discharge time to 1.0 V.

^dThe presence of Li₂Se at the anode interface was determined by electron microprobe for 3% of the cells tested. Most of the determinations for Li₂Se were made from visual examination of the anode section.

^eUnless stated otherwise, open-circuit voltage (O.C.V.) at cell shut-down was above 2.0 V.

^fNo capacity measurements were made for these cells. The purpose of these experiments was to determine selenium permeability of the paste electrolyte in the absence of electrical measurements.

^gA good seal was one of no selenium leakage nor product deposition at the outer cathode perimeter.

^hAll subsequent cells contained LiCl-LiBr-LiI-KI-Csl eutectic in the cathode seal grooves.

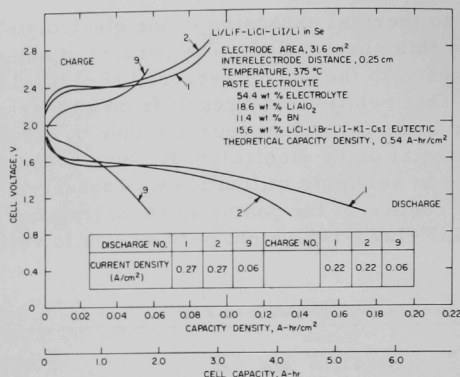


Fig. V-25

Voltage-Capacity Density Curves for
Lithium/Selenium Cell No. 17.
ANL Neg. No. 308-2392.

4) The problem which appears unaffected by the changes made in these cell tests is formation of Li_2Se at the anode and outer cathode perimeter. Various elements will be added to the selenium and changes will be made in the cell construction and testing procedures for future cell tests in an attempt to minimize this problem.

b. Paste Electrolyte Studies

An important area of investigation of lithium/selenium cells is the development of paste electrolytes of minimum selenium permeability (selenium transfer through pores or microcracks in the paste), maximum strength, minimum weight, and minimum ionic resistivity to serve as separators between the lithium anode and selenium cathode. Development work on the paste electrolyte consisting of molten LiF-LiCl-LiI eutectic with a lithium aluminate filler has emphasized ionic resistivity and permeability.

(1) Resistivity of Paste Electrolytes

Measurements of paste resistivities were carried out to obtain an indication of the minimum possible internal cell resistance. The measurements were obtained by a dc, potentiometric technique with each paste disk held between two lithium-impregnated, stainless steel Feltmetal disks. Figure V-26 shows experimental and theoretical resistivity ratios for pastes at 350°C as a function of volume fraction of electrolyte. The theoretical values are based on Maxwell's equation⁵⁴ for conduction in heterogeneous systems; paste resistivity/salt resistivity = $(2+f)/(2-2f)$, where f = volume fraction of filler. It was concluded that the conditioning

⁵⁴R. E. Meredith, C. W. Tobias, in *Advances in Electrochemistry and Electrochemical Engineering*, vol. 2, p. 15, Interscience, New York (1962).

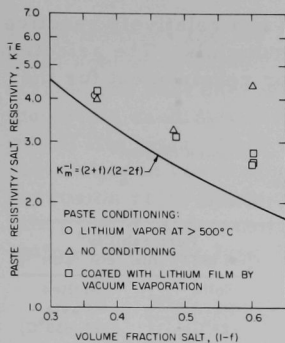


Fig. V-26

Dependence of Resistivity Ratios at 350°C on Salt Content for Paste Electrolyte Samples Prepared from Lithium Aluminate and the LiF-LiCl-LiI Eutectic. ANL Neg. No. 308-2391.

treatments, indicated in Fig. V-26, which were intended to promote interfacial contact between paste and lithium electrode, had no effect on paste resistivities for samples containing 40 and 50 wt % salt, and also that paste-electrolyte resistivities exceeding predictions from Maxwell's theory by factors of no more than 1.1 to 1.4 can be realized.

(2) Permeability of Paste Electrolytes

The permeability of paste electrolytes to gaseous helium implies a mechanical imperfection as the possible cause of the interelectrode leakage of selenium observed in cell tests and described in Section V.C.2.a. The development of pastes with minimum permeability was therefore considered a primary objective. Studies of the effect of fabrication procedure on permeability demonstrated that the procedure can be altered to produce pastes with significantly lower permeability.

We have observed that pastes conventionally prepared by pressing a filler-salt mixture are most permeable, that pastes prepared by the method of Tantram et al.⁵⁵ (allowing salt to melt into a cake of filler-salt mixture) are less permeable, and that pastes prepared by allowing salt to melt into a cake of pure filler are least permeable. The cracking of pure filler disks of 7.5-cm diameter during the infiltration by molten salt was the main difficulty to be overcome in the development of this last method. Pure filler disks pressed at 1000-1200 kg/cm² almost invariably cracked. Pure filler disks of 7.5-cm diameter were successfully infiltrated, however, under the following conditions: a filler disk, previously pressed at 600 kg/cm² at 150°C, was heated to 450-460°C on a tantalum plate protected from drafts with the heat source at the bottom face and edges. About 60 to 75% of the required salt was added as a powder to the top face, mainly near the edges, in small increments that melted immediately. The salt distributed throughout the disk by flowing from edge to center. After cooling to 25°C at 1-3°C/min, the disk was overturned and the remainder of the required salt was added similarly. Table V-10, listing the permeabilities of various samples, indicates the significantly lower permeability of pastes prepared by the infiltration of pure filler disks.

c. Materials of Construction

The development of reliable, long-lived lithium/selenium secondary batteries requires corrosion-resistant materials. Selenium,

⁵⁵A. Tantram, A. Tseung, B. Harris, in Hydrocarbon Fuel Cell Technology, B. Baker, ed., pp. 187-211, Academic Press, New York (1965).

lithium, and the molten salts utilized in these cells are relatively reactive and consequently are corrosive to many common materials. The selection of suitable corrosion-resistant materials is a major requirement for the successful utilization of these batteries.

TABLE V-10. Permeabilities of Paste Electrolyte Disks to Gaseous Helium^a

Fabrication Method	Disk Dia (cm)	Disk Pressing Pressure (kg/cm ²)	Disk Pressing Temp. (°C)	Wt % Salt	Permeability ^b [ml (STP) min ⁻¹ cm ⁻² atm ⁻¹]	
					Solid Paste (25°C)	Molten Paste (370-400°C)
Conventional ^c	1.3	700-1050	25-100	50-60	2-100	< 3-30
Infiltration of pure filler ^d	1.3	700-1050	25-100	50-60	< 0.8	< 3
Conventional ^c	7.5	1300	200	60	1	-
Infiltration of mixture ^e	7.5	1200	150	56-57	0.09-4.0	-
Infiltration of pure filler	7.5	600	150	~60	< 0.04	-

^aThe permeabilities and conditions listed are ranges representing observations on a number of samples.

^bCorrected to 0.25-cm thickness.

^cDisks were pressed from a pulverized and sintered mixture of filler and all the required salt.

^dAll the salt was added by allowing it to melt into a cake pressed from filler powder only.

^eA fraction of the salt was added by allowing it to melt into a cake pressed from a salt-poor mixture of filler and salt.

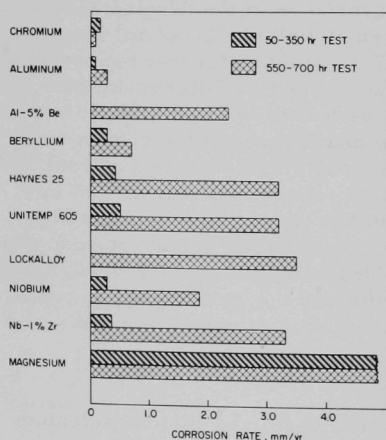


Fig. V-27. Corrosion Rates Observed in 20 at. % Li-Se Mixtures (temperature, 375°C; dynamic isothermal capsule tests). ANL Neg. No. 308-2375.

Current emphasis is on the cathode compartment, which requires a material resistant to the selenium and lithium-selenium alloys that are present in the cathode compartment in the partially discharged state. Most corrosion tests are performed with a 20 at. % lithium-selenium mixture, which was chosen as representative of the cathode composition of a partially discharged cell.

Figure V-27 summarizes the corrosion data for the more corrosion-resistant materials examined in this program. The results of both short-term (50-350 hr) and longer-term (550-700 hr) dynamic isothermal capsule tests (in which the corrosion specimen is sealed in an evacuated quartz capsule along with a 20 at. %

Li-Se mixture and the capsule rotated during equilibration to produce uniform specimen exposure) are included. Chromium has consistently demonstrated the best corrosion resistance to lithium-selenium mixtures and is the prime candidate for use in the construction of cells that will be used in initial life tests. Both beryllium and aluminum have demonstrated higher variability in corrosion resistance and, on some occasions, have yielded corrosion rates lower than that of chromium. If the cause of this variability could be determined, one of these materials might prove to be a better choice for long-lived cells.

3. High-Specific-Energy Lithium/Sulfur Cells for Electric Vehicles⁵⁶

The use of electrically powered automobiles could greatly decrease the amount of air pollution in urban areas. However, an all-electric automobile is not practical at present because the batteries that are available have an insufficient energy-storage capacity per unit weight, and are therefore heavy, bulky, and too costly for general consumer acceptance. The ultimate goal of this program is to develop the technology required to construct multikilowatt secondary batteries capable of powering a practical electric family automobile. Such a battery must have an energy-storage capability of 200 W-hr/kg, be able to deliver power at a peak rate of 200 W/kg, and cost no more than about \$10/kW-hr. The immediate objectives of the program are to investigate the performance characteristics of lithium/sulfur cells, to develop a cell design suitable for vehicle application, and to identify appropriate materials of construction.

a. Single-Cell Studies

The objective of the single-cell studies is to determine those conditions under which the cells will deliver capacity densities of 0.4 A-hr/cm² or greater at current densities of 0.3 to 1.0 A/cm². These criteria are based on the performance requirements of an electric family automobile and an assumed battery configuration.

Electrical performance tests were conducted on cells of the type Li/LiX/S, Li/LiX/P₄S₁₀, and Li/LiX/P₄S₃, where LiX represents a molten halide salt containing lithium cations. The experimental cells, with electrode areas of 1 to 5 cm², were operated at temperatures of about 325 to 400°C under a helium atmosphere. The cell configuration, cathode current-collector structure, and cathode reactant were investigated by means of electrical performance tests. In general, the anode consisted of liquid lithium contained in stainless steel Feltmetal, and the cathode was molten sulfur, P₄S₁₀, or P₄S₃ contained in a porous current-collector

⁵⁶This work was sponsored by the National Air Pollution Control Administration of CPE, Public Health Service, U.S. Dept. of Health, Education and Welfare.

structure. The anode and cathode assemblies were immersed in the molten-salt electrolyte with an interelectrode distance of 0.3 to 1.0 cm.

Electrical performance tests were conducted on a series of cells to determine the effects of different operating conditions and variations in the cell design. Most of the lithium/sulfur cells had an open-circuit potential of 2.1 to 2.38 V and a short-circuit current density between 4.8 and 8.5 A/cm².

The effect of temperature on cell performance was investigated briefly. When two identical cells were discharged at the same current density (1.0 A/cm²), but at different temperatures (364 and 385°C), the capacity densities above 1.0 V were 0.022 and 0.052 A-hr/cm², respectively. A similar result was obtained when a cell with a molybdenum-foam cathode current collector was operated with current densities of 0.33 and 1.0 A/cm² at temperatures between 350 and 400°C. The capacity density of the cell nearly doubled with a 50°C increase in temperature (0.092 vs. 0.056 A-hr/cm² above 1.0 V). With the present cell designs and materials, it appears that a minimum operating temperature of about 375°C is required to achieve acceptable capacity density. Lower temperature operation may become possible, however, if chemical additives can be used to decrease the viscosity of sulfur, or if other techniques can be used to increase the diffusion rate of the product within the cathode.

Similar cells were operated with sulfur, P₄S₁₀, and P₄S₃ cathodes to evaluate the feasibility of using phosphorus as an additive in sulfur cathodes. The results of the electrical performance tests are listed in Table V-11. The P₄S₃ cell was inferior to the other two with respect to both capacity density and energy density. The lithium/sulfur cell is theoretically capable of achieving higher capacity densities, if the sulfur can be fully utilized, because of its higher capacity per unit volume or weight. The lithium/P₄S₁₀ cell warrants further investigation because a higher energy density may be possible, and because practical design problems could be alleviated by its lower vapor pressure.

TABLE V-11. Comparison of Lithium/Sulfur, Lithium/P₄S₁₀, and Lithium/P₄S₃ Cells

Anode: Lithium
Cathode: as indicated
Electrolyte: LiBr-RbBr eutectic salt (mp ~278°C)
Interelectrode distance: 1 cm
Cathode current collector: stainless steel Feltmetal, 80% porosity, 29 µm mean pore dia.

Cathode Material	Temp (°C)	Current Density (A/cm ²)	Theoretical Capacity Density (A-hr/cm ²)	Capacity Density above 1.0 V (A-hr/cm ²)	Short-Circuit Current Density (A/cm ²)	Open-Circuit Voltage (V)	Cathode Material	Temp (°C)	Current Density (A/cm ²)	Theoretical Capacity Density (A-hr/cm ²)	Capacity Density above 1.0 V (A-hr/cm ²)	Short-Circuit Current Density (A/cm ²)	Open-Circuit Voltage (V)
Sulfur	375	0.57	0.50	0.114	-	2.3	P ₄ S ₁₀	373	0.21	0.39	0.069	-	2.4
Sulfur	355	0.46	0.73	0.119	6.5	2.3			0.31		0.073		
	365	0.34		0.124			P ₄ S ₁₀	340	0.31	0.41	0.082	6.2	2.7
	364	1.03		0.022				357	0.60		0.092		
	363	0.34		0.103				372	0.31		0.116		
P ₄ S ₁₀	375	0.12	0.40	0.074	-	2.5	P ₄ S ₃	377	0.13	0.28	0.053	-	2.2
P ₄ S ₁₀	368	0.21	0.39	0.015	-	2.5			0.33		0.029		
		0.31		0.009					0.41		0.027		
		0.52		0.007					0.64		0.037		

Because of the low electronic conductivities of sulfur and phosphorus-sulfur compounds (about 10^{-10} and 10^{-7} ohm $^{-1}$ cm $^{-1}$, respectively, at 375°C), an efficient cathode current collector structure is necessary. Table V-12 shows the results of electrical performance tests of cells with various types of cathode current collectors. The highest capacity densities were obtained with the molybdenum foam and the stainless steel Feltmetal. The high performance of the molybdenum foam is encouraging because several materials, such as beryllium, niobium, and chromium, which are not available as Feltmetal, can be fabricated into foams.

TABLE V-12. Effect of Cathode Current Collector on Lithium/Sulfur Cell Performance

Anode: lithium
Cathode: sulfur
Electrolyte: LiBr-RbBr eutectic salt (mp ~278°C)
Interelectrode distance: 1.0 cm

Cathode Current Collector			Temp. (°C)	Current Density (A/cm ²)	Theoretical Capacity Density (A-hr/cm ²)	Capacity Density above 1.0 V (A-hr/cm ²)
Material	Porosity (%)	Mean Pore Dia (μm)				
Stainless steel Feltmetal (Huyck)	80	29	375	0.57	0.50	0.114
Stainless steel Fibermetal (Brunswick)	85	40	375	0.41	0.26	0.048
Molybdenum foam	75	30	400	0.44	0.46	0.143
			400	0.88		0.051
Molybdenum foam	82	a	385	0.43	0.62	0.121
				0.85		0.060
				1.39		0.023
Niobium expanded mesh	76	(0.24 cm) ^b	385	0.58	1.2	0.005
Chromium foam	68	25	385	0.60	0.43	0.004
Stainless steel Fibermetal (Brunswick)	92	30	385	0.44	0.32	0.003

^aNot available.

^bDie size.

A study to determine the optimum cathode thickness in a practical cell design was made. Three similar Li/LiBr-RbBr/S cells were operated with Type 302 stainless steel Feltmetal current collectors having thicknesses of 0.16, 0.32, and 0.48 cm. The thickness of the cathode had no effect upon the capacity density at various current densities, indicating that the effective thickness was 0.16 cm or less.

In view of the above results, a laminated cathode current collector was designed with the objective of increasing the cathode-electrolyte interfacial area per unit volume. A cell of this design is shown

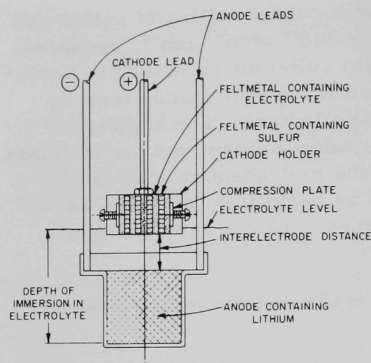


Fig. V-28. Laminated-Cathode Lithium/Sulfur Cell. ANL Neg. No. 308-2390.

previous design. As the current density was increased from 0.52 to 1.04 A/cm², the capacity density above 1.0 V decreased from 0.52 to 0.23 A-hr/cm². The largest percentage of theoretical capacity achieved with this cell was 25%, based on Li₂S as the final reaction product. This cell had a capacity density consistent with the requirements of vehicular propulsion, but this performance would have to be obtained in about one-third of the experimental cathode volume before these cells would be practical.

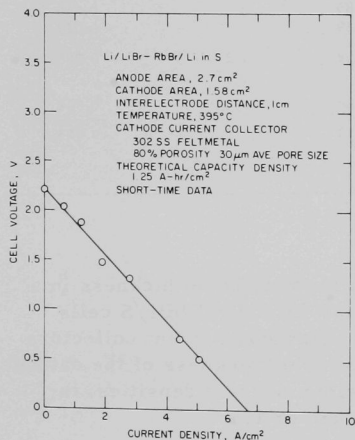


Fig. V-29. Voltage-Current Density Characteristics of a Lithium/Sulfur Cell with a Laminated Cathode. ANL Neg. No. 308-2389.

in Fig. V-28. The cathode consisted of alternating, thin layers of Type 302 stainless steel Feltmetal, the alternate layers being impregnated with sulfur and with electrolyte. The voltage-current density characteristics of a cell of this type are shown in Fig. V-29. The open-circuit voltage of this cell was 2.2 V, and the short-circuit current density was 6.6 A/cm². The linear voltage-current density relationship and the high short-circuit current density indicate that these cells possess adequate power densities for vehicular application. Voltage-capacity density data for a similar cell are presented in Fig. V-30. The results are similar to those obtained for other cells of the

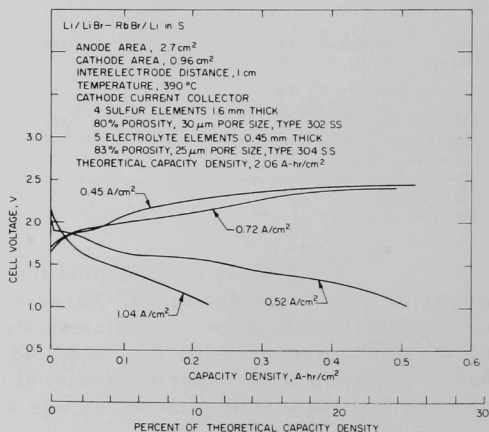


Fig. V-30. Voltage-Capacity Density Characteristics of Lithium/Sulfur Cell with Laminated Cathode. ANL Neg. No. 308-2388.

A Li/LiCl-KCl/P₄S₁₀ cell with a laminated cathode consisting of alternating molybdenum-foam layers containing electrolyte and porous graphite layers containing P₄S₁₀ was subjected to a series of discharge-charge cycles. Although the P₄S₁₀ utilization was low (15-17% of the sulfur), the cell performance remained constant over 15 discharge-charge cycles at current densities of 0.1 to 0.5 A/cm². This result suggests that no serious deterioration of the cell occurs during this amount of discharge-charge cycling. However, additional work is needed to raise the capacity density while improving the cycle life. For use in electric vehicles, a lithium/sulfur battery should have a cycle life of at least 300 charge-discharge cycles and a lifetime of three years or more. At present, the cycle life and lifetime of the experimental cells appear to be limited by the loss of sulfur or P₄S₁₀ from the cathode.

b. Studies of Molten-Salt Electrolytes

In the selection of a molten-salt electrolyte and a cathode material for a practical lithium/chalcogen secondary cell, it is necessary to have pertinent information on the phase relationships and mutual solubilities of these two materials and possible chemical reactions that could decrease the capacity or cycle life of the cell. A basic chemical study is being undertaken to understand the nature of the solutions of sulfur-bearing species in molten-salt electrolytes and to find methods of minimizing or eliminating the solubility. The initial work, directed to the formation and study of the chemical behavior of sulfur-bearing species in molten halide salts, will involve the preparation, characterization, and analysis of molten salt solutions containing known concentrations of sulfur and sulfide.

c. Materials, Seals, and Insulators

Additional corrosion tests have been performed to identify suitable materials for the different cell components, such as anode and cathode housings, current collectors, insulators, and seals. Specimens of the metallic materials, which might be used for cathode housings and current collectors, were exposed to molten 20 at. % lithium-80 at. % sulfur mixtures at 375°C in short-term screening tests of 100-300-hr duration. Some of the more promising materials were subjected to longer (~600-hr) tests.

The results of the tests are shown in Table V-13. In the shorter term tests, the corrosion rates of the stainless steels were less than about 0.15 mm/yr. The nickel-base alloys were more variable in their performance, as shown by the difference in the results for Hastelloy X and Monel, as opposed to those for Hastelloy X and Inconel 702. Among the other materials tested, molybdenum, chromium, Zircaloy-2, and niobium showed the greatest corrosion resistance. Although the results for magnesium and aluminum were somewhat variable, these metals and their alloys are of special interest because of their light weight and low cost.

TABLE V-13. Comparison of Corrosion Rates of Metals
by 20 at. % Lithium-Sulfur at 375°C

Test Material	Shorter-Term Tests		Longer-Term Tests		Remarks
	Exposure Period (hr)	Corrosion Rate ^a (mm/yr)	Exposure Period (hr)	Corrosion Rate (mm/yr)	
<u>Stainless Steels (Ni-Cr)</u>					
2 RK 65	311	0.03	620	0.67	Conductive film
347	311-331	0.02-0.09	620	1.5-1.9	Conductive film
2 RN 65	311	0.10			Conductive film
2 RE 10	311	0.12			Conductive film
Worthite	311	+0.07			Conductive film
Croloy 16-1	304	+0.14			Conductive film
Carpenter 20	304	+0.21			Conductive film
Durimet 20	100	+0.24			Adherent film
<u>Stainless Steels (Mn-Cr)</u>					
205	309	0.05	620-642	0.35-5.4	Poorly conductive film
Tenelon	304	0.18			
<u>Nickel-Base Alloys</u>					
Hastelloy X	331	0.02	620-642	0.17-2.0	Conductive film
Inconel 702	311	0.02	615	0.07	Nonconductive film
Inconel 800	331	0.23			Conductive film
Hastelloy B	309	1.93			Dissolution
Monel	304	3.68			Dissolution
Inconel 718	100	+0.12	642	0.07-0.10	Adherent film
Inconel 600			620	0.54	Nonconductive film
Hastelloy C			615	0.49	Poorly conductive film
<u>Other</u>					
Molybdenum	100	0.01	615	0.001-0.07	No detectible corrosion
Chromium	100-328	0.01-+0.17	642	0.01-0.16	Poorly conductive film
LT-1	101	0.03			Al ₂ O ₃ reduction
Zircaloy-2	101-136	0.05-+0.01	620	0.94-1.1	Nonconductive film
Niobium	306	0.09	615	1.6-2.4	
Magnesium	304-331	0.11-0.24			Nonconductive film
Aluminum	304-331	0.02-0.85	620-642	0.01-2.4	Nonconductive film
Titanium	304	0.48			
Beryllium	233	0.55			Sample pitted
Tantalum	101	0.56	615	2.0	Dissolution
Nickel	100	1.80			Dissolution
Iron	100	2.36			Dissolution

^a "+" indicates a weight gain of the specimen as a result of film formation.

The 600-hr tests were performed to determine the effect of exposure time upon the corrosion rates and to evaluate the validity of using linear extrapolation to obtain annual rates. In several instances, such as Type 205 stainless steel, Hastelloy X, and Zircaloy-2, the corrosion rates were higher than those for the shorter term tests (see Fig. V-31). The reason for this behavior is not fully understood, although it may be related to intergranular attack or to the temporary existence of a protective film. Other materials that showed little corrosion in the shorter-term tests, e.g., molybdenum and chromium, continued to have low corrosion rates in the longer-term tests. Aluminum showed a highly variable

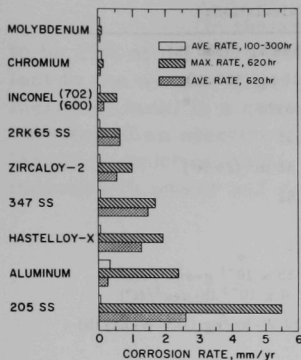


Fig. V-31

Comparison of Corrosion Rates in Li-S Mixtures (temperature, 375°C; composition, 20 at. % Li-80 at. % S; test duration, 100-300 or 620 hr as shown). ANL Neg. No. 308-2387.

electrochemical effects can result from potential differences within the cell. The performance of the more promising materials will be evaluated in long-term cell tests.

corrosion behavior in the longer tests. Most of the observed corrosion rates were similar to those obtained in the short-term tests.

Additional tests were conducted on the corrosion of insulating materials by molten lithium and lithium-sulfur mixtures. An 1168-hr immersion test at 375°C showed hot-pressed, high-purity BeO to be the most resistant to lithium attack of any insulator material tested to date. The average corrosion rate was 0.011 mm/yr, as opposed to rates as high as 12 mm/yr, which were observed with other types of BeO (commercial grade and recrystallized grade).

Although the above results on corrosion rates are useful in screening potential materials for cell components, it must be recognized that the observed rates are not necessarily those that would occur in an operating cell where

d. Design Calculations for Electric Vehicles

Preliminary calculations were made to provide an estimate of the performance that might be expected of a battery-powered family automobile. Because several simplifying assumptions were made in the calculations, the results represent the maximum possible performance for a battery of a particular specific energy (220 W-hr/kg).⁵⁷ The most important simplifying assumption was that the specific energy is not affected by the power density or the depth of discharge in the individual segments of the driving profile, although it is known that the deliverable specific energy is affected by both of these factors. More refined calculations incorporating the battery discharge characteristics are currently in progress.

The automobile was assumed to have a curb weight of 1588 kg (3500 lb) and to carry a payload (passengers and luggage) of 227 kg (500 lb). The battery weight was 397 kg (875 lb) with a deliverable specific energy of 220 W-hr/kg (100 W-hr/lb). Other assumptions related to the vehicle are listed in Table V-14.

⁵⁷Pb/PbO₂ batteries common in current automobiles have specific energies of 5-25 W-hr/kg.

TABLE V-14. Assumptions Used in Vehicle Calculations

Curb weight of vehicle	1588 kg (3500 lb)
Payload of vehicle	227 kg (500 lb)
Tire rolling resistance coefficient	0.0175
Air drag coefficient	0.35
Frontal area of vehicle	2.32 m ² (25 ft ²)
Efficiency (battery output to wheels)	0.82
Conversion factor from linear to total acceleration (including rotational)	1.1
Air density	1.25×10^{-6} g-sec ² /cm ⁴ (2.4×10^{-3} lb-sec ² /ft ⁴)
Battery specific energy (delivered)	220 W-hr/kg (100 W-hr/lb)
Accessory Power	
No accessories	0 W
Normal service accessories (lights, windshield wipers, heater blower, defrosters, radio, etc.)	230 W
Convenience option (normal service accessories plus air conditioning, power steering)	6530 W

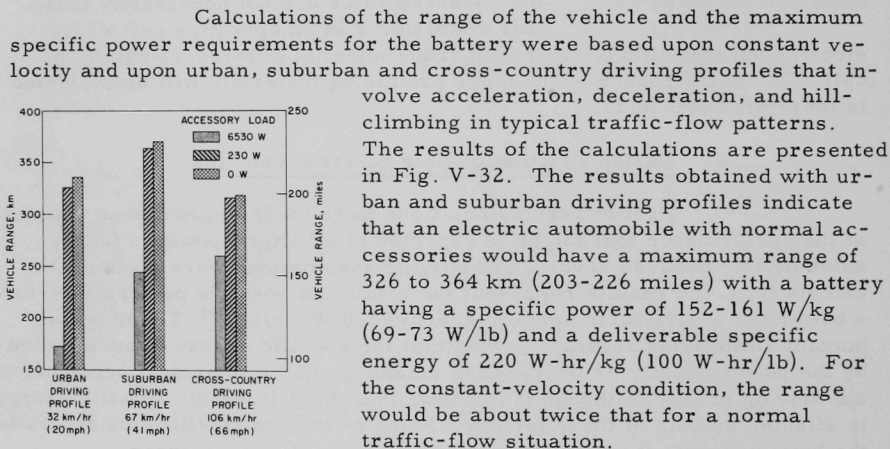


Fig. V-32. Vehicle Range Under Selected Driving Profiles.
ANL Neg. No. 308-2386.

The calculations were extended to determine the increase in performance that could be obtained by the use of regenerative braking (an electro-mechanical system to recover part of the energy normally dissipated during braking and deceleration). The results of an urban driving profile analysis indicate that the range of the vehicle could be increased by as much as 40%, assuming that 50% of the braking and deceleration energy could be recovered.

In the above calculations, the battery weight was assumed to be 25% of the curb weight of the vehicle, which is approximately equivalent to the weight of the power plant (engine, transmission, exhaust system, fuel, fuel tank) in a conventional internal-combustion-engine passenger vehicle. If an electric vehicle were designed specifically to allocate a larger proportion of the total vehicle weight to the battery, a significant increase in power and range could be achieved.

VI. NUCLEAR SAFEGUARDS STUDY

At the request of the AEC's Office of Safeguards and Materials Management (OSMM), a program study has been initiated on nuclear safeguards, that is, measures designed to detect and guard against the diversion of strategically significant nuclear materials for unauthorized uses. It is desired that these measures will provide credible assurance that no diversion has occurred. Argonne's efforts in this regard are specifically directed at provisions for future privately owned plants for conversion, preparation, and fabrication of nuclear fuels into finished nuclear reactor fuel assemblies. Of primary concern are materials of such high strategic value as ^{239}Pu , ^{233}U and highly enriched ^{235}U fuels. Of secondary concern are low enriched (less than 20%) uranium fuels.

The study will include materials accountability, physical protection, and surveillance. Results of the study are for use by the AEC-OSMM in developing general criteria for future U.S. plants to assure that adequate safeguards are established and maintained. The OSMM will ultimately apply the study results for (1) current international (IAEA) negotiations under the Non-Proliferation Treaty, and (2) input to the development of safeguards criteria required in connection with licensing and regulation of future private domestic facilities.

The Argonne study is being performed principally by Chemical Engineering Division personnel. Significant assistance to the study is being given by people from other parts of ANL. The initial efforts were devoted to becoming familiar with existing reactor fuel conversion, preparation, and fabrication facilities. This was followed by visits to a number of these plants. Thus far, preliminary general design criteria have been formulated and discussed with the personnel of OSMM and Division of Regulation. Initial drafts of the criteria were made available to the AEC-OSMM by the end of this calendar year for internal and later external comment.

Discussions are now under way between ANL and the AEC-OSMM for possible future support and interest of further work in this general area.

VII. FLUIDIZED-BED COMBUSTION OF FOSSIL FUELS

Fluidized-bed combustion is being studied at Argonne National Laboratory (ANL) as a method of reducing the quantity of atmospheric pollutants (oxides of sulfur and nitrogen) released during the combustion of fossil fuels. This work is part of a large program, under the direction of the National Air Pollution Control Administration, on various aspects of fluidized-bed combustion research. Numerous government agencies and industrial firms are involved in this program.

The concept of fluidized-bed combustion involves burning fuel in a fluidized bed of solids with simultaneous feeding of particulate limestone or dolomite additive to control sulfur dioxide emission. A fluidized-bed combustor offers, in addition to in situ control of SO_2 emission, high heat-transfer rates and efficient contacting for gas-solids reactions. Also, since combustion can be carried out at lower temperatures ($\sim 800^\circ\text{C}$) in a fluidized bed than in conventional combustors, nitrogen oxide formation may be lowered.

The stainless steel fluidized-bed combustor employed in the ANL studies has a 6-in. dia and 6-ft length; upstream from the combustor is a gas preheater for the fluidizing air. Vibratory-screw feeders deliver the coal and the limestone additive into air transport streams for injection into the fluidized-bed combustor. The flue gas from the combustor passes through primary and secondary cyclone separators and a final filter of glass fiber where entrained solids are removed. Infrared spectrometry and other suitable instrumental methods are used to measure concentrations of the constituents of the flue gas.

An objective of the bench-scale experimental work is to determine the conditions necessary to achieve a high degree of SO_2 removal from the flue gas and a high utilization of the limestone or other additive material. Work during the period of this report included bench-scale, coal-burning experiments with limestone additive of two particle sizes (44- μm average dia or smaller in several series of experiments and an average diameter of several hundred microns in other series). These experiments indicated effects on SO_2 removal of (1) Ca/S mole ratio in the feed, (2) type of limestone material, (3) gas velocity, and (4) combustion temperature. Combustion of natural gas was investigated to demonstrate that low nitric oxide (NO) levels can be attained.

Modeling studies were performed to predict the extent of SO_2 removal as a function of various operating parameters and to predict the effect of coal-injection procedure on the mixing of coal particles in a fluidized-bed combustor.

A. Coal-Combustion Experiments with Pulverized Limestone

A series of bench-scale experiments was performed to compare SO_2 removal with pulverized limestone No. 1359 and Tymochtee dolomite additives. In these runs, the initial fluidized bed consisted of refractory alumina particles. Base-line reaction conditions were a combustion temperature of 1600°F , an average additive particle size of $25\ \mu\text{m}$, a superficial gas velocity of 3 ft/sec, 10-20% excess air, a fluidized-bed depth of 2 ft, and coal and limestone addition rates giving a Ca/S mole ratio of 2.5 in the feed streams. With these conditions, the reduction in SO_2 concentration of the flue gas was higher for the dolomite than for the limestone, 90 and 83%, respectively. Variation of temperatures in the range 1550 - 1650°F had little effect on SO_2 removal by the pulverized limestone. Removals were 73, 83, and 77% at 1650, 1600 and 1550°F , respectively. An increase in superficial gas velocity from 3 to 9 ft/sec decreased SO_2 removals by about 10%. Decreasing the Ca/S mole ratio from 2.5 to 2.0 to 1.5 decreased SO_2 removals from 83 to 70 to 57%, respectively, at 1600°F .

Recycle to the combustor of a finely divided limestone-flyash mixture that had been elutriated from the bed did not increase SO_2 removal, contrary to the expectation that recycle would increase SO_2 removal because of the additional reaction potential of the partially sulfated limestone contained in the elutriated solids. Laboratory-scale tests later confirmed that reactivities of limestone in flyash and of fresh limestone are similar. The failure of recycled material to increase SO_2 removal in the bench-scale combustor was probably due to the fine particles having a short residence time in the bed.

The extent of calcination and sulfation (i.e., CaO utilization) of the final bed material and of the solids collected overhead was determined by analysis. The results show that the material retained in the fluid bed had the greatest extent of calcination ($\sim 100\%$) and the highest extent of CaO utilization (70%). Material collected in the primary cyclone had the lowest extent of calcination ($\sim 75\%$) and the lowest CaO utilization (18%). Material collected in the secondary cyclone was intermediate (calcination of $\sim 90\%$ and CaO utilization of 43%). The low values for both sulfation and calcination of the material collected in the cyclones suggest that it was blown through the bed with little time for reaction.

B. Coal-Combustion Experiments with Coarse Limestone

A series of bench-scale experiments was performed in which coarse-particle-size limestone was used for both the initial fluidized bed and as the additive feed. An objective was to determine the effects of operating variables on SO_2 removal at steady state, where the bed composition (i.e., Ca/S ratio) does not change with continued addition of fresh limestone and removal of reacted limestone.

Experiments were performed at a combustion temperature of 1600°F, with a superficial gas velocity of 3 ft/sec, a 2-ft-deep fluidized bed, and Ca/S mole ratios of 2.3 to 2.6. With three additives (limestone No. 1359, limestone No. 1360, and dolomite No. 1337) having particle sizes in the range 500-600 μm , SO₂ removals of 74 to 86% were achieved. These results indicate that SO₂ removal is relatively independent of the types of additive material used. The use of large-particle-size limestone material (in a limestone bed) gave SO₂ removals similar to those obtained with fine limestone (average particle size of 25 μm in an alumina bed). It was concluded that the longer retention of large-particle-size limestone in the bed compensates for the lesser specific surface.

A marked effect of combustion temperature on SO₂ removal was noted with both coarse limestone No. 1359 and coarse dolomite No. 1337. The experiments were performed over the temperature range 1400-1800°F. At a Ca/S mole ratio of 2.5 with limestone No. 1359, SO₂ removal peaked at 91% in the range from 1500 to 1550°F. For the coarse dolomite additive, the temperature effect was nearly identical. SO₂ removal was high at 1500°F and decreased as the temperature was increased to 1800°F.

The effect on SO₂ emission of the Ca/S mole ratio in the limestone and coal feed streams was measured at a bed temperature of 1550°F. The coarse limestone, having an average particle diameter of 490 μm , was from the same batch as used in the temperature-effect experiment but the coal came from a different batch. At Ca/S ratios of 2.5, 4.6, and 5.5 the SO₂ removals were 78, 95, and 94%, respectively. As the stoichiometric ratio was increased, CaO utilization decreased from 31 to 21 to 17%. Run durations at the three operating conditions were 27, 19, and 20 hr, respectively, to ensure that equilibrium conditions had been reached in the fluid bed.

The effect of superficial gas velocity in the combustor on the removal of SO₂ by coarse particles of limestone No. 1359 averaging 1010- μm dia was determined. The tests were made at 1550°F with a Ca/S mole ratio in the feed of ~4 (3.8 to 4.2 range) and at gas velocities of 3.5, 5.5, and 7.4 ft/sec. The greatest removal of SO₂ in these tests (83%) was observed at the lowest gas velocity, 3.5 ft/sec; similarly, the highest gas velocity, 7.4 ft/sec, resulted in the smallest removal of SO₂ (65%). The data can be correlated by the following equation:

$$R = k_1 e^{-k_2 v}$$

where

R is percent SO₂ removal

v is the superficial gas velocity, ft/sec

k₁ and k₂ are constants.

Tests with a British coal-limestone combination and an American coal-limestone combination were carried out in two 6-in.-dia combustors, one at Argonne National Laboratory (ANL) and the other at the Coal Research Establishment (CRE) laboratories at Cheltenham, England. The designs of these combustors differ slightly. The tests were made to determine if SO_2 removals would differ significantly when the two combustors were operated under similar conditions. The fixed variables included a bed temperature of 800°C (1472°F), a fluidized-bed height of 2 ft, a fluidizing-gas velocity of 3 ft/sec, and an excess of combustion air of 10 to 20%.

The effect on SO_2 removal of three limestone stoichiometric addition levels (i.e., Ca/S mole ratios in the feed streams of ~1, ~2, and ~3) was measured. Both the ANL and CRE coal-limestone combinations were tested at the three Ca/S levels. Only preliminary data are available and these show that data on SO_2 levels obtained at ANL agree reasonably well with those of CRE, but in every test the SO_2 levels obtained at ANL were somewhat higher. The difference possibly reflects differences in combustor design, operating procedures, or analytical bias.

C. Natural Gas Combustion Experiments--NO Levels and SO_2 Sorption and Desorption from CaSO_4

The use of a fluidized-bed combustor for the combustion of natural gas was also investigated. Because a low combustion temperature of 1600°F is feasible in this method of combustion, nitric oxide (NO) generation was held to the level dictated by the nitrogen fixation equilibrium, about 60 ppm. Combustion efficiencies of up to 99% were achieved.

In other natural gas combustion experiments, artificially generated SO_2 was added to the combustor and reacted with limestone at 1600°F . The SO_2 removals, 95 to 99% at a low Ca/S mole ratio of 1.5, were higher than those achieved in coal-burning experiments. These excellent results were probably due to efficient distribution of the injected SO_2 in the combustor and to the ash-free environment.

During gas combustion experiments, it was noted that when a bed of partially sulfated limestone was heated, desorption of SO_2 began at slightly above 1700°F . At 1850°F and with an excess air level in the fluidizing gas giving 1 vol % oxygen in the flue gas, SO_2 concentration in the flue gas was 5000 ppm. This high degree of SO_2 desorption at a relatively low temperature (previously, a temperature of about 2200°F had been thought necessary to obtain this effect) may have been due to localized reducing conditions in the bed at the low excess-air level employed.

D. Reduction of Nitrogen Oxide Emission in Coal-Combustion Experiments

A reduction of NO concentration in the flue gas, concomitantly with a reduction in SO_2 concentration, was noted upon the addition of limestone

to the fluidized bed in coal-combustion experiments. This is probably related to the presence of CaSO_4 in the bed.

Attempts to decompose NO by adding metal oxides (Al_2O_3 , Co_3O_4 , and ZrO_2) as catalysts were not successful. In fact, when Co_3O_4 was tested, the NO concentration in the flue gas increased.

Flue gas from the fluidized-bed combustion of coal was analyzed for nitrogen oxide compounds by three independent analytical procedures. Nitric oxide was the only nitrogen oxide species present in significant quantity.

E. Mathematical Modeling Studies

A mathematical model was developed to predict the degree of SO_2 removal in a fluidized-bed coal combustor as a function of the operating parameters of bed height, superficial gas velocity, and limestone additive feed rate. Data on SO_2 sorption capacity and SO_2 sorption rate of limestone will be acquired to allow application of the model.

Models have been developed also to predict the effects on SO_2 removal of nonuniform feeding of coal, which results in localized reducing or oxidizing conditions at points within and above a fluidized-bed combustor. These mathematical models predict coal concentration gradients within the bed for (1) coal injection at the base of the bed and (2) horizontal-jet coal injection and deep penetration into the bed. The models were applied to the operating conditions anticipated for a large fluidized-bed coal combustor. Results indicated that coal concentration in the bed will be more uniform if coal is injected horizontally in a jet with deep penetration into the bed than if coal is injected vertically from a point at the base of the bed.

VIII. ADDENDUMCHEMICAL ENGINEERING DIVISION PUBLICATIONS
1970A. Open-Literature Publications

- R. J. Armani, R. Gold, R. P. Larsen, and J. H. Roberts
Measured Fission Yields of ^{99}Mo and ^{140}Ba in Fast-Neutron-Induced Fission of ^{239}Pu
Trans. Am. Nucl. Soc. 13(1), 90 (June 1970) Abstract
- J. E. Battles, W. A. Shinn, P. E. Blackburn, and R. K. Edwards
A Mass Spectrometric Study of the Volatilization Behavior in the Plutonium-Carbon System
High Temp. Sci. 2(1), 80-93 (1970)
- J. E. Battles, W. A. Shinn, P. E. Blackburn, and R. K. Edwards
A Mass Spectrometric Investigation of the Volatilization Behavior of $(\text{U}_{0.8}\text{Pu}_{0.2})\text{O}_{2-x}$
Proc. 4th Int. Conf. Plutonium and Other Actinides, Santa Fe, N. M., Oct. 5-9, 1970, Plutonium 1970 and Other Actinides, Nuclear Metallurgy, Vol. 17, Part II, pp. 733-742
- J. J. Barghusen, A. A. Jonke, N. M. Levitz, M. J. Steindler, and R. C. Vogel
Fluid-Bed Fluoride Volatility Processing of Spent Reactor Fuel Materials
Progress in Nuclear Energy, Ser. III, Process Chemistry, Vol. 4, Pergamon Press, Oxford, 1969, pp. 347-398
- M. A. Bergougnon, J. D. Gabor, B. L. Tarmy, and N. J. Weinstein, eds.
Fundamental Processes in Fluidized Beds
Chem. Eng. Progr. Symp. Ser. 66(101), 1970
- E. J. Cairns and H. Shimotake
Recent Advances in Fuel Cells and Their Application to New Hybrid Systems
Fuel Cell Systems-II, Proc. 5th Biennial Fuel Cell Symp. Advances in Chem., Ser. 90, Am. Chem. Soc., Washington, 1969, pp. 392-425
- E. J. Cairns and R. Sridhar
Electrical Resistivities of Liquid Mixtures of Selenium and Tellurium
J. Electrochem. Soc. 117, 125c (March 1970) Abstract
- E. J. Cairns, G. H. Kucera, P. T. Cunningham
Thermodynamic Studies of the Lithium-Selenium System by an Emf Method
Extended Abstracts of CITCE Meeting, Prague, Sept. 28-Oct. 2, 1970, p. 95
- M. G. Chasanov
Material Behavior
Nucl. Safety 11(2), 163 (March-April 1970) Abstract

- M. G. Chasanov
Material Behavior
Nucl. Safety 11(4), 338 (July-August 1970) Abstract
- P. M. Danielson
An Investigation of Gasket Coating Materials for Ultrahigh-Vacuum Seals
J. Vacuum Sci. Technol. 7(3), 449-452 (1970)
- P. M. Danielson
Aluminum Sorption Roughing Pump for Small Vacuum Systems
J. Vacuum Sci. Technol. 7(5), 527-530 (September/October 1970)
- T. L. Denst, E. Greenberg, J. L. Settle, and W. N. Hubbard
An Improved Interconnecting Valve for a Two-Compartment Calorimetric Bomb
Rev. Sci. Instr. 41, 588-589 (April 1970)
- J. E. Draley and J. R. Weeks, Eds.
Corrosion by Liquid Metals, Proc. 1969 Fall Mtg. Met. Soc. AIME, Philadelphia, October 13-16, 1969, Plenum Press, New York, 1970
- N. D. Dudey, R. R. Heinrich, and A. A. Madson
Reaction Cross Sections of $^{85}\text{Rb}(n,\gamma)$ $^{86\text{m}}\text{Rb}$, $^{87}\text{Rb}(n,\gamma)$ ^{88}Rb , and $^{89}\text{Y}(n,\gamma)$ $^{90\text{m}}\text{Y}$ between 0.16 MeV and 1.5 MeV
J. Nucl. Energy 24(4), 181-189 (1970)
- N. D. Dudey, S. D. Harkness, and H. Farrar IV
Helium Production in EBR-II Irradiated Stainless Steel
Nucl. Appl. Technol. 9(5), 700-710 (1970)
- J. G. Eberhart
Comments on Wetting of Binary Aluminum Alloys in Contact with Be, B_4C , and Graphite
J. Amer. Ceram. Soc. 53, 223-224 (April 1970) Note
- J. G. Eberhart
The Surface Tension and Critical Properties of Liquid Metals
J. Colloid and Interface Sci. 33, 191-192 (May 1970)
- J. G. Eberhart, F. A. Cafasso, H. M. Feder, and W. A. Kremsner
The Grain Boundary Grooving of Iron in Liquid Sodium
Corrosion by Liquid Metals. Plenum Press, New York, 1970, pp. 461-467
- A. K. Fischer and S. A. Johnson
Liquid-Vapor Equilibrium in the Sodium-Lead System
J. Chem. Eng. Data 15, 492-495 (October 1970)
- A. K. Fischer, V. A. Maroni, A. D. Tevebaugh, and E. J. Cairns
Secondary Power-Producing Cell
U. S. Patent 3,531,324 (Sept. 29, 1970)

- D. R. Fredrickson, M. G. Chasanov, R. D. Barnes, and S. A. Johnson
The Enthalpy of Solid and Liquid Na_3Bi by Drop Calorimetry
High Temp. Sci. 2(3), 259-264 (1970)
- D. R. Fredrickson, R. D. Barnes, and M. G. Chasanov
The Enthalpy of Uranium Diboride from 1300 to 2300°K by Drop Calorimetry
High Temp. Sci. 2(3), 299-301 (1970)
- D. R. Fredrickson and M. G. Chasanov
Enthalpy of UO_2 and Sapphire to 1500 K by Drop Calorimetry
J. Chem. Thermodyn. 2(5), 623-629 (1970)
- J. D. Gabor
Heat Transfer to Particle Beds with Gas Flows Less than or Equal to that Required for Incipient Fluidization
Chem. Eng. Sci. 25, 979-984 (June 1970)
- J. D. Gabor
Wall-to-Bed Heat Transfer in Fluidized and Packed Beds
Chem. Eng. Prog. Symp. Ser. 66(105), 76 (1970)
- J. D. Gabor and L. B. Koppel
Interaction Effects on the Fluid Dynamics of Bubbles in a Fluidized Bed: Chain of Rising Bubbles in an Infinite Three-Dimensional Medium
Chem. Eng. Prog. Symp. Ser. 66(105), 28 (1970)
- E. Greenberg, C. A. Natke, and W. N. Hubbard
The Enthalpy of Formation of Silicon Carbide by Fluorine Bomb Calorimetry
J. Chem. Thermodynam. 2(2), 193-201 (1970)
- J. T. Holmes, D. R. Vissers, J. D. Gabor, and I. Knudsen
Uranium Oxide Fluorination with Fluorine and Fluorine Interhalogens
U. S. Patent 3,490,881 (Jan. 20, 1970)
- C. E. Johnson and C. E. Crouthamel
Cladding Interactions in Mixed Oxide Irradiated Fuels
J. Nucl. Mater. 34, 101-104 (January 1970)
- C. E. Johnson and A. K. Fischer
New Measurements for the Sodium-Bismuth Phase Diagram
J. Less-Common Metals 20, 339-344 (April 1970)
- C. E. Johnson, C. E. Crouthamel, H. Y. Chen, and P. E. Blackburn
Electron Microprobe Analysis of Irradiated Fuels
Proc. 2nd Ann. Tech. Mtg. Int. Metallographic Soc., Los Alamos, September 8-10, 1969, Ed. K. A. Johnson. Vergara Prntg. Co., Santa Fe, N. Mex., 1970, p. 139
- G. K. Johnson, P. N. Smith, E. H. Appelman, and W. N. Hubbard
The Thermodynamic Properties of the Perbromate and Bromate Ions
Inorg. Chem. 9, 119-125 (January 1970)

- G. K. Johnson, E. H. Van Deventer, O. L. Kruger, and W. N. Hubbard
The Enthalpy of Formation of Plutonium Monocarbide
J. Chem. Thermodyn. 2(5), 617-622 (1970)
- I. Johnson and R. M. Yonco
Thermodynamics of Cadmium- and Zinc-Rich Alloys in the Cd-La,
Cd-Ce, Cd-Pr, Zn-La, Zn-Ce, and Zn-Pr Systems
Met. Trans. 1, 905-910 (April 1970)
- I. Johnson, J. J. Heiberger, and J. Fischer
Thermodynamics of Dilute Solutions of Neptunium in Liquid Magnesium
Met. Trans. 1, 1253-1255 (May 1970)
- A. A. Jonke, E. L. Carls, R. L. Jarry, and L. J. Anastasia
Reduction of Atmospheric Pollution by the Application of Fluidized-Bed
Combustion
Proceedings of American Power Conference 1970, Vol. 32,
pp. 445-452 (1970)
- W. Y. Kato, R. J. Armani, R. P. Larsen, P. E. Moreland, L. A. Mountford,
J. M. Gasidlo, R. J. Popek, and C. D. Swanson
An Integral Measurement of ^{239}Pu Alpha
Trans. Am. Nucl. Soc. 13(1), 88 (June 1970) Abstract
- M. Kobayashi, D. Ramaswami, and W. T. Brazelton
Pulsed Bed Approach to Fluidization
Chem. Eng. Progr. Symp. Ser. 66(105), 47-57 (1970)
- M. Kobayshi, D. Ramaswami, and W. T. Brazelton
Heat Transfer from an Internal Source to a Pulsed Bed
Chem. Eng. Progr. Symp. Ser. 66(105), 58-67 (1970)
- L. B. Koppel, R. D. Patel, and J. T. Holmes
Statistical Models for Surface Renewal in Heat and Mass Transfer.
Part III. Residence Times and Age Distributions at Wall Surface of
a Fluidized Bed, Application of Spectral Density. Part IV. Wall to
Fluidized Bed Heat Transfer Coefficients
A.I.Ch.E. Journal 16(3), 456-471 (1970)
- H. Littman, R. Pfeffer, J. Feinman, B. S. Lee, and N. M. Levitz, eds.
Fluidization Fundamentals and Application
Chem. Eng. Progr. Symp. Ser. 66(105) (1970)
- J. O. Ludlow, M. A. Slawewski, and H. L. Brown
Pneumatic Tube Transfer System for Radioactive Systems
Proc. 18th Conf. Remote Systems Technol., Washington,
November 1970, pp. 107-115, Amer. Nucl. Soc., Hinsdale, Ill. (1970).
Also published in Trans. Amer. Nucl. Soc. 13(2), 845 (1970)
Abstract
- V. A. Maroni and E. J. Cairns
Raman Spectra of Fused Carbonates
J. Chem. Phys. 52, 4915-4916 (May 1, 1970) Letter

- V. A. Maroni, D. M. Gruen, R. L. McBeth, and E. J. Cairns
Raman Spectrum and Vibrational Analysis for Gaseous Aluminum Chloride
Spectrochim. Acta 26A, 418-421 (1970)
- V. A. Maroni and E. J. Hathaway
Raman Spectra of the CdCl_2 -KCl System
Electrochim. Acta 15, 1837-1840 (1970)
- K. M. Myles
The Ternary System Copper-Magnesium-Calcium
J. Less-Common Metals 20, 149-154 (February 1970)
- P. A. G. O'Hare, G. K. Johnson, and E. H. Appelman
The Thermochemistry of Aqueous Xenon Trioxide
Inorg. Chem. 9, 332-334 (February 1970)
- P. A. G. O'Hare, E. Benn, F. Y. Cheng, and G. Kuzmycz
A Fluorine Bomb Calorimetric Study of Molybdenum Disulfide. The Standard Enthalpies of Formation of the Di- and Sesquisulfides of Molybdenum
J. Chem. Thermodyn. 2, 797-804 (1970)
- P. A. G. O'Hare
Some Experimental and Computed Properties for the Monofluorides of Oxygen and Sulfur, and for Nitrogen Monosulfide
Abstracts of Papers, 159th Nat. Mtg. Am. Chem. Soc., Houston, February 22-27, 1970, PHYS-073
- P. A. G. O'Hare, W. N. Hubbard, O. Glemser, and J. Wegener
Thiazyl Tri- and Monofluorides: Enthalpies of Formation and Dissociation Energies of the $\text{N}\equiv\text{S}$ Bonds
J. Chem. Thermodyn. 2, 71-76 (1970)
- P. A. G. O'Hare
Dissociation Energies, Enthalpies of Formation, Ionization Potentials, and Dipole Moments of NS and NS^+
J. Chem. Phys. 52, 2992-2996 (March 15, 1970)
- P. A. G. O'Hare and A. C. Wahl
A Quantum-Chemical Study of SF and PF
Abstracts of Papers Presented at the 3rd European Symposium on Fluorine Chemistry, Aix-en-Provence, France, September 14-17, 1970 Abstract No. 50
- P. A. G. O'Hare and A. C. Wahl
Oxygen Monofluoride (OF , $^2\Pi$): Hartree-Fock Wavefunction, Binding Energy, Ionization Potential, Electron Affinity, Dipole and Quadrupole Moments, and Spectroscopic Constants. A Comparison of Theoretical and Experimental Results
J. Chem. Phys. 53(6), 2469-2478 (1970)

- P. A. G. O'Hare and A. C. Wahl
Hartree-Fock Wavefunctions and Computed Properties for the Ground ($^2\Pi$) States of SF and SeF and Their Positive and Negative Ions. A Comparison of the Theoretical Results with Experiment
J. Chem. Phys. 53(7), 2834-2846 (1970)
- D. Ramaswami and A. A. Jonke
Sea Water Desalination
U. S. Patent 3,491,822 (Jan. 27, 1970)
- E. Rudzitis, E. H. Van Deventer, and W. N. Hubbard
Fluorine Bomb Calorimetry. The Enthalpy of Formation of Phosphorus Trifluoride
J. Chem. Thermodynam. 2(2), 221-225 (1970)
- R. A. Sharma and I. Johnson
Study of the Reduction of UO_2 by Magnesium or Calcium Dissolved in Molten Chlorides
Met. Trans. 1, 291-297 (January 1970)
- R. A. Sharma
Liquidus and Eutectic Phase Equilibria in the Systems CaI_2 - CaCl_2 , CaI_2 - CaF_2 , and CaI_2 - MgCl_2
High Temp. Sci. 1(4), 423-429 (1969)
- R. A. Sharma
Thermodynamic Properties of Liquid Mg + Pb and Mg + Sn Alloys by E.M.F. Measurements
J. Chem. Thermodynam. 2(3), 373-389 (1970)
- R. A. Sharma
The Solubilities of Calcium in Liquid Calcium Chloride in Equilibrium with Calcium-Copper Alloys
J. Phys. Chem. 74, 3896-3900 (Oct. 29, 1970)
- H. Shimotake, M. L. Kyle, V. A. Maroni, and E. J. Cairns
Lithium/Sulfur Cells and Their Potential for Vehicle Propulsion
Proc. 1st Intern. Electric Vehicle Symp., Phoenix, Arizona, November 5-7, 1969, Electric Vehicle Council, 750 3rd Ave., New York 10017, pp. 392-415
- H. Shimotake, C. E. Johnson, M. S. Foster, and E. J. Cairns
Electrochemical Cell
U. S. Patent 3,488,221 (Jan. 6, 1970)
- R. Sridhar, C. E. Johnson, and E. J. Cairns
Phase Diagrams of the Systems LiI - KI and LiI - RbI
J. Chem. Eng. Data 15, 244-245 (April 1970)
- R. K. Steunenberg, R. D. Pierce, and L. Burris
Pyrometallurgical and Pyrochemical Fuel Processing Methods
Progress in Nuclear Energy, Ser. III, Process Chemistry, Vol. 4, Pergamon Press, Oxford, 1969, pp. 461-504

- M. Tetenbaum and P. D. Hunt
Total Pressure of Uranium-Bearing Species over Oxygen-Deficient Urania
J. Nucl. Mater. 34, 86-91 (January 1970)
- L. E. Trevorrow, T. J. Gerding, and M. J. Steindler
Ultraviolet-Activated Synthesis of Plutonium Hexafluoride at Room Temperature
Inorg. Nucl. Chem. Letters 5, 837-839 (October 1969)
- E. H. Van Deventer, E. Rudzitis, and W. N. Hubbard
The Enthalpy of Formation of Thorium Tetrafluoride by Fluorine Bomb Calorimetry
J. Inorg. Nucl. Chem. 32, 3233-3236 (1970)
- D. R. Vissers, M. J. Steindler, and J. T. Holmes
Tellurium Hexafluoride Removal Method
U. S. Patent 3,491,513 (Jan. 27, 1970)
- D. R. Vissers, J. T. Holmes, and P. A. Nelson
A Hydrogen Monitor for Detecting Leaks in LMFBR Steam Generators
Trans. Am. Nucl. Soc. 13(1), 96 (June 1970) Abstract

B. Papers Accepted for Publication in the Open Literature

- J. D. Gabor
Boundary Effects on a Rising Bubble in a Finite Two-Dimensional Fluidized Bed
Accepted for Publication in Chem. Eng. Sci.
- T. R. Johnson, R. D. Pierce, F. G. Teats, and E. F. Johnston
Behavior of Countercurrent Liquid-Liquid Columns with a Liquid Metal
Accepted for publication in A.I.Ch.E. Journal
- M. Krumpelt and I. Johnson
The Thermodynamics of the Cadmium-Neptunium System
Accepted for publication in Met. Trans.
- L. Leibowitz, M. G. Chasanov, L. W. Mishler, and D. F. Fischer
Enthalpy of Liquid Uranium Dioxide to 3500°K
Accepted for publication in J. Nucl. Mater.
- L. Leibowitz, M. G. Chasanov, and R. A. Blomquist
Speed of Sound in Liquid Sodium
Accepted for publication in J. Appl. Phys.

C. ANL Reports

- L. Burris, J. E. Draley, P. A. Nelson, F. A. Cafasso, T. F. Kassner,
J. T. Holmes, W. E. Miller, and R. J. Meyer
Sodium Technology Quarterly Report, January, February, March 1970
ANL/ST-2

- L. Burris, J. E. Draley, P. A. Nelson, F. A. Cafasso, T. F. Kassner,
J. T. Holmes, W. E. Miller, and R. J. Meyer
Sodium Technology Quarterly Report, April, May, June 1970
ANL/ST-3
- E. L. Carls
Review of British Program on Fluidized-Bed Combustion: Report of
U. S. Team Visit to England, February 17-28, 1969
ANL/ES-CEN-1000
- M. G. Chasanov and D. F. Fischer
Out-of-Pile Study of the Effects of Thermal Gradients on the Distribution
of Plutonium in Fast-Reactor Fuel Materials
ANL-7703
- D. W. Cissel, L. F. Coleman, F. O. Pancner, F. A. Smith, and
A. D. Tevebaugh
Guidelines for Sodium Fire Prevention, Detection, and Control: Report
of the Ad Hoc Committee on Sodium Fires
ANL-7691
- N. D. Dudey and R. R. Heinrich
Flux-Characterization and Neutron-Cross-Section Studies in EBR-II
ANL-7629
- A. A. Jonke, E. L. Carls, R. L. Jarry, M. Haas, W. A. Murphy, and
C. B. Schoffstoll
Reduction of Atmospheric Pollution by the Application of Fluidized-Bed
Combustion. Annual Report, July 1968-June 1969
ANL/ES-CEN-1001
- R. W. Kessie, L. J. Marek, and M. J. Steindler
Laboratory Investigations in Support of Fluid-Bed Fluoride Volatility
Processes. Part XXI. Filtration of Aerosols from Plutonium Hexa-
fluoride Hydrolysis
ANL-7612
- M. Kobayashi
Pulsed-Bed Approach to Fluidization
ANL-7592
- B. J. Kullen, W. A. Murphy, E. L. Carls, N. M. Levitz, G. J. Vogel, and
R. V. Kinzler
Engineering Development of Fluid-Bed Fluoride Volatility Processes.
Part 16. A Safety Manual for the Engineering-Scale Alpha Facility
ANL-7672

- N. M. Levitz, G. J. Vogel, E. L. Carls, I. E. Knudsen, D. E. Grosvenor, R. W. Lambert, E. L. Youngblood, W. A. Murphy, B. J. Kullen, R. V. Kinzler, and J. E. Kincinas
Engineering Development of Fluid-Bed Fluoride Volatility Processes. Part 14. Processing Experience in Fluorinating Plutonium Materials and Thermally Decomposing Plutonium Hexafluoride in the Engineering-Scale Alpha Facility
ANL-7473
- P. A. G. O'Hare and A. C. Wahl
Hartree-Fock Wave Functions and Computed One-Electron Properties for Oxygen Monofluoride (OF, $^2\Pi$) at Six Internuclear Separations
ANL-7702
- R. R. Stewart, C. E. Dickerman, N. R. Stalica, and W. B. Doe
A Study of the Physical Properties of Nominal 0.7, 3, and 6 a/o Burnup UO_2 Fast-Reactor Fuel Pins Preparatory to Transient TREAT Exposure
ANL-7571
- K. A. Varteressian and L. Burris
Fission-Product Spectra from Fast and Thermal Fission of ^{235}U and ^{239}Pu
ANL-7678
- P. Vilinskas, E. C. Filewicz, and J. R. Humphreys
Selected Data and Discussion of the Plugging Indicator for Sodium Loops
ANL-7658
- R. C. Vogel, L. Burris, A. D. Tevebaugh, D. S. Webster, and J. Royal
Chemical Engineering Division Research Highlights, January-December 1969
ANL-7650
- R. C. Vogel, L. Burris, A. D. Tevebaugh, D. S. Webster, and J. Royal
Chemical Engineering Division Annual Report, 1969
ANL-7675
- D. S. Webster, A. A. Jonke, G. J. Bernstein, N. M. Levitz, R. D. Pierce, M. J. Steindler, and R. C. Vogel
Chemical Engineering Division Fuel Cycle Technology Quarterly Report, April, May, June, 1970
ANL-7735
- I. O. Winsch, R. D. Pierce, D. E. Grosvenor, L. Burris, T. F. Cannon, P. J. Mack, K. Nishio, and K. R. Tobias
The EBR-II Skull Reclamation Process. Part IV. Pilot-Plant Development
ANL-7614

D. Papers Presented at Scientific Meetings

M. D. Adams

Ultramicrosampling with a Laser-Microscope

Presented at Inter/Micro-70 Symposium, Chicago, July 1, 1970

L. J. Anastasia, E. L. Carls, R. L. Jarry, A. A. Jonke, and G. J. Vogel

Pollution Control Capabilities of Fluidized-Bed Combustion

Presented at 2nd Int. Conf. on Fluidized-Bed Combustion,
Hueston Woods, Ohio, Oct. 4-7, 1970

L. Burris, P. A. Nelson, and J. T. Holmes

Industrial Spin-Off from Developments in Sodium Technology

Presented at AIChE 63rd Annual Meeting, Chicago,
Nov. 29-Dec. 3, 1970

L. Burris

Sodium Technology - Engineering Development Needed for Fast Reactors

Presented at Iowa State University, Nov. 2, 1970

E. J. Cairns

High Temperature Electrochemical Energy Conversion

Presented at Physics Dept. Seminar, Northern Illinois University,
January 9, 1970

E. J. Cairns

(1) AEC (ANL) Electrochemical Energy Conversion Program

(2) NAPCA Battery Program

Presented at Power Information Center (PIC) Mtg.,
Ft. Monmouth, N. J., April 7-8, 1970

E. J. Cairns

Lithium/Chalcogen Cells

Presented at Institute for Technical Physics, Braunschweig
University, Braunschweig, Germany, Sept. 27, 1970

E. J. Cairns, E. C. Gay, H. Shimotake, and R. K. Steunenberg

Electrochemical Energy Conversion

Presented at AIChE 63rd Annual Meeting, Chicago, Nov. 29-
Dec. 3, 1970

A. A. Chilenskas, H. Shimotake, R. K. Steunenberg, and E. J. Cairns

The Development of Lithium/Selenium Secondary Cells and Batteries
for Implantation

Presented at 5th IECEC Mtg., Las Vegas, Nev., Sept. 21-25, 1970

C. E. Crouthamel, C. E. Johnson, and I. Johnson

Techniques for Materials Investigations

Presented at AIChE 63rd Annual Meeting, Chicago, Nov. 29-
Dec. 3, 1970

- J. E. Draley
Corrosion by Liquid Sodium
Presented at Division of Interdisciplinary Studies, Clemson
University, Aug. 13, 1970
- J. G. Eberhart and H. M. Feder
The Simultaneous Determination of Surface and Volume Diffusion
Coefficients from the Kinetics of Grain Boundary Grooving
Presented at Amer. Vac. Soc. Surface Science Symp., Albuquerque,
N. Mex., Apr. 22-24, 1970
- J. G. Eberhart
Grain Boundary Grooving in a Sodium Environment
Presented at Materials Science Seminar, Sandia Laboratory,
Albuquerque, N. Mex., July 26, 1970
- J. D. Gabor
Boundary Effects on a Rising Bubble in a Finite Two-Dimensional Bed
Presented at AIChE 63rd Annual Meeting, Chicago, Nov. 29-
Dec. 3, 1970
- E. C. Gay, L. E. Trevorrow, M. L. Kyle, V. M. Kolba, and E. J. Cairns
Lithium/Selenium Cells with Paste Electrolytes
Presented at Electrochem. Soc. Mtg., Atlantic City, Oct. 4-8, 1970
- R. L. Jarry, L. J. Anastasia, E. L. Carls, A. A. Jonke, and G. J. Vogel
Comparative Emissions of Pollutants during Combustion of Natural Gas
and Coal in Fluidized Beds
Presented at 2nd Int. Conf. on Fluidized-Bed Combustion, Hueston
Woods, Ohio, Oct. 4-7, 1970
- A. A. Jonke
Fluidized Bed Combustion
Presented at 19th Annual Steam Power Plant Operations Meeting,
University of Wisconsin, Madison, Wisc., Oct. 1-2, 1970
- A. A. Jonke and N. M. Levitz
Fluidization Technology in Nuclear Chemical Engineering
Presented at AIChE 63rd Annual Meeting, Chicago, Nov. 29-
Dec. 3, 1970
- V. A. Maroni, E. J. Hathaway, and E. J. Cairns
Structural Studies of Magnesium Halide-Potassium Halide Melts by
Raman Spectroscopy
Presented at 21st Mid-America Symposium on Spectroscopy,
Chicago, June 4, 1970
- K. M. Myles
The Ternary System Copper-Magnesium-Calcium
Presented at 1970 TMS Spring Mtg. AIME, Las Vegas, Nev.,
May 11-14, 1970

- P. A. Nelson
Monitoring and Control of Impurities in Breeder Reactor Sodium
Present at Nuclear Engineering Dept., University of Michigan,
Nov. 13, 1970
- R. D. Pierce and R. K. Steunenberg
Processing with Liquid Metals and Salts
Presented at AIChE 63rd Annual Meeting, Chicago, Nov. 29-
Dec. 3, 1970
- J. L. Settle, G. K. Johnson, E. Greenberg, and W. N. Hubbard
Additional Studies of the Enthalpies of Formation and Solution of
Liquid HF
Presented at 25th Calorimetry Conference, Nat. Bur. Std.,
Gaithersburg, Md., Oct. 19-22, 1970
- R. Sridhar and E. J. Cairns
Electrical Resistivities of Liquid Mixtures of Selenium and Tellurium
Presented at Electrochemical Society Meeting, Los Angeles,
May 10-15, 1970
- M. Tetenbaum
Effect of Dissolution of Oxygen on the Activity of Carbon in the
U-C-O System
Presented at Gordon Research Conference on High Temperature
Chemistry, Issaquah, Washington, July 6-10, 1970
- M. Tetenbaum, P. D. Hunt, and D. R. O'Boyle
Thermodynamics of Fuel Materials: Total Vapor Pressures and Carbon
Potentials in the Ternary U-C-Pu System
Presented at 6th U. S.-Japan Fuels Information Meeting, Seattle,
Washington, Oct. 12-15, 1970
- A. D. Tevebaugh
U. S. Energy Resources
Presented at U. S. Army Reserve Corps Meeting, Chicago,
Feb. 16, 1970
- D. R. Vissers, J. T. Holmes, and L. G. Bartholme
High Vacuum Technology and Its Application to Monitoring Hydrogen in
LMFBR Systems
Presented at 8th Ann. Symp., Midwest Sect., Amer. Vac. Soc.,
Argonne, Ill., May 21-22, 1970

X

ARGONNE NATIONAL LAB WEST



3 4444 00011471 0

